PHYSICS IN HIGH ELECTRIC FIELDS

by

Markus Leopold Karahka

Submitted in partial fulfilment of the requirements
for the degree of Doctor of Philosophy

at

Dalhousie University
Halifax, Nova Scotia
September 2016

As Ralph Waldo Emerson said “Adopt the pace of nature; her secret is patience.” I dedicate this to my family and friends for all their love, patience, and support throughout my years and especially to Laura, the light of my life.

Table of Contents

LIST OF TABLES

LIST OF FIGURES

Abstract

This thesis is a theoretical study on the effects of high electrostatic fields, fields of the order of Volts per Angstrøm, on the structure and stability of water, MgO, ZnO, and Si nanoclusters. A high electrostatic field applied across a material will raise the energy levels of a molecular orbital relative to another molecular orbital in the field direction. This rearrangement of the bonding and antibonding orbitals or field-induced chemistry can cause: (i) the electronic transformation of one material into another creating a continuous periodic table, (ii) the formation of new structures which are stable in the field, and (iii) field-induced dissociation or field evaporation. We perform detailed quantum mechanical calculations using density functional theory to explain experimental observations and explore the above effects.

To understand Atom Probe results on the field evaporation of semiconductors we calculate the effects of high electrostatic fields on MgO, ZnO, and Si clusters to follow the structural changes during field evaporation and to obtain potential energy curves, partial charges and desorption pathways. We obtain field evaporation products seen in experiment, address the question of what happens to the oxygen during field evaporation of the oxide, and explain why the O goes missing. It can migrate down the (metallic) surface of the tip and eventually desorb either as atoms or molecules (neutral). Evidence of field-induced metallization of the semiconductors is seen through closure of the HOMO-LUMO gaps, increases in dielectric constant and polarizability, and field expulsion inside the clusters. Strong band gap shrinkage of a dielectric nanostructure in a field was experimentally confirmed.

Finally, it has been observed in field ion microscopy experiments that long whiskers of up to 12 water molecules can form. We present whisker structures and energetics, lower and upper threshold fields, and fragmentation patterns. Our results are in general agreement with experiments including the fact that predominantly small protonated clusters break off. We also look at the quantum mechanics of charge transport along proton wires both with free ends and donor/acceptor terminated. The charge transfer times and the conductivity of the proton wire were calculated in agreement with experimental results.

LIST OF ABBREVIATIONS AND SYMBOLS USED

AO	Atomic Orbital
APM	Atom Probe Microscopy
APT	Atom Probe Tomography
B3LYP	Becke, 3-parameter, Lee-Yang-Parr functional
DC	Direct Current
DFT	Density Functional Theory
EVB	Empirical Valence Band
FE	Field Evaporation
FIM	Field Ion Microscopy
FPI	Feynman Path Integral
GGA	Generalized Gradient Approximation
HF	Hartee-Fock
HOAO	Highest Occupied Atomic Orbital
HOMO	Highest Occupied Molecular Orbital
IR	Infrared
LCAO	Linear Combination of Atomic Orbitals
LDA	Local Density Approximation
LUMO	Lowest Unoccupied Molecular Orbital
MD	Molecular Dynamics
MO	Molecular Orbital
NIST	National Institute of Standards and Technology
NSERC	Natural Sciences and Engineering Research Council of Canada
SCF	Self-Consistent Field
TOF	Time of flight
UV	Ultraviolet
WKB	Wentzel–Kramers–Brillouin
a	Lattice Constant
a_s	Adsorption site area
A	Atom
b	Bond length
b_0	Equilibrium bond length
c_{ij}	Weights of the atomic orbital
C_P	Heat capacity
d	Bond length
$\boldsymbol{d}$	Distance
d_{jp}	Basis set constant
d_0	Equilibrium bond length
$\boldsymbol{D}$	Electric displacement
D_e	Electron diffusion coefficient
D_h	Hole diffusion coefficient
D_{O_2}	Molecular dissociation energy
e	Electron charge
E	Energy

$\boldsymbol{E}$	Electric field
$E[\rho]$	Energy functional
E_0	Electric field at tip apex
E_B	Binding energy per atom or molecule
E_{crit}	Critical field for Zener-type interband tunneling
E_{diss}	Dissociation Energy
$E_{el}(\boldsymbol{E})$	Electronic energy
$E_{el}(\text{Mg})$	Electronic energy of Magnesium
$E_{el}(\text{MgO},d)$	Electronic energy of MgO with its atoms separated by a distance d
$E_{el}(\text{O})$	Electronic energy of Oxygen
$E_{el}(\text{Zn})$	Electronic energy of Zinc
$E_{el}(\text{ZnO},d)$	Electronic energy of ZnO with its atoms separated by a distance d
E_{ev}	Evaporation field strength
E_{F}	Fermi energy
$E_{\text{Field}}(\boldsymbol{E})$	Field energy
E_i	Ionization field
E_{system}	Energy of the system
$E_{\text{xc}}[\rho]$	Exchange-correlation functional
$E_{\text{xc}}^{\text{GGA}}[\rho]$	Generalized gradient approximation exchange-correlation functional
$E_{\text{xc}}^{\text{LDA}}[\rho]$	Local density approximation exchange-correlation functional
E_{z}	Electric field strength in the z direction
f	Force
f_{M}	Metal fraction
f_{O}	Oxygen fraction
F_{laser}	Laser fluence
g	Primitive gaussian
G	Conductance
h	Planck's Constant
$\hbar$	Reduced Planck's constant
H	Field constant
I	Electric current; Ionization energy
J_{e}	Electron current density
J_{h}	Hole current density
k_{B}	Boltzmann Constant
k_{f}	Field reduction factor
l	Angular quantum number
m	Particle mass; Magnetic quantum number
M	Metal
n	Number of monomers in a molecule; Number of electrons; Number of atoms; Charge state; Principal quantum number
n_{e}	Density of electrons
n_{h}	Density of holes
$\boldsymbol{N}$	Torque
$\langle N \rangle$	Number of kink site atoms
$\boldsymbol{p}$	Induced dipole moment
$\boldsymbol{P}$	Polarization

$P_{\mu\nu}$	Corresponding element of an appropriate density matrix
q	Charge; Detector efficiency
q_3	Partition function of the translational motion of the molecule parallel and perpendicular to the surface
$q_i^{(n)}$	Mulliken charge on atom i in the nth iteration
$Q_{0'}$	Proportionality factor
Q_n	Activation energy
$\boldsymbol{r}$	Electronic spatial coordinate; Distance
r_0	Atomic radius
$r_{cm}^{(n)}$	Center of mass of the charge cloud in the nth iteration
$r_{des}^{(ass)}$	Associative thermal desorption rate constant
$r_{des}^{(mol)}$	Desorption rate constant
r_{diss}	Rate constant of dissociation
r_i	Hopping rate
r_{tip}	Tip apex radius of curvature
R	Radius; Resistance; Metal to oxygen yield ratio
$\boldsymbol{R}$	Nuclear spatial coordinate
S	Overlap integral; Total spin for a molecule
S_e	Electron generation rate
S_h	Hole generation rate
$S_{\mu\nu}$	Overlap matrix
$S^{(O)}(T)$	Sticking coefficient of O
$S^{(O_2)}(T)$	Sticking coefficient of O_2
t	Time
T	Temperature, Transmission coefficient
$T[\rho]$	Kinetic energy functional
$v_{eff}(\boldsymbol{r})$	Effective one-electron potential
$v_{ext}(\boldsymbol{r})$	Static external electrostatic potential
$v_H(\boldsymbol{r})$	Hartree potential
$v_{xc}(\boldsymbol{r})$	Exchange-correlation potential
V	Volume; Voltage; Energy; Activation barrier
$V(d)$	Potential energy
$V(\boldsymbol{r})$	Electrostatic potential
V_0	Applied potential between the tip and a flat counter-electrode; Atomic binding energy
V_a	Atomic potential energy curve
$V_{ext}[\rho]$	Static external electrostatic potential functional
V_H	Hartree energy
$V_H[\rho]$	Hartree functional
V_i	Ionic potential energy curve
V_M	Metal binding energy
V_{mem}	Membrane potential
$V_{nucl\text{-}nucl}$	Nuclear interaction energy
V_O	Oxygen binding energy
x	Distance
x_c	Critical distance

Y	Ion yield
Y_M	Metal ion yield
Y_O	Oxygen ion yield
z	Distance
z_0	Equilibrium distance
z_A	Distance of atom A from the surface
z_B	Distance of atom B from the surface
z_c	Critical distance
z_{int}	Partition function for internal vibration and rotation in the adsorbed state
Z	Atomic number
Z_{int}	Partition function for internal vibration and rotation in the gas phase
α	Spin up electrons; Atomic polarizability; Absorption coefficient, Radial extent of primitive gaussian
α_a	Atomic polarizability
β	Spin down electrons; Dimensionless shape factor
γ	The angle between the electric field direction and the dipole moment of a water molecule; Absorption properties coefficient
γ_a	Hyperpolarizability
Γ	Energy broadening; Reflectivity
$\delta E_{xc}[\rho]$	Functional derivative of the exchange-correlation functional
Δ	Field penetration depth
ϵ	Permittivity
ϵ_0	Permittivity of free space
ϵ_r	Relative permittivity or dielectric constant
ε_{gap}	Band gap
ε_i	Molecular orbital energy; Single electron eigenenergy
$\varepsilon_{xc}(\rho(\boldsymbol{r}))$	Exchange-correlation energy per particle
$\varepsilon_{xc}^{GGA}(\rho(\boldsymbol{r}))$	Generalized gradient approximation exchange-correlation energy per particle
$\varepsilon_{xc}^{LDA}(\rho(\boldsymbol{r}))$	Local density approximation exchange-correlation energy per particle
κ	Dimensionless tip geometry factor; Impact ionization coefficient
λ_{th}	Thermal wavelength
Λ	Field dependent binding energy of the surface atom
$\mu(\boldsymbol{E})$	Field dependent dipole moment
μ_e	Electron mobility
μ_h	Hole mobility
μ_{water}	Dipole Moment of water
ν	Vibrational frequency; Prefactor
ν_M	Metal prefactor
ν_O	Oxygen prefactor
$\boldsymbol{\Xi}(\boldsymbol{R})$	Nuclear wavefunctions
ρ	Charge density; Resistivity
$\rho(\mathbf{r})$	Ground state electron density
τ	Transfer time; Dielectric relaxation time; Recombination time
τ_{evap}	Evaporation time
φ	Work function; Detection rate

φ_-	Anti-bonding orbital
φ_+	Bonding orbital
φ_i	One-electron functions or molecular orbitals
φ_μ	Orbital basis functions
φ_ν	Orbital basis functions
$\boldsymbol{\Phi}_{el}(\boldsymbol{r})$	Electron wavefunctions
χ_e	Electric susceptibility
χ_j	Atomic orbitals
$\boldsymbol{\Psi}(\boldsymbol{r}, \boldsymbol{R})$	Total molecular wavefunction
$\Psi_i(\boldsymbol{r})$	Single electron wavefunction
ω	Photon energy

ACKNOWLEDGEMENTS

First I would like to thank my supervisor. Dr. Hans Jürgen Kreuzer for being a mentor, colleague, and friend over the years. His support has given me the experience of speaking at various international conferences and publishing many papers. I have learned a great deal about physics, publishing, and academia for which I am indebted and heard many an interesting story about physicists and a life in science over a beer.

I would also like to thank Dr.'s Stephen Payne and Laurent Kreplak for being on my committee and for their advice and help.

Thank you to former group members Brenden Nickerson, Patrick Shea, Yu Xia, Elena Silaeva, Clement Remacha, John Sampson, and Matthew Lobban for their support and friendship. Also, to many friends and colleagues at the Physics Department, past & present.

Finally, I would like to thank whoever invented or discovered coffee and alcohol without which I wouldn't have survived grad school.

This work was funded by the Office of Naval Research, Washington DC and by the Natural Sciences and Engineering Research Council of Canada (NSERC).

.

CHAPTER 1 Introduction

Electrostatic fields inside atoms and molecules are of the order of volts per ångström, such high fields can also be maintained over macroscopic distances at field emission tips. These fields are strong enough to cause the rearrangement of the electronic orbitals of the molecules and atoms leading to new phenomena which can be described as field-induced chemistry and field-induced chemisorption. There have been several review articles written about these topics by Kreuzer and Block et al [1]–[5].

For discussion purposes, the effects of electric fields on matter can be split into two regimes: physical and chemical. Physical effects occur in low fields (< 0.1 V/Å) and result in the atoms, molecules, and condensed matter becoming polarized. Chemical effects occur in larger fields and are due to the electronic orbitals becoming distorted such that the chemical characteristics of atoms and molecules are altered, e.g. by establishing new bonding or anti-bonding orbitals. Thus, a strong electric field can stabilize molecules that are unstable under field-free or low field conditions. This can open up new pathways in chemical reactions previously unseen.

In this work we will examine the effects of high electric fields on dielectric and low-, medium, and high-bandgap semiconductive materials using H_2O, Si, ZnO, and MgO, respectively, as specific examples. Density Functional Theory (DFT) was used throughout to calculate field effects and the computational methods and algorithms are discussed in this chapter. The effects can be constructive as mentioned above with the formation of new structures. In Chapter 2 we will look at this field-induced chemistry and the changes in the Molecular Orbital (MO) energy levels caused by the electric field and the resulting transformed structure, electronically and physically. With a sufficiently strong field we show the electronic transformation of N_2 into CO.

With a sufficiently strong applied field the effects will be destructive i.e. the material will break apart and ionize. This Field Evaporation (FE) of the material is discussed in Chapters 2-6. We examine the role of MOs in the FE process specifically the gap between the Highest Occupied Molecular Orbital (HOMO) and Lowest Unnoccupied

Molecular Orbital (LUMO). As well as compare the evaporation products calculated with experimental results from Atom Probe Tomography (APT); see section 1.2 for a description of APT.

Of course when looking at applied field effects one should also look at changes of the local field and not just MOs and evaporation products. In Chapters 3-4 we calculate the effects of the applied field on the local fields both interior and exterior to the material to determine the induced electric field. The local enhancement or reduction of the induced field is then compared with that of conductors and of classical electrostatics. We find it is possible that internal fields are reduced by over 100X indicating that the material has become conducting. We explore this field-induced metallization further in Chapters 3-5. We present evidence for this effect from the closure of the HOMO-LUMO gaps, field expulsion from the material, and changes in the dielectric constant and polarizability. Experimental confirmation of bandgap closure or reduction is discussed in Chapter 5. Also, we calculate the depth of this metallization and show that it is predominantly a skin effect.

In Chapter 7, we follow the quantum mechanics of charge transport along linear water structures called proton wires both with free ends and donor/acceptor terminated. By increasing the applied field we examine the stability and structural changes of these linear water structures which in the literature are referred to as water whiskers, water wires, or water chains. For clarity we will refer to these linear water structures as water whiskers if unprotonated and as proton wires if protonated for the remainder of the thesis. We present whisker structures and energetics, lower and upper threshold fields, and fragmentation patterns. Finally in Chapter 8 we end with the conclusions.

In the remainder of this chapter we provide the necessary background information and preliminaries. In section 1.1 we begin with a review of classical electrostatics for conductors and dielectrics.We review in section 1.2 how high electric fields are generated experimentally and give a brief overview of the technique known as Atom Probe Tomography which uses such high fields. Atom probe results depend on field

evaporation which is discussed in section 1.3; specifically several models for the FE of metals. An introduction to MO theory is given section 1.4. Because DFT underlies all of our calculations, we give an overview in section 1.5. Finally, the computational methods used are discussed in section 1.6.

A common physical effect has emerged in [1]–[5], namely that in a high electrostatic field the rearrangement of the bonding and antibonding orbitals or field-induced chemistry can cause: (i) the electronic transformation of one material into another creating a continuous periodic table, (ii) the formation of new structures which are stable in the field, and (iii) field-induced dissociation or field evaporation. We perform detailed quantum mechanical calculations using density functional theory to explain experimental observations, exhibit applications, and explore the above effects.

1.1 Classical Electrostatics in Matter

In this section we will review the classical effects of electric fields on matter for the purposes of comparison with later parts of the thesis.

1.1.1 Metals

In an insulating material each electron is bound to a particular atom. However, in a metallic conductor one or more electrons are unbound or free to move through the material. A perfect or ideal conductor would contain an unlimited supply of free electrons but such materials don't exist. Many however come close so we list the electrostatic properties of an ideal conductor below [6]:

1. The electric field $\boldsymbol{E} = 0$ inside the conductor. The applied electric field will cause a separation of charge in the conductor. These induced charges will generate their own electric field which is equal and opposite to the applied field. Thus the net internal field will be zero.
2. The charge density $\rho = 0$ inside the conductor. Local charges exist but the net density is zero.

3. Any net charge is on the surface of the conductor. The mutual repulsion of the charges will distribute the charge over the surface.

4. A conductor is an equipotential surface.

5. The electric field just outside the surface of the conductor is perpendicular to the surface.

We now turn our attention to dielectrics.

1.1.2 Dielectrics

As mentioned above insulators or dielectrics contain electrons which are tightly bound. The electric field can distort the charge distribution of a dielectric atom or molecule through two effects: rotation and stretching. We'll look at these effects first on an atom or molecule before looking at bulk dielectric properties. If a neutral atom is placed in an electric field then the field will cause a displacement of the electron cloud away from the nucleus, opposite to the applied field direction. The electric field will cause a force trying to separate the nucleus from the electrons while the Coulombic interaction between the nucleus and electrons will try to keep the atom together. If the field isn't too strong, then the forces on the atom will reach equilibrium leaving the atom polarized. This separation of charge means the atom now has an induced dipole moment $\boldsymbol{p}$ which is oriented in the field direction. The induced dipole moment is approximately proportional to the applied field with the caveat that the field isn't too strong [6]:

$$\boldsymbol{p} = \alpha \boldsymbol{E} \tag{1}$$

where α is the atomic polarizability and its value is material dependent. If the field is strong enough, then the electrons will be ripped away from the nucleus, ionizing the atom. For a molecule the polarization isn't necessarily uniform and the constant α must be replaced with a polarizability tensor.

A molecule with a permanent dipole moment is called a polar molecule; water for example is a polar molecule. Placing a polar molecule in a uniform electric field will generate a torque $\boldsymbol{N}$ causing the molecule to rotate:

$$\boldsymbol{N} = q\boldsymbol{d} \times \boldsymbol{E} = \boldsymbol{p} \times \boldsymbol{E} \tag{2}$$

where q is the charge separated by a distance $\boldsymbol{d}$. The torque will align $\boldsymbol{p}$ parallel with $\boldsymbol{E}$. For a nonuniform field there is also a net force $\boldsymbol{f}$ in addition to the torque:

$$\boldsymbol{f} = (\boldsymbol{p} \cdot \nabla)\boldsymbol{E}. \tag{3}$$

Now that we have looked at atoms and molecules, what about the effects of an electric field on a bulk material? If the material consists of nonpolar molecules, then the field will induce dipole moments in the molecules and align them in the field direction. This still holds for randomly oriented asymmetric crystals but not single crystals which are more complicated. For a material consisting of polar molecules the field will rotate the molecules to align the dipole moment in the field direction. However, random thermal motion will prevent the molecules from being perfectly aligned. Regardless then of the mechanism that aligns the individual dipole moments in the material, it becomes polarized with a polarization $\boldsymbol{P} \equiv \boldsymbol{p}/V$ where V is unit volume [6].

Linear dielectrics are substances where the polarization is proportional to the electric field (again provided the field isn't too strong):

$$\boldsymbol{P} = \epsilon_0 \chi_e \boldsymbol{E} \tag{4}$$

where ϵ_0 is the permittivity of free space, and χ_e is the electric susceptibility of the material. The value of χ_e is material and temperature dependent. It should be noted that in Eq. 4, $\boldsymbol{E}$ is the total field thus the polarization will depend on the field produced by the polarization itself. It is best to use electric displacement $\boldsymbol{D}$ to break out of this self-dependence:

$$\boldsymbol{D} \equiv \epsilon_0 \boldsymbol{E} + \boldsymbol{P} = \epsilon_0 \boldsymbol{E} + \epsilon_0 \chi_e \boldsymbol{E} = \epsilon_0 (1 + \chi_e) \boldsymbol{E}, \tag{5}$$

so $\boldsymbol{D}$ is proportional to $\boldsymbol{E}$ and the proportionality constant $\epsilon_0(1 + \chi_e) = \epsilon$ is called the permittivity of the material. A more useful quantity for this thesis is the relative permittivity or dielectric constant ϵ_r:

$$\epsilon_r \equiv 1 + \chi_e = \frac{\epsilon}{\epsilon_0}. \tag{6}$$

The dielectric constant has values of 1 (vacuum), 80.1 (water), etc [6]. The electric field in a homogenous linear dielectric is reduced by a factor of one over the dielectric constant

$$\boldsymbol{E} = \frac{1}{\epsilon}\boldsymbol{D} = \frac{\mathbf{1}}{\epsilon_r}\boldsymbol{E}_{\boldsymbol{vacuum}}. \tag{7}$$

This implies that the dielectric constant inside of a metal, where the field is zero, approaches infinity. This is discussed further in Chapters 3-5.

1.2 Atom Probe Tomography (APT)

The atom probe, developed by Müller et al in 1968 [7], uses field evaporation for the identification of the atomic composition of micro- and nano-specimens. It is based on the field ion microscope invented by Müller in 1951 [8]. In atom probe microscopy (APM), high electric fields are induced at the sample surface. In metallic materials the electric field penetration is very small (< 1 Å) and is effectively screened on an atomic scale. Thus, only surface atoms are affected by the field evaporation process which evaporates the surface atom by atom and atomic-layer after atomic-layer. In non-metallic materials the field penetrates more deeply into the specimen leading to the evaporation of complex ions, since more than one atomic layer is being affected by the field. Figure 1.1 shows the typical set up of an atom probe.

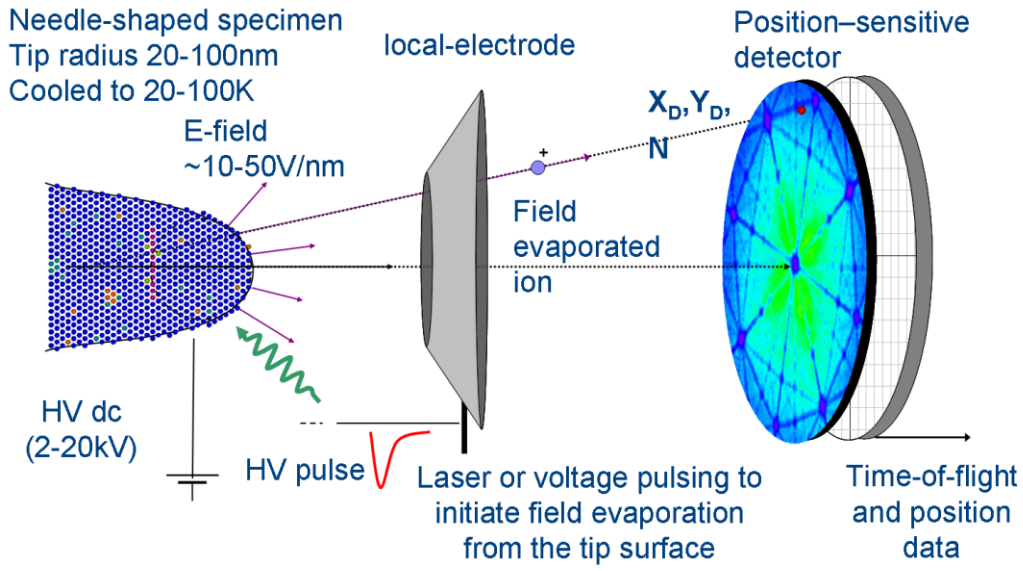

Figure 1.1 Schematic of a typical atom probe set up [courtesy of University of Oxford atom probe group].

The needle-shaped specimen is placed in an ultra high vacuum chamber with a base pressure less than 10^{-8} Pa. The specimen is mounted on a movable stage controlling the position of the specimen in front of the local-electrode or counter electrode. The tip is then cooled to cryogenic temperatures (~ 20 K) to improve spatial resolution. Lower temperatures reduce thermal agitation and diffusion of the surface atoms, thus increasing confidence that the atoms observed are in their original locations and not redistributed by the electric field. A high-voltage (2-20 kV) DC power supply is connected to the sample to generate the required electrostatic field. A high voltage pulser is connected to the counter electrode which is positioned in front of the sample. In pulsed field evaporation there are two mechanisms to control the field evaporation process. One is to increase the electric field at a constant temperature and the other is to increase the temperature while keeping the electric field constant. They are known as high-voltage pulsing and laser- or thermal pulsing, respectively. The high-voltage pulser delivers negative high voltage pulses lasting a few nanoseconds. For atom probes with laser pulsing, the beam of a pulsed laser is focused onto the apex of the tip through a window in the chamber or using in-vacuum optics. Solid-state and gas lasers have been used with pulse durations of nanoseconds down to femtoseconds. The use of pulsed field evaporation allows precise control over the instant in time when the ion departs from the tip's surface and permits an accurate determination of the time of flight (TOF), the time between application of the evaporating field pulse and the measurement of the ion by the detection system. The TOF of the ion is directly related to its kinetic energy and can be used to measure several parameters related to the motion and to determine the mass-to-charge ratio. The measurement of the mass-to-charge ratio enables the identification of the elemental species. Field evaporated ions are collected by a detector that provides information on timing and the position of impact of each ion on the detector. With time-of-flight measurements and the ability to record the position of the ions impact, the tomographic atom probe was developed and three dimensional reconstructions of the analysed volume became possible. This technique is now known as atom probe tomography [9].

In the analysis of APT data the distribution of the electric field and potential determines the projection geometry of an ion, field evaporated from the specimen, on the detector plane. Moreover, the local field variation at the atomic scale controls the initial stage of the evaporation process and, thus, introduces aberrations into the ionic trajectories and ion energy spread, limiting the atom probe spatial and mass resolution. In addition, field penetration deep into the bulk of an insulating or semiconducting specimen leads to the disintegration and rupture of the specimen and affects the laser absorption during laser-triggered field evaporation [10].

For a metallic tip the macroscopic field $E(\mathbf{r})$ and potential $V(\mathbf{r})$ distribution is obtained from the Laplace equation ($\Delta V = 0$) with the boundary conditions that there are no charges inside the vacuum chamber and the field is zero in the metallic specimen. For hemispherical, paraboloid and hyperboloid tips the field distribution is known analytically [11]. The field value E at the tip apex can be approximated by $E_0 = V_0 / \kappa R$ [12] where V_0 is the applied potential between the tip and a flat counter-electrode, R is the apex radius and κ is a dimensionless factor that varies with the exact tip geometry[10].

The situation is more complex for semiconductor and dielectric tips for which the free-charge density is much lower than in metals. For insulating tips one can assume that the carrier density inside the tip is zero because APT experiments are usually performed at temperatures below 100 K, where only a very low density of conduction electrons and valence holes are excited thermally. In this case, the field inside the tip is, on the macroscopic scale, the applied field divided by the dielectric constant, producing a large potential drop at the tip apex [13], [14]. For a dielectric layer on a metallic tip one gets approximately at the tip apex [15]

$$E_0 = \frac{\epsilon_r R}{(\epsilon_r R + d)} \frac{V_0}{\kappa R}, \tag{8}$$

where ϵ_r is the dielectric constant of the layer and d is its thickness. Thus, for rather thick dielectric layers, the field at the apex can be many times lower than the one found at the apex of metallic tips [10].

However, experiments show that the field values for both metallic and insulating tips are quite similar and the potential drop at the dielectric tip apex is less than 1% of the applied voltage [16]. This implies a substantial free-carrier density inside the insulating tip, and a better way to describe the field distribution is to solve the Poisson equation coupled to the transport equations for the free carriers, taking into account the dielectric constant of the specimen. As a result, the free electrons will separate from the free holes in order to screen the external field inside the tip, and the potential at the tip apex will correspond to the one applied to the tip base [17]. A simple estimate how long it takes to establish this separation after the external field has been switched on or changed is given by the dielectric relaxation time $\tau = \epsilon\epsilon_0\rho$ where ϵ_0 is the permeability of free space and ρ is the resistivity of the specimen. For MgO at 100 K the internal field will take more than 2 h to be established. This is in stark contradiction to both APT experiments and also to field evaporation observed in the field ion microscopy which show that relaxation is very fast. To understand this discrepancy one has to find extra carriers and also consider the initial high fields inside the insulator as a driving force for charge separation, thus faster screening and hence shorter relaxation times. This discrepancy can be understood and resolved in a microscopic approach which shows that in high electric fields in insulators and semiconductors the band gap is drastically reduced as will be discussed in Chapters 2-5 [10].

1.3 Field Evaporation of Metals and Dielectrics

The application of a high kilovoltage to a nanometric metallic tip generates an electric field at the surface of the metal on the order of volts per angstrom. This voltage induces free electrons to move inwards towards the bulk leaving an electron deficiency at the surface. The electric field is generated by the presence of the positively charged surface atoms. At the edges and kink sites, the atoms have a greater positive charge, as illustrated

in Figure 1.2.

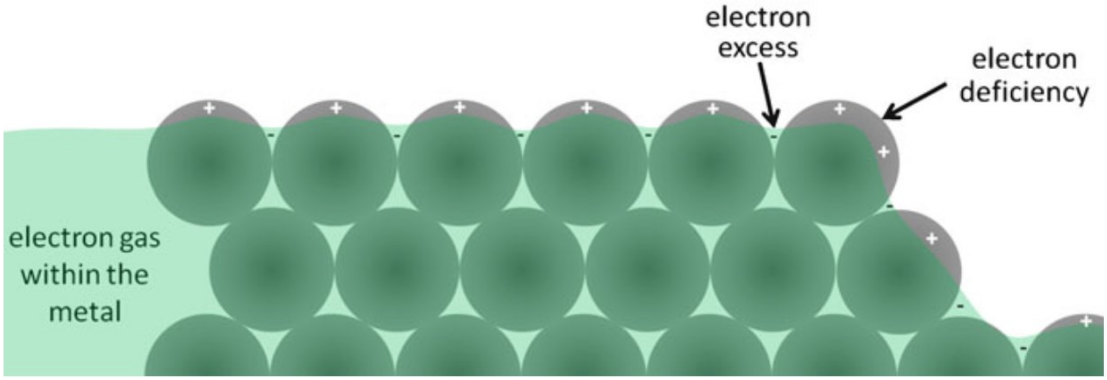

Figure 1.2 Side view illustration of a positively charged metal surface [9].

As the electric field is directly proportional to the surface charge density, the field is strongest above these sites. If the electric field is sufficiently strong, then the atom can be pulled away from the lattice while an electron drains into the surface. The atom is now ionized and is accelerated away from the surface by the electric field. This field induced removal of the atom from its lattice site is called field evaporation [9]. There are many different models for the exact mechanism of FE and an excellent overview is given by Miller and Forbes [18]. We will review the Gomer or charge draining model [19], which is the most widely accepted, and the Kingham-Haydock model on post-ionization [20], followed by the Kreuzer model [21], [22] which improves upon the former models. Also, electron tunneling in an electric field will be discussed.

1.3.1 Gomer Model

This model was originally proposed by Gomer for the field desorption of electronegative gases. It was adapted by T.T. Tsong for the field evaporation of metals by viewing the field evaporation process as a draining of electronic charge from the surface atom as thermal vibrations move the atom away from equilibrium. The Gomer model treats FE as a transition, for an atom A and metal M, to go from the $A + M$ atomic state to the $A^{n+} + M^{n-}$ ionic state. The potential energy curves for the atomic state V_a (z, $E=0$) and the ionic

state V_i (z, $E=0$) in the absence of a field are shown in Figure 1.3. Far away from the surface, the ionic state will be higher in energy than the atomic state by a factor of $\Sigma_i I_i - n\varphi$. This is simply the energy needed to ionize the atom into an n+ ion minus the energy of the n electrons returned to the metal surface, where φ is the work function of the metal. Once a field is applied, the atomic curve V_a (z, E) is slightly lowered due to polarization and the ionic curve V_i (z, E) is lowered greatly by $-nqEz$. The atomic and ionic curves will intersect at a point z_c close to the equilibrium distance z_0 of the surface atom provided the field is sufficiently strong. The atomic state has a higher energy than the ionic state after z_c. If the thermal vibration of the surface atom exceeds this critical distance then it's possible for the atom to undergo an electronic transition into the ionic state and be accelerated away from the surface as an ion. The activation energy Q_n is given by

$$Q_n(E) = V_i\,(z_c, E) - V_a\,(z_0, E)\,. \tag{9}$$

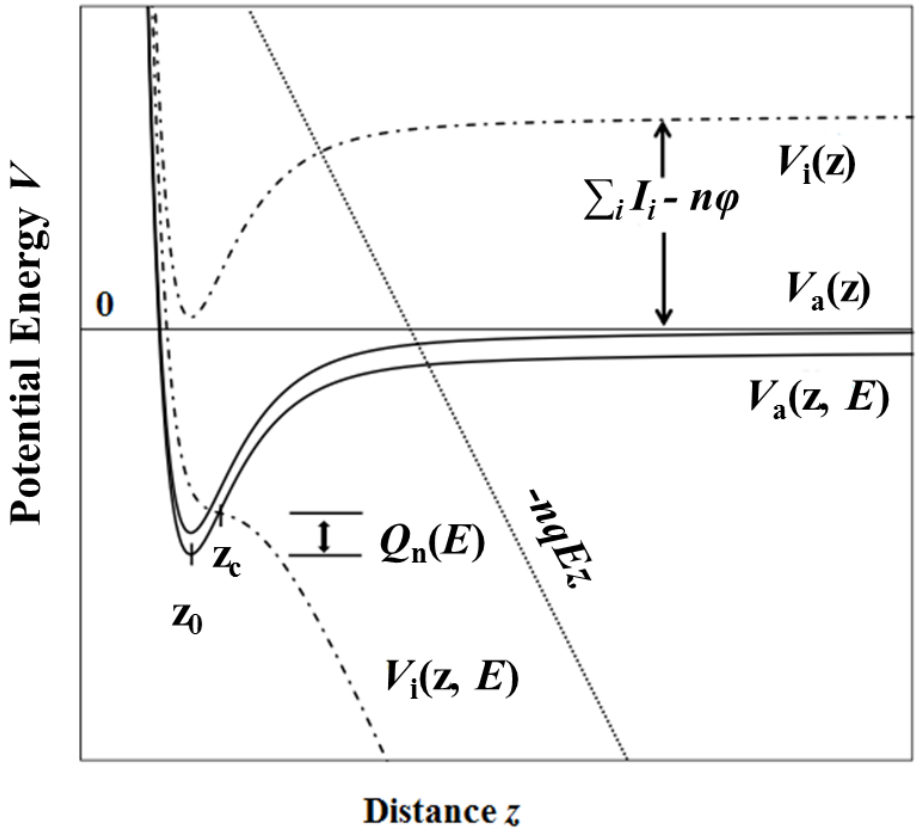

Figure 1.3 Potential energy diagram of the atomic, V_a, and ionic states, V_i, in the Gomer model.

To calculate the activation energy then requires explicit forms for the atomic and ionic states. The atomic state is approximated by

$$V_{\mathrm{a}}\,(z_0, E) \cong -\Lambda(E) - \tfrac{1}{2}\alpha_{\mathrm{a}}(z_0)E^2 - \tfrac{1}{24}\gamma_{\mathrm{a}}(z_0)E^4 \tag{10}$$

where Λ is the field dependent binding energy of the surface atom, α_a is the polarizabilty, and γ_a is the hyperpolarizabilty [19]. The ionic curve is given below and is more complicated due to an energy level shift, broadening effects, and field penetration [19],

$$V_{\mathrm{i}}\,(z_{\mathrm{c}}, E) \cong \Lambda + \sum_{i}^{n} I_i - \frac{\Gamma}{2} - \Delta V - n\varphi(E) - nqEz_{\mathrm{c}} - \frac{1}{2}\alpha_{\mathrm{i}}E^2 - \frac{1}{24}\gamma_{\mathrm{i}}E^4 - \frac{n^2q^2}{4(z_{\mathrm{c}} + \delta)} + \sum_{j}\frac{K}{r_j^{p}(E)} \tag{11}$$

where ΔV is the energy shift, Γ is the broadening effect, φ is the work function taking into account field penetration, δ is the field penetration depth, and α_i and γ_i are the n charged ion polarizabilty and hyperpolarizabilty. The second last term is the ion image potential modified by the field penetration. The last term represents a Lennard-Jones type repulsive interaction between the ion and ionic cores of the metal. These forms for the ionic and atomic potentials are often too unwieldy to use for data analysis and are frequently approximated by simpler models [19].

A simpler model by Tsong , based on the Gomer model, is more frequently used to calculate the evaporation field [23]. The field strength at which the activation barrier decreases to zero is defined as the evaporation field E_{ev}. The evaporation field of n-fold charged ions is given by

$$E_{\mathrm{ev}} \cong \frac{1}{nr_0}\left(\Lambda + \textstyle\sum_i^n I_i - n\varphi - \frac{3.6n^2}{r_0}\right)\mathrm{V/\AA} \tag{12}$$

provided that Λ, I, and φ are in eV, and the atomic radius r_0 is in angstroms. Tsong calculated the evaporation fields and charge states for different metals using this model and found them to be in good agreement with experimental observations at the time but was unable to account for multiple charged states that occurred during nanosecond high voltage pulsing [19].

1.3.2 Kingham-Haydock Model

Haydock and Kingham came forth with a model to account for the multiply charged ions using the charge-draining model as the basis for initial evaporation [20]. Their model proposes that all ions leave the surface singly charged and are re-ionized or post-ionized in the vicinity of the tip. It's possible for the high electric field to ionize the atom several times as it leaves the vicinity of the tip. Figure 1.4 illustrates the potential energy of an ion in a potential qEx near a metal surface in an electric field E. An electron in the outer shell of the ion can tunnel through the energy barrier into an empty energy level in the metal surface. However, this is only possible if the electron energy level coincides or is higher than the Fermi level in the metal. The critical distance, x_c, this post-ionization occurs from the surface for the (n+1)th ionization is given by

$$x_c = \frac{I_{n+1} - \varphi}{E} \tag{13}$$

where $I_{(n+1)}$ is the (n+1)th ionization energy. The probability for an electron to tunnel through the energy barrier is dependent on the electric field and the time the ion is in the ionization zone. This means the post-ionization probability depends on the ion's kinetic energy. Their model was found to explain discrepancies in the charge states of Rh and W. Thus, the model was used to calculate the relative frequency of each charge state versus electric field to produce what are known as Kingham curves. For better or worse, the FE community has adopted these curves [9], [20].

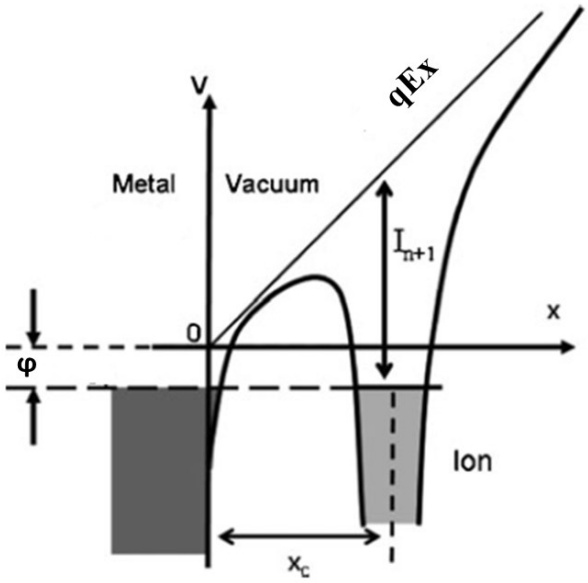

Figure 1.4 Potential energy diagram of an ion in state I_n subject to an electric field E near a metal surface [9]. The potential is qEx, $I_{(n+1)}$ is the $(n+1)$th ionization energy, φ is the work function of the surface, and x_c is the critical distance for post-ionization.

1.3.3 Kreuzer Model

The macroscopic field distribution, described above in 1.2, is obtained using classic electrodynamics, assuming a continuum with a smooth tip surface. At the atomic scale, however, the tip surface must have multiple heterogeneities like ledges, steps, and kink sites due to the discrete nature of the atoms. Also, the classic description considers that the field drops abruptly to zero at the metallic surface and decreases discontinuously by a factor of ϵ_r at the dielectric surface. However, in reality the electron distribution and electric fields vary smoothly over distances of a few angstroms on real surfaces. A jellium model [24]–[26] has these features. The jellium model of a metal assumes that the ionic lattice can be smoothed into a uniform positive charge density that drops to zero abruptly half a lattice constant above the topmost lattice position. The electron density and the local field distribution can be calculated using, for instance, density functional theory.

Density functional calculations have been performed to deal with a lonely metal atom on a flat metal surface in an external field [24]. In Figure 1.5 the equipotential lines around

the atom and also the classical approximation around a metallic hemisphere are shown. In Figure 1.6 they show the external electrostatic field along a line perpendicular to the surface. Curve A, calculated with DFT, is along a line laterally far from the adatom showing the smooth variation over several angstroms rather than an abrupt change as predicted by macroscopic electrostatics. Curve B is the field along a line through the center of the atom and curve C is the classical result approximating the atom by a hemispherical boss. Compared with the field in the absence of the adatom, we note the expulsion of the field from the adatom region which, in turn, results in an enhancement of the field just outside the adatom but not by as much as classical theory predicts. Rather, the partial field penetration into the adatom region results in a smearing out of the field, as a reflection of the adjustability of the electronic distribution at the surface [10], [24].

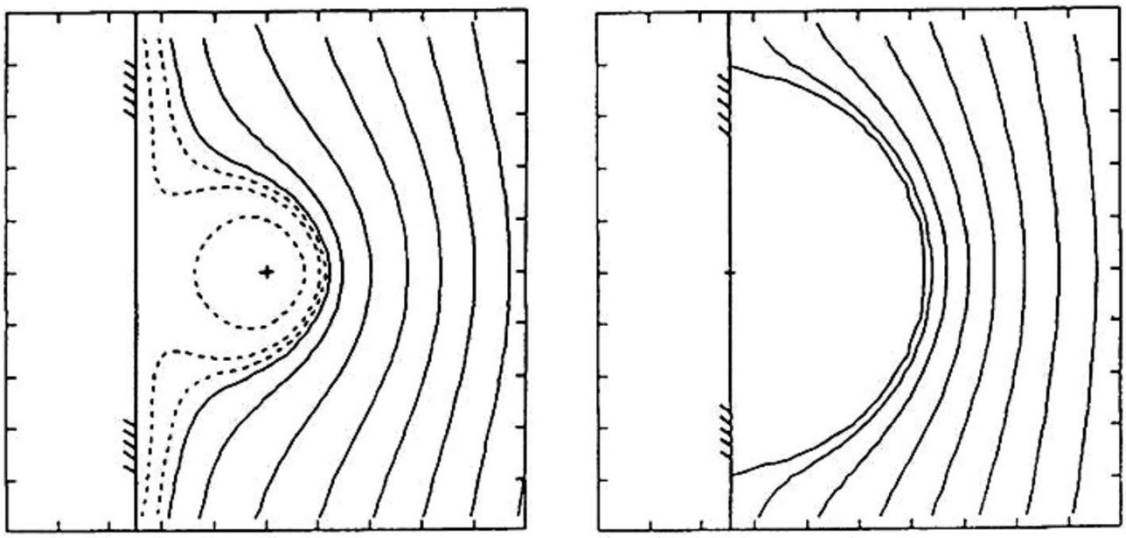

Figure 1.5 Electrostatic equipotential map for a Nb atom on a metal surface. Left: DFT calculations; right: metallic hemisphere (classical) [24].

Evaporation field strengths have been calculated using this model yielding good agreement with experimental values. In the past decade it has become possible to calculate the local field distribution above a ‘real’ metal surface using gradient-corrected exchange-correlation potentials with density functional theory. Details such as field-induced surface reconstruction and relaxation can be calculated. Precision measurements of field ion appearance energies by Block’s group [22], [27]–[29] have confirmed the local field enhancements predicted in Figure 1.6. This is crucial to understand field ion

imaging and the preferential field evaporation of kink, edge, and ledge atoms in APT of metals.

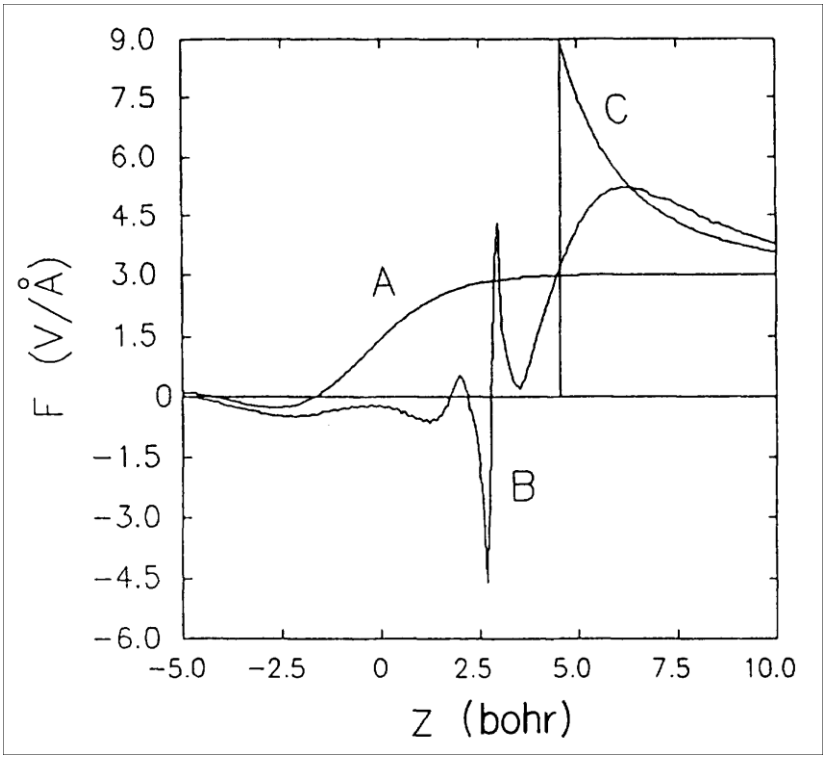

Figure 1.6 Electrostatic field along a line perpendicular to the surface. Curve A along a line laterally far from the adatom predicted by DFT, curve B is the field along a line through the center of the atom and curve C is the classical result approximating the atom by a hemispherical boss [24].

Kreuzer *et al* also developed a first principles theory of the kinetics of field evaporation [21]. They start from the observation that the potential energy curves, V_a (z, $E=0$) and the curve that starts as V_a (z, E) close to zero and transitions to V_i (z, E) at z_c, shown in Figure 1.3, are the quantum-mechanical ground state of the system in the adiabatic approximation; which assumes that the nuclei are infinitely heavy and the electrons follow instantaneously the "motion" of the nuclei. Following a potential energy curve note that inside the hump the atom is essentially neutral with small charge transfers for increased binding but far from the surface it is an ion. The transition from neutral to ion occurs around the potential hump. To quantify this picture one needs the potential energy curve for the first excited state for which the atom is neutral far from the surface and

becomes an ion on close approach. The two curves are shown schematically in Figure 1.7. To calculate the transition rate for the departing atom to get excited one must consider diabatic energy curves along which the neutral and ionic character does not change, see the dashed curves in Figure 1.7. They can be obtained via an orthogonal transformation from the adiabatic states even though they are not true eigenstates of the full Hamiltonian but they contribute off-diagonal elements in their interaction matrix, which, when coupled to the phonons of the substrate lead, e.g. via Fermi's Golden rule, to transition rates for ionization. The theory is quite involved (and won't be discussed in this thesis) but has been worked out in detail and applied very successfully to field desorption of He, and field evaporation of metals and polymers [10], [21], [30], [31].

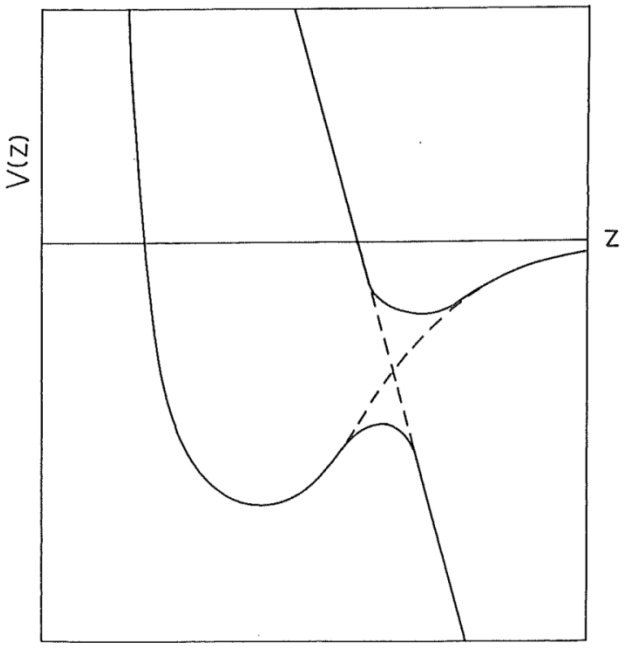

Figure 1.7 Sketch of adiabatic (solid) and diabatic (dashed) potential energy curves for an atom at a distance *z* above a surface [10].

1.3.4 Electron Tunneling

Quantum tunneling is a microscopic phenomenon where a particle, such as an electron, can penetrate and pass through a potential barrier. This barrier is assumed to be higher than the kinetic energy of the particle, therefore such a motion is not allowed by the laws of classical dynamics. The simplest problems in quantum tunneling are one-dimensional and we restrict ourselves to such in this work.

To calculate the tunneling probability of a particle through a potential barrier one needs to find a solution to the time independent Schrödinger equation

$$\left[-\frac{\hbar^2}{2m}\frac{d^2}{dx^2} + V(x)\right]\psi(x) = E\psi(x) \tag{14}$$

where m is the mass of the particle, $V(x)$ represents the barrier, $\psi(x)$ is the particle wavefunction, and E is the particle energy. For simple tunnelling-barrier models, such as the rectangular barrier, an analytic solution exists. More complicated barriers are solved using semiclassical or quasiclassical methods such as the WKB approximation.

The WKB approximation, named after Wentzel, Kramers, and Brillouin, is a method for obtaining an approximate solution to a time-independent one-dimensional differential equation, in this case the Schrödinger equation. Its principal application here will be in calculating tunneling rates through potential barriers. Note that the WKB approximation involves what is called the classical turning point, the point at which the potential energy V is approximately equal to the total energy E. This is the point at which the kinetic energy equals zero, and marks the boundaries between regions where a classical particle is allowed and regions where it is not; hence, the semiclassical nature of the approximation [32].

We'll look at the case of an electron tunneling through a barrier in the presence of a high electric field and use the WKB approximation to find the tunneling probability. The potential barrier $V(x)$ is shown in Figure 1.8.

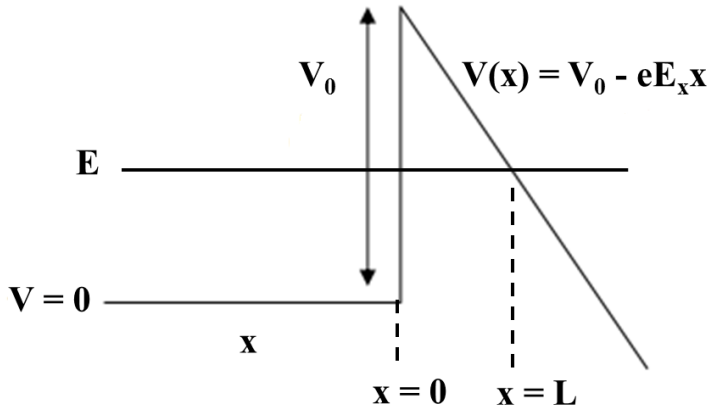

Figure 1.8 Schematic of a triangular potential energy barrier.

We begin by rewriting Eq. 14 as:

$$\frac{d^2\psi(x)}{dx^2} = \frac{2m(V(x)-E)}{\hbar^2}\psi(x) \tag{15}$$

Between x and $x+dx$ this equation can be solved yielding:

$$\psi(x+dx) = \psi(x)\exp\left(-\sqrt{\frac{2m(V(x)-E)}{\hbar^2}}\,dx\right) \tag{16}$$

For a slowly varying potential the amplitude of the wavefunction at $x = L$ can be related to the wave function at $x = 0$:

$$\psi(L) = \psi(0)\exp\left(-\int_0^L \sqrt{\frac{2m(V(x)-E)}{\hbar^2}}\,dx\right) \tag{17}$$

From this the tunneling probability T, can be calculated for a triangular barrier for which $V(x) = 0$ for $x < 0$ and $V(x) = V_0 - eE_x x$ for x > 0 where V_0 is the barrier height and E_x is the electric field:

$$T = \frac{\psi(L)\psi^*(L)}{\psi(0)\psi^*(0)} = \exp\left(-2\int_0^L \sqrt{\frac{2m}{\hbar^2}}\sqrt{V_0 - eE_x x}\,dx\right) \tag{18}$$

the tunneling probability then becomes [32], [33]

$$T = \exp\left(-\frac{4}{3}\frac{\sqrt{2em}}{\hbar}\frac{V_0^{3/2}}{E_x}\right) \tag{19}$$

1.4 Molecular Orbital Theory

Analogous to an atomic orbital (AO), a molecular orbital (MO) represents a region where an electron in a molecule is likely to be found. In principle the Schrödinger equation allows the calculation of the molecular wavefunction but is more difficult to solve than in the case of the many-electron atom. Several simplifying assumptions have to be made which then provide an approximation of the real situation. The first is the Born

Oppenheimer approximation [34]. This approximation writes the total wavefunction $\boldsymbol{\Psi}(\boldsymbol{r}, \boldsymbol{R})$ as a product of the nuclei wavefunctions $\boldsymbol{\Xi}(\boldsymbol{R})$ and electrons wavefunction $\boldsymbol{\Phi}_{\text{el}}(\boldsymbol{r})$

$$\boldsymbol{\Psi}(\boldsymbol{r}, \boldsymbol{R}) = \boldsymbol{\Xi}(\boldsymbol{R})\boldsymbol{\Phi}_{\text{el}}(\boldsymbol{r}) \tag{20}$$

where $\boldsymbol{R}$ and $\boldsymbol{r}$ represent the nuclear and electronic coordinates, respectively. The physical justification is that the nuclei are more massive than the electrons and move very slowly in comparison with the electrons. Thus equation (20) describes a set of mobile electrons moving around fixed nuclei. The problem then reduces to solving the $\boldsymbol{\Phi}_{\text{el}}(\boldsymbol{r})$ for a given nuclear geometry [35].

An exact analytic solution for the electronic wavefunction of systems containing more than one electron isn't possible so the orbital approximation can be used. Using this approximation, the solution of the many-electron wavefunction is written as a product of one-electron functions

$$\boldsymbol{\Phi}_{\text{el}}(r_1, r_2, \dots, r_n) = \varphi_1(r_1)\varphi_2(r_2) \dots \varphi_n(r_n) \tag{21}$$

where the one-electron functions φ_i are the molecular orbitals of the system [35].

The form of the molecular orbitals can be described using the linear combination of atomic orbitals (LCAO) approximation. Each MO is written as a linear sum of contributions from the AO's of the molecule χ_j

$$\varphi_i = \sum_j c_{ij}\, \chi_j \tag{22}$$

where the c_{ij} are the weights of the AO χ_j in the MO. The physical justification for this is that an atom in the interior of the molecule retains many of the characteristics of an isolated atom. In principle the χ_j are known and consist of an infinite number of functions for each atom. In order for the problem to be solveable, two approximations are used to truncate the sum: (1) Core electron orbitals are ignored. They are centered close to the nucleus and play negligible roles in chemical bonding. (2) Only occupied valence orbitals and empty orbitals with the same principal quantum number as the valence orbitals are used. Calculating the MOs, thus reduces to solving for the coefficients c_{ij} which characterize it. This can be done by the variational theorem which leads to a direct determination of the c_{ij}, which can then be used to calculate the energy of the system $E_{\text{system}} = \sum \varepsilon_i$ where ε_i is the energy of the ith orbital [35].

A qualitative approach based on symmetry and relative energies of the AOs of the isolated atoms is also quite useful for understanding the electronic and chemical behaviour of the molecule; we use a diatomic heteronuclear molecule AB as a simple example. We assume that each atom has only a single AO (χ_1 on A and χ_2 on B) and they each have a different energy, χ_2 being lower. The wavefunctions of the AOs interact with a degree of interaction determined by the overlap integral $< \chi_1 | \chi_2 > = S$, with $S = 0$ indicating no interaction. Depending on the symmetry of the interacting AOs, the probability density functions for the MOs may be enhanced or reduced between the two atoms. An enhancement is due to the AOs being in phase and indicates that the electron has an increased probability of being found between the two atoms. The kinetic and potential energy of the electron are reduced leading to an energetic stabilization of the MO which is called the bonding orbital φ_+. The bonding orbital lies lower than the AOs. A reduction is due to the AOs being out of phase and indicates that the electron is unlikely to be found between the two atoms. There is no stabilization in this region, in fact the electron is more unstable here than in an isolated AO. This MO is higher in energy than the AOs and is called the antibonding orbital φ_-. Orbitals with no interaction are called non-bonding orbitals. Their energy is almost the same as the AOs of one of the atoms in the molecule except for small shifts due to changes in the local field. Core electrons are typical examples [35].

The interaction between the two AOs is illustrated in an interaction diagram shown in Figure 1.9. The bonding orbital φ_+ lies lower than χ_2 by an amount $\Delta E^+ = E(\chi_2)-E(\varphi_+)$ and the antibonding orbital φ_- is higher than χ_1 by $\Delta E^- = E(\varphi_-)-E(\chi_1)$. In general, $\Delta E^+ < \Delta E^-$. The MOs are filled according to Hund's rule and the Pauli-Exclusion principle. The presence of two electrons in the bonding orbital and the lack of electrons in the anti-bonding orbital gives rise to a chemical bond. However, if there are two electrons in the antibonding orbital then the bond is destabilized due to $\Delta E^+ < \Delta E^-$. The interaction of two AOs located on two centers is summarized below: (1) Orbitals can only interact if $S \neq 0$. (2) The interaction of two AOs leads to the formation of one bonding orbital and one anti-bonding orbital. In general, *n* AOs leads to *n* MOs. (3) The bonding MO is more

stable than the lowest energy starting AO. (4) The antibonding orbital is less stable than the highest energy starting AO. (5) The bonding orbital is stabilized less than the antibonding is destabilized i.e. $\Delta E^{+} < \Delta E^{-}$. (6) The interaction is proportional to S for degenerate AOs and $S^2/(\varepsilon_1 - \varepsilon_2)$ for non-degenerate AOs, where ε_i is the energy of orbital i. (7) The bonding orbital is localized on the atom with the deeper lying AO and the antibonding on the atom with the higher energy AO [35].

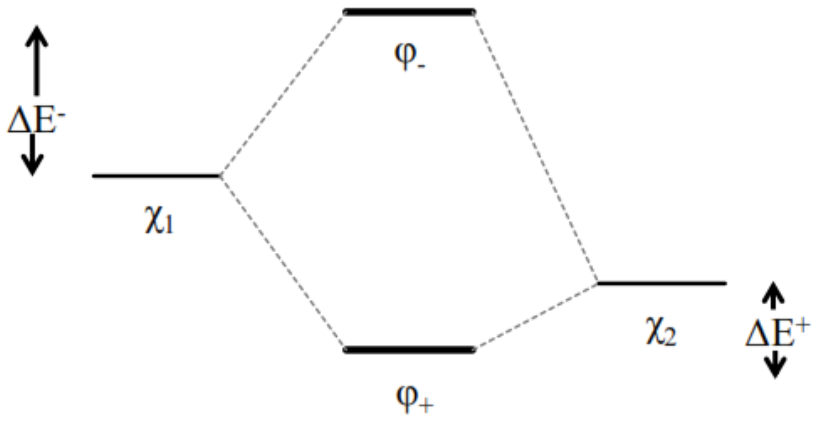

Figure 1.9 Interaction diagram of a heteronuclear diatomic molecule.

The situation becomes much more complex as the number of AOs and MOs increase on the molecules in question. A simplification can be made using the frontier orbital approximation [35] which looks at the interaction of the highest occupied molecular orbital (HOMO) and lowest unoccupied molecular orbital (LUMO) of two molecules to determine how the molecules react with one another. The difference of the energies of the HOMO and LUMO is called the HOMO-LUMO gap. As the molecular system increases in size towards a bulk material, the HOMO-LUMO gap approaches the bulk band gap. Application of a high electric field can raise the MO energy levels causing closure of the HOMO-LUMO gap indicating field-induced metallization of the material. We will look at changes to the HOMO-LUMO gap in electric fields throughout this thesis and discuss implications of its closure.

1.5 Density Functional Theory

Density functional theory is a method used in quantum mechanics to calculate the electronic structure of many-body systems. As is common in many-body electronic structure calculations, the nuclei of the treated molecules or clusters are regarded as generating a static external potential $v_{ext}(\boldsymbol{r})$ in which the electrons follow the motion of the nuclei instantaneously (the Born–Oppenheimer approximation) [34]. The external potential seen by the electrons is then due to the external field from the positively charged nuclei and is defined as

$$v_{ext}(\boldsymbol{r}) = -\sum_I \frac{Z_I q^2}{|\boldsymbol{r}-\boldsymbol{R}_I|} \tag{23}$$

where the $\boldsymbol{R}_I$ are nuclear coordinates of the Ith nucleus, and Z_I is the atomic number. DFT is based upon the Hohenberg-Kohn theorem [36]. This theorem states that for a system of interacting electrons in an external potential $v_{ext}(\boldsymbol{r})$, the ground state electron density, $\rho(\boldsymbol{r})$, is uniquely determined. Thus, the full Hamiltonian is determined since the density $\rho(\mathbf{r})$ is uniquely related to the external potential $v_{ext}(\mathbf{r})$ and the number n of electrons by $n = \int \rho(\mathbf{r}) d^3\,\mathbf{r}$.

The Hohenberg-Kohn theorem also states that a universal functional $E[\rho]$ can be defined in terms of the density. The exact ground state is the global minimum value of this functional. That is to say, the total energy is given by:

$$E = min_{\rho(r)} E[\rho] = min_{\rho(r)}(T[\rho] + V_{ext}[\rho] + V_H[\rho] + E_{xc}[\rho]) \tag{24}$$

$V_{\text{ext}}[\rho]$ is the functional of the external potential. $V_H[\rho]$ is the functional for the Hartree energy. The Hartree energy corresponds to the mean-field electrostatic energy of the electronic charge distribution and is given by

$$V_H = \frac{1}{2}\int d^3\mathbf{r} d^3\mathbf{r}' \frac{q^2\rho(\mathbf{r})\rho(\mathbf{r}')}{|\mathbf{r}-\mathbf{r}'|} \tag{25}$$

$T[\rho]$ is the kinetic energy functional for non-interacting electrons. The exchange-correlation functional $E_{\text{xc}}[\rho]$ contains the interaction between electrons of the same spin (exchange) and opposite spin (correlation). The problem is that this non-local functional

isn't known and may be impossible to determine exactly in a closed form. However, it is a well-defined universal functional of the electron density. Another issue is that the kinetic energy functional $T[\rho]$ is often not well known either so a direct variation of the density isn't usually performed. Instead the density is expressed as a sum over single particle states

$$\rho(\mathbf{r}) = \sum_{i=1}^{n} |\psi_i(\mathbf{r})|^2 \tag{26}$$

Then the variational principle is used to minimize $E[\rho]$ with respect to the single particle states under a normalization constraint. This produces the Kohn-Sham equations [37]:

$$\left\{-\frac{\hbar^2}{2m}\nabla^2 + v_{ext}(\mathbf{r}) + v_H(\mathbf{r}) + v_{xc}(\mathbf{r})\right\}\psi_i(\mathbf{r}) = \varepsilon_i\psi_i(\mathbf{r}) \tag{27}$$

where the one-electron energies are given by ε_i. Thus, in the Kohn-Sham formalism the effective one-electron potential acting on the electrons is

$$v_{eff}(\mathbf{r}) = v_{ext}(\mathbf{r}) + v_H(\mathbf{r}) + v_{xc}(\mathbf{r}) \tag{28}$$

The exchange-correlation potential $v_{xc}(\mathbf{r})$ is determined by

$$v_{xc}(\mathbf{r}) = \frac{\delta E_{xc}[\rho]}{\delta\rho} \tag{29}$$

where $\delta E_{xc}[\rho]$ is the functional derivative of the exchange-correlation functional. Since the exchange-correlation potential and Hartree term depend on the electron density which depends on the ψ_i, which in turn depend on the effective potential, the solution of the Kohn–Sham equation has to be done in an iterative and self-consistent way. One generally starts with an initial guess for the electron density, then calculates the corresponding effective one-electron potential and solves the Kohn-Sham equations for the ψ_i. A new density is calculated and the potentials recalculated. This procedure is then repeated until convergence is reached. This type of procedure involving a self-consistency cycle is also known as a self-consistent field (SCF) approximation.

Thus the ground state energy is expressed as

$$E = \sum_{i=1}^{n} \varepsilon_i + E_{xc}[\rho] - \int v_{xc}\,(\mathbf{r})\rho(\mathbf{r})d^3\mathbf{r} - V_H + V_{nucl-nucl} \tag{30}$$

The nuclear interaction energy $V_{\text{nucl-nucl}}$ has been added in to give the correct total energy of the electronic Hamiltonian. This energy is given by

$$V_{nucl-nucl} = \frac{1}{2}\sum_{I \neq J} \frac{Z_I Z_J q^2}{|\boldsymbol{R}_I - \boldsymbol{R}_J|} \tag{31}$$

The ground state energy expressed in equation 30 is in principle exact. The reliability of any density functional theory calculation for the energy now is crucially dependent on the accuracy of the expression for the exchange-correlation functional. The exchange-correlation functional can be expressed as

$$E_{xc}[\rho] = \int d^3\boldsymbol{r}\, \rho(\boldsymbol{r})\varepsilon_{xc}\big(\rho(\boldsymbol{r})\big) \tag{32}$$

where $\varepsilon_{\text{xc}}(\rho(\boldsymbol{r}))$ is the exchange-correlation energy per particle at a given point $\boldsymbol{r}$. The problem is that the exchange-correlation energy $\varepsilon_{\text{xc}}(\rho(\boldsymbol{r}))$ can't be derived exactly since the exchange-correlation functional isn't well known either. However, the exchange-correlation energy for the homogeneous electron gas is known [38]. It is used in the Local Density Approximation (LDA) to approximate non-homogeneous densities with a homogeneous electron gas. The functional is given by

$$E_{xc}^{LDA}[\rho] = \int d^3\,\boldsymbol{r}\, \rho(\boldsymbol{r})\varepsilon_{xc}^{LDA}\big(\rho(\boldsymbol{r})\big) \tag{33}$$

As can be seen, the non-locality of the true exchange-correlation energy, at any point in space, is replaced by the local exchange-correlation energy of the homogeneous electron gas for the corresponding density. The LDA has been successful in a wide range of bulk and surface problems but has had difficulties modeling chemical reactions in the gas

phase and at surfaces. The LDA often leads to calculated binding and cohesive energies being larger than experimental values. This has led to the advent of the Generalized Gradient Approximation (GGA). The GGA includes the gradient of the density in the exchange-correlation energy and its functional is given by

$$E_{xc}^{GGA}[\rho] = \int d^3\,\boldsymbol{r}\;\rho(\boldsymbol{r})\varepsilon_{xc}^{GGA}(\rho(\boldsymbol{r}), |\nabla\rho(\boldsymbol{r})|) \tag{34}$$

The use of GGA in DFT calculations has achieved chemical accuracy (error ≤ 0.1 eV) for many chemical reactions. The GGA isn't perfect and research into more accurate exchange-correlation functions is still ongoing. One method is the use of hybrid functionals such as the B3LYP functional used throughout the calculations in this work [39]. B3LYP stands for Becke, 3-parameter, Lee-Yang-Parr and is a mix of Hartree-Fock, LDA, and GGA functionals with three parameters determined by fitting to the experimental atomization energies, ionization potentials, proton affinities and first row atomic energies.

1.6 Computational Details

In this section we discuss the computational methods used throughout this work with details on the three main types of calculations done: geometry optimizations, electric fields, and Mulliken charges. All density functional theory calculations were done using the Gaussian09 software programme [40]. Every calculation begins with a choice of the form of the exchange-correlation functional and basis set. This choice is motivated by the trade-off between accuracy and computational time. Larger basis sets can be more accurate but take longer to get results. The B3LYP exchange-correlation functional is used throughout due to its accuracy vs. computational time as compared to other functionals in the computational chemistry database maintained by National Institute of Standards and Technology (NIST) and due to its frequent use in the literature. One must choose between restricted or unrestricted wavefunctions for the calculation. Restricted means that all electrons are paired in each MO i.e. doubly occupied orbitals. Unrestricted

wavefunctions, i.e singly occupied orbitals, are used since they are needed for ions and processes such as bond dissociation.

In Gaussian, basis sets assign a group of basis functions to each atom within a molecule to approximate its orbitals. These basis functions, χ_j, themselves are composed of a linear combination of gaussian functions, called primitives, and are of the form

$$\chi_j = \sum_p d_{jp} g_p \tag{35}$$

Where d_{jp} are fixed constants within a given basis set, and g_p is a primitive gaussian. A primitive gaussian has the general form

$$g(\alpha, \boldsymbol{r}) = c x^n y^m z^l e^{-\alpha r^2} \tag{36}$$

where $\boldsymbol{r}$ is the radial coordinate, x, y, z are Cartesian coordinates, α is a constant determing the radial extent of the function, c is a normalization constant, and n, l, and m are the principal , angular, and magnetic quantum numbers, respectively. A representative s-type gaussian function is given by

$$g_s(\alpha, \boldsymbol{r}) = \left(\frac{2\alpha}{\pi}\right)^{3/4} e^{-\alpha r^2}. \tag{37}$$

The basis set is of the form 6-31G which means that the core orbitals are represented by six gaussians, whereas the inner and outer valence orbitals consist of three and one gaussian, respectively. This is a split valence basis set and in these bases the AO's are split into two parts: an inner, compact orbital and an outer, expanded orbital. The coefficients of these two kinds of orbitals can be varied independently during the construction of the MO. Split valence basis sets allow the orbitals to change size but not shape. Polarized basis sets allow the shape to change by adding orbitals with angular momentum beyond what is required for the ground state description. Polarized basis sets added to heavy atoms are indicated by a (d) or * and (p) or ** for hydrogen [41].

Another factor that must be taken into account is the spin multiplicity of the entire system for an accurate determination of the electronic structure. The spin multiplicity is given by the equation 2S+1, where S is the total spin for the molecule. Paired electrons do not contribute so a singlet (no unpaired electrons) has a spin multiplicity of one and so on to

doublet, triplet, etc. There are of course other parameters involved in the calculations such as total charge but these will be addressed as the need arises. The next three subsections outline the main types of calculations done.

1.6.1 Geometry Optimization

Geometry optimizations attempt to locate minima (local and/or global) on the potential energy surface, thus predicting equilibrium or ground state structures of molecular systems. At the minima the gradient of the energy is zero and since the gradient is the negative of the forces, the forces are zero as well. This is called a stationary point and all successful optimizations locate a stationary point, although not necessarily the intended one.

The geometry optimization begins with an initial molecular structure specified in the input and then proceeds to step along the potential energy surface. Gaussian computes the energy and gradient at that point, and then determines how far and in which direction to make the next step. The gradient indicates the direction along the surface where the energy decreases the most rapidly from the current point and the steepness of the slope. Also, computed is the second derivative of the energy with respect to the molecular coordinates, known as the Hessian, which is a matrix of force constants. These force constants specify the curvature of the surface at that point, which provides information for determining the next step. Gaussian does all this using a variation of the Berny optimization algorithm. The Berny geometry optimization algorithm in Gaussian is based on an earlier program written by H. B. Schlegel which implemented his published algorithm [42]. The program has been considerably enhanced since this earlier version using techniques either taken from other algorithms or never published, the current version is summarized in the Gaussian 09 user's reference [40], [41].

An optimization is complete when it has converged; essentially, when the forces are zero and the convergence criteria have been met. The convergence criteria used by Gaussian are:

- The maximum component of the force on each atom must be below the cutoff value of 0.00045 au, essentially zero.
- The root-mean-square of the forces must be below 0.0003 au.
- The calculated displacement for the next step is less than 0.0018 Bohr.
- The root-mean-square of the displacement is below 0.0012 Bohr.

The presence of four distinct convergence criteria prevents a premature identification of the minimum [41].

A review of different model chemistries in [41] lists the accuracy of a given exchange-correlation functional and basis set as compared with experimental data from the G2 molecule set. This is a set of experimental data consisting of: 55 atomization energies, 38 ionization potentials, 25 electron affinities, and 7 proton affinities taken from first and second row heavy atoms. The model chemistries used in this work, B3LYP/6-31G* and B3LYP/6-311+G*, have mean absolute deviations of 0.34 eV and 0.17 eV, respectively on the G2 molecule set.

The ground state structure of a given system is found by running a geometry optimization for several different multiplicities and taking the optimized system with the lowest SCF energy as the ground state structure. The application of an electric field in the optimization requires some part of the structure remain fixed (a single atom or bottom layer in a cluster) to prevent the system from drifting in the electric field due to the polarization of the system. The multiplicity of the optimized structure can change with the electric field, for example the ZnO molecule is a triplet at zero field but becomes a singlet at 1.2 V/Å. Thus, parallel calculations with different multiplicities are often run for analysis.

1.6.2 Electric Fields

The electrostatic properties of a system in Gaussian are calculated using the PRISM algorithm [43]. The electrostatic potential $V(\boldsymbol{r})$ is rigorously defined as a quantum mechanical expectation value, and is given in the ab initio LCAO framework by

$$V(\boldsymbol{r}) = \sum_A \frac{Z_A}{|\boldsymbol{r}-\boldsymbol{R}_A|} - \sum_{\mu\nu} P_{\mu\nu} \int \frac{\phi_\mu(\boldsymbol{r}_1)\phi_\nu(\boldsymbol{r}_1)}{|\boldsymbol{r}-\boldsymbol{r}_1|} d\boldsymbol{r}_1 \quad (38)$$

where Z_A, is the nuclear charge of atom A centered at $\boldsymbol{R}_A$, ϕ_μ and ϕ_ν are orbital basis functions, and $P_{\mu\nu}$ is the corresponding element of an appropriate density matrix. The first summation is the classical contribution to the electrostatic potential of the atomic nuclei, treated as point charges. The second summation gives the contribution of the electronic charge distribution, which is nontrivial due to the three-center one-electron integrals over basis functions required, see [43] for further details.

To calculate the electric field induced in a structure it's important to remove the fields due to the atoms by using the field-optimized structure in zero applied field. The induced electric field at a given point **r** and applied field $\boldsymbol{E}$ is given by

$$\boldsymbol{E}_{induced}(\boldsymbol{E},\boldsymbol{r}) = \boldsymbol{E}_{total}(\boldsymbol{E},\boldsymbol{r}) - \boldsymbol{E}_{total}(\boldsymbol{E}=0,\boldsymbol{r}) \quad (39)$$

1.6.3 Mulliken charge

Mulliken charges arise from a Mulliken population analysis [44] and provide a means of estimating partial atomic charges from electronic structure calculations. The electron density $\rho(r)$ is expanded in terms of the MOs and is given as:

$$\rho(r) = \sum_{\mu\nu} P_{\mu\nu} S_{\mu\nu} \quad (40)$$

where $P_{\mu\nu}$ is an orbital density matrix and $S_{\mu\nu}$ is an AO overlap matrix. Each atomic center is a positively charged core (charge Z_A) surrounded by a shielding electron cloud, once the electron density each atom has is calculated then atomic partial charge, q_A can be determined.

$$q_A = Z_{\mathrm{A}} - \int \rho_{\mathrm{A}}(r)dr \tag{41}$$

There is a problem however. The charge can be distributed in qualitatively different ways because it's basis set dependent. Also, there is no observable property associated with the "partial charge" and as such there is no reference value to which computed values can be compared, thus there is also no way to evaluate the accuracy.

CHAPTER 2 Field-induced Chemistry and Physics

Sections 2.1-2.2 of this chapter have been published in Surface Science (vol. 643, pp. 164–171, Jan. 2016) in an article with the title "New physics and chemistry in high electrostatic fields" [45].The authors are Markus Karahka and Hans Jürgen Kreuzer. Markus Karahka's contribution to this article consists of 80% of all calculations and drafting 50% of the manuscript. Permission to use this work has been granted by the editor of Surface Science, a copy of the permission letter is attached to this thesis. Section 2.3 is taken from "Atom Probe Tomography and field evaporation of insulators and semiconductors: Theoretical issues" published in Current Opinion in Solid State and Materials Science (vol. 17, pp. 211–216, 2013) [10]. The authors are Elena Silaeva, Markus Karahka, and Hans Jürgen Kreuzer. Markus Karahka's contribution to this work consists of the DFT calculations and drafting 25% of the manuscript. Permission to use this work has been granted by the editor of Current Opinion in Solid State and Materials Science, a copy of the permission letter is attached to this thesis.

To discuss field effects qualitatively, we look, in Figure 2.1 at a molecule AB adsorbed on a metal. Far from the surface and in the absence of a field, the atomic orbitals of A and B hybridize into molecular orbitals, which we take to be a lower-lying bonding orbital, φ_+, and an empty antibonding orbital, φ_-, as discussed in section 1.4. As the molecule approaches a metal surface, additional hybridization with the conduction electrons occur leading to shifts and broadening of these orbitals. For the energetics depicted in Figure 2.1, the antibonding orbital is close to the Fermi level, E_F, of the metal and thus gets partially occupied resulting in (i) bonding to the surface and (ii) weakening of the A-B bond stretch vibration. Applying an electric field, E_z, pointing in the z-direction away from the surface, adds the potential energy, qE_zz, for the electrons outside the metal (assuming, for this simplified discussion, total expulsion of the field from the metal), see the lower part of Figure 2.1. This raises the atomic levels of the atoms A and B by amounts of the order qE_zz_A and qE_zz_B, respectively, with z_A and z_B the positions of atoms A and B above the surface. This results in a substantial re-arrangement of the molecular orbitals. The anti-bonding orbital empties out again leading to restabilization of the

molecule and probably a weakening of the surface bond for the situation depicted in Figure 2.1. If we increase the field strength to the point where the bonding orbital is lifted above the Fermi energy of the metal, it will drain as well, leading to field-induced dissociation. Note that in the absence of the field the bonding orbital of the AB molecule is more B-like i.e. localized on the B atom, whereas the anti-bonding orbital has more A character. As the electric field is increased, these characteristics are changed in a continuous manner into a situation where the bonding orbital is more A-like and the anti-bonding orbital has B character. This possibility of changing the relative position of orbitals of the constituent atoms in a molecule with respect to each other creates a "continuous Periodic Table" and leads to new, field-induced chemistry. A dramatic demonstration of field-induced chemistry was the prediction and discovery that He, which physisorbs on a metal surface with an adsorption energy of about 5 meV becomes covalently bonded in fields of 3 - 4 V/Å with a 50-fold increase of its adsorption energy [46]. Another dramatic example is the electronic transformation of N_2 into CO.

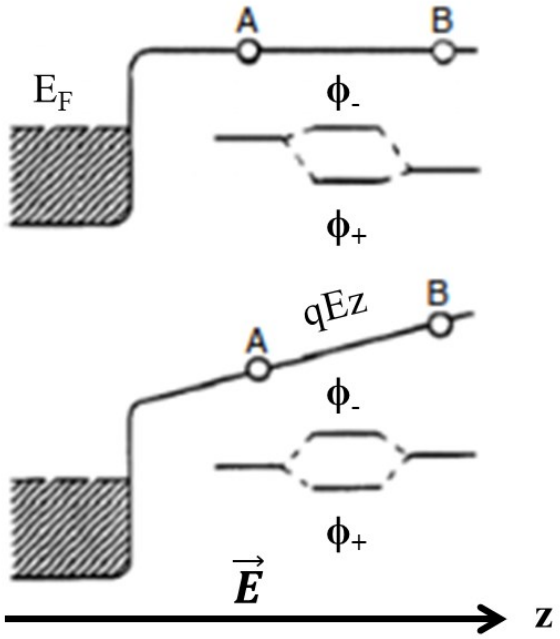

Figure 2.1 Schematic of a molecule AB adsorbed on a metal without and with an electric field ***E*** applied in the *z* direction.

2.1 N_2 and CO

We start with a diatomic, N_2, and show in Figure 2.2 the HOMO density distributions in zero field with the well-understood concentration of the bonding orbital between the two atoms. The LUMO density distributions showed little change with increasing field.

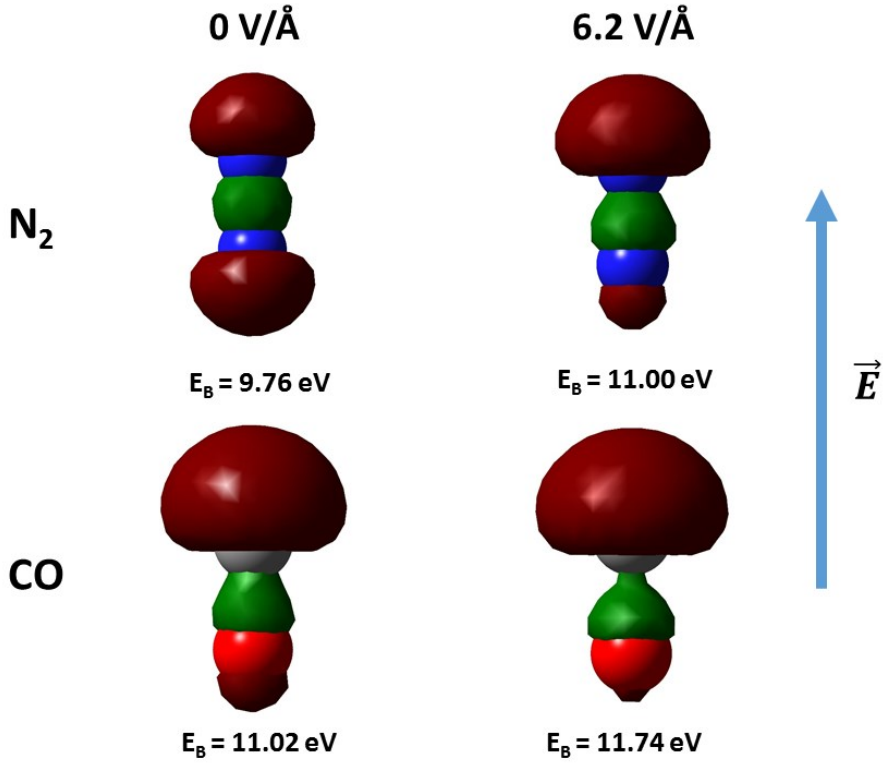

Figure 2.2 Electronic bonding (green) and anti-bonding (burgundy) orbitals for N_2 (N blue) and CO (C grey, O red) in zero field and in 6.2V/Å.

Applying a strong field we see that electrons are transferred in the opposite direction to the field to create a field-induced dipole. In addition, one finds that the electron distribution now resembles very closely that of CO in the absence of a field, i.e. the field has transmuted the upper N atom (in the field direction) to act chemically like a C atom and the other N to become O-like. Indeed, the binding energy of N_2 of 9.7 eV in zero field is increased to 11.00 eV in a field of 6.2 V/Å, i.e. the same as that of CO in zero field. In addition, the vibrational frequency of N_2 is reduced from 7.3×10^{13} Hz in zero field to 6.6×10^{13} Hz in a field of 6.2 V/Å, very close to that of CO in zero field, 6.7×10^{13} Hz. Field dissociation happens at higher fields yet. To quantify this point further we show

in Figure 2.3 an electronic level scheme for N_2 in zero field and in a field of 6.2 V/Å and of CO in zero field demonstrating that the level scheme for N_2 in a field is indeed similar to that of CO in zero field [45].

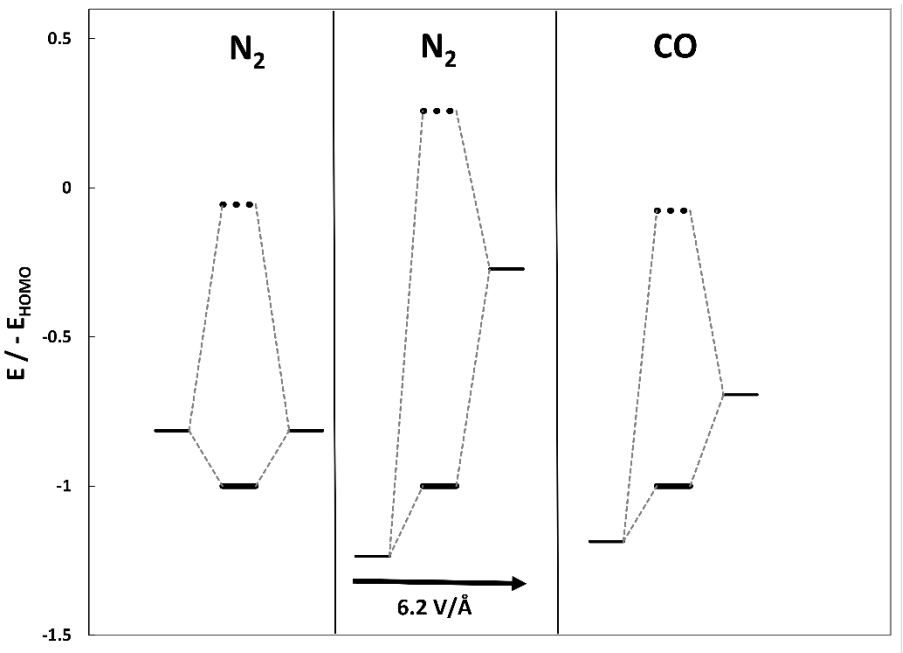

Figure 2.3 Highest occupied levels in the atoms (thin solid line) with resulting HOMO (thick solid line at -1) and LUMO (three dots) levels normalized with the HOMO levels, -11.74 eV for N_2, -7.83 eV for N_2 in a field of 6.2 V/Å, and -10.36 eV for CO.

Thus field-induced chemistry creates a continuous periodic table in the sense that the field alters the chemical characteristics of one element relative to a second one in a continuous fashion [45]. Next we'll show how high electric fields can cause the ionization and dissociation of molecules, using ZnO as an example.

2.2 ZnO

First we'll look at the field ionization of atoms in high fields before we turn to a ZnO molecule. In Figure 2.4 we show the self-consistent electrostatic potential around a Zn atom obtained from density functional calculations. The 4s level, the highest occupied atomic orbital (HOAO), is stable at -6.2 eV raising by only 26meV from -6.212 in zero field to -6.238 eV in a 6.0 V/Å field. Instantaneous ionization will occur when the applied

field depresses the activation barrier below the ionization energy which for Zn happens around 3 V/Å. For lesser fields ionization takes a finite time due to tunneling through the barrier shown on the left side of Figure 2.4.

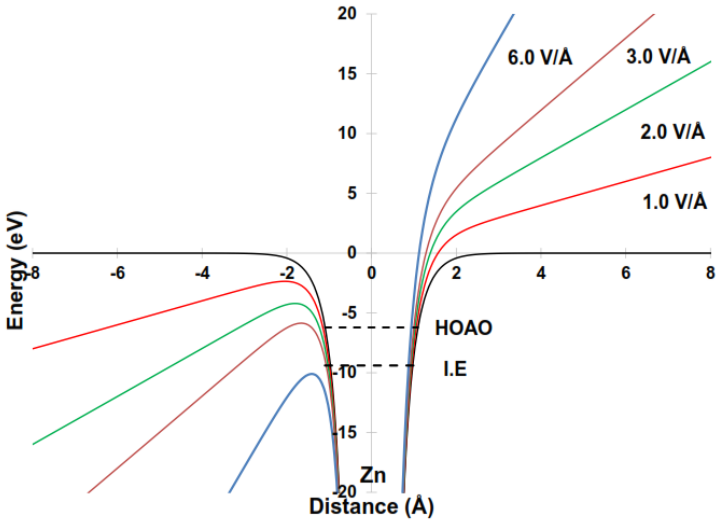

Figure 2.4 Potential seen by the electrons in a Zn atom at various electrostatic fields. Dashed lines indicate the 4s level or highest occupied atomic orbital (HOAO) and 1st ionization energy (I.E.).

As our next topic we look at field ionization and dissociation of a molecule, taking ZnO as an example, and plot in the top panel of Figure 2.5 the potential energy as a function of the bond length obtained by subtracting the electronic energy of Zn and O from that of ZnO. As a small field is applied there remains a potential minimum (red curve) at a bond length close to that in zero field but lowered in energy due to electron transfer from Zn to O creating an additional field-induced polarization. However, at larger distances the potential energy decreases linearly as $-nqEz$ where n is the Mulliken partial charge. This is the potential seen by the Zn^{n+} ion. The potential barrier on the right is gradually lowered with increasing field until it finally disappears at the dissociation field strength. To complete the picture we also show in the bottom panel of Figure 2.5 the potential seen by the electrons (equivalent to the Coulomb potential for the H atom) together with the HOMO level. As the field increases the HOMO level rises until, at the field strength where the potential barrier, on the left, for the atoms disappears, the HOMO will actually be above the tunneling barrier so that an electron moves away from the molecule leaving behind an ion ready to field-dissociate. If at lower fields the tunneling barrier is still

nonzero the probability of ionization will be less than 1, given by the tunneling probability which is lowered in a field of 1 V/Å due to the barrier width, and increased in probability at 4 V/Å with a narrowed and low barrier. Next we discuss field dissociation. In the absence of a field ZnO can be ionized by collisions for instance resulting in a stable ZnO^+ ion. In the highest fields ionization occurs but the potential energy curve no longer has a minimum with the result that a Zn^+ ion is accelerated away by the field with the O atom remaining fixed. We have plotted in Figure 2.5 the Mulliken charge [44] on the Zn for a field of 4 V/Å: it is approximately +1 at a bond separation of 3 Å and then rises gradually to +2. The increasing charge could be taken as indication of post-ionization but care must be taken with all Mulliken charge analyses. These are of course model calculations; however, one could fix the oxygen to a metal surface and impose a field to line the molecular axis up with field direction. Oxide and semiconductor tips prepared for Atom Probe Tomography (APT) are also the relevant systems for this new physics and their issues are discussed in the next section.

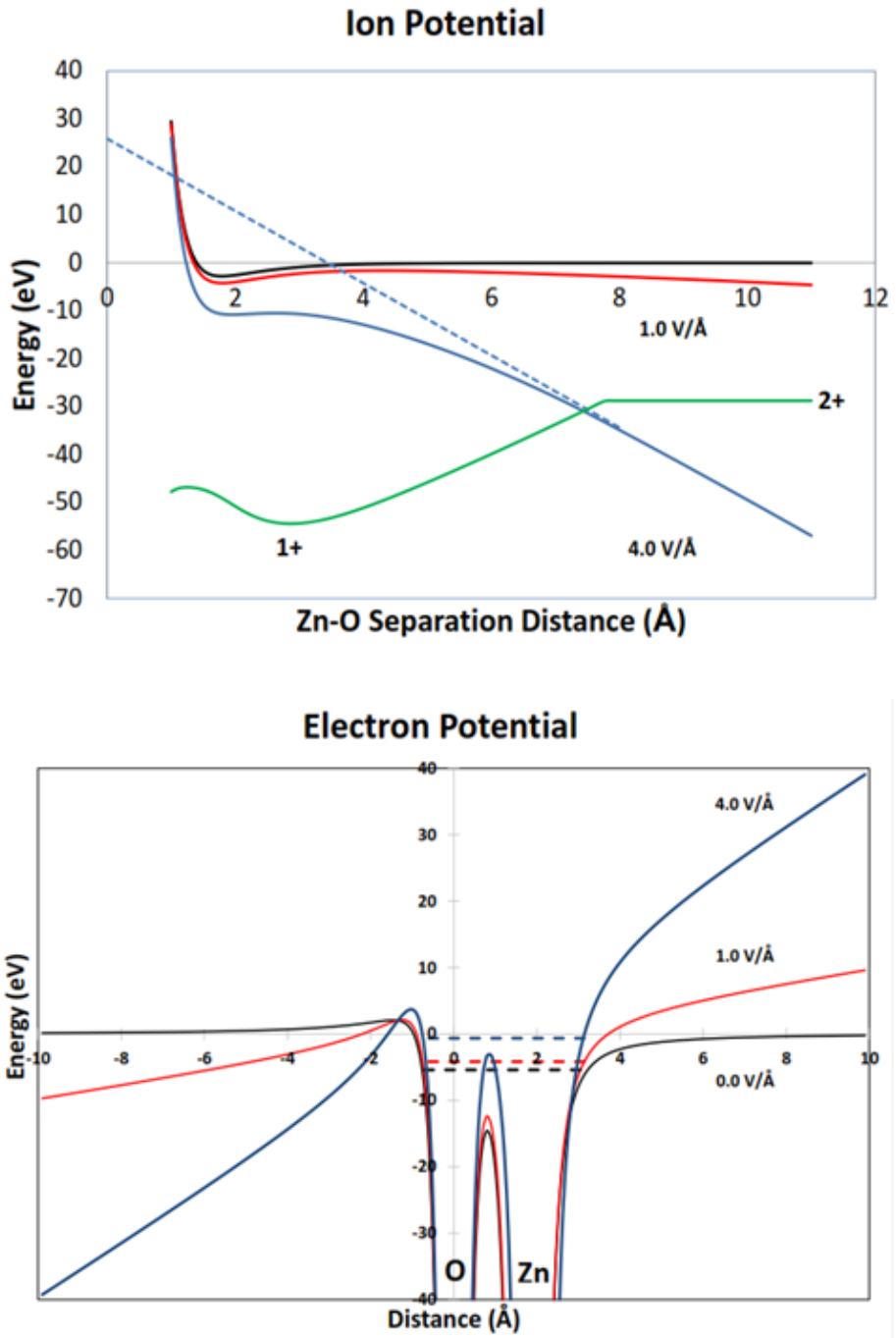

Figure 2.5 Top panel: Potential energy curve of ZnO as a function of bond length for various electrostatic fields. Bottom panel: Electrostatic fields seen by the electrons; dashed line: HOMO's.

2.3 Open problems in APT

The open questions in APT of semiconductors and insulators arise from the fact that high electric fields attack not only the surface atoms of the specimen but many atomic layers deep into the bulk. This changes significantly the electronic structure of the material and complicates the field evaporation process in comparison to the one observed on metals.

One of the current questions is the great difficulty in measuring an accurate stoichiometry of compound semiconductors and oxides [47], [48]. The stoichiometries strongly depend on the electric field and laser power values. Calculations for MgO clusters show several different species from which a direct identification of stoichiometry would be difficult in particular if some of the oxygen migrates down the tip and desorbs as neutral molecules. This problem is discussed in Chapters 3, 4, and 6.

It remains unclear why we can field-evaporate semiconducting and dielectric materials by using photon energies well below their band gap [16], [49]–[51]. For example, MgO with a band-gap of $\varepsilon_{gap} = 7.8$ eV and Al_2O_3 with $\varepsilon_{gap} = 9$ eV were successfully analyzed by using a laser pulse with a photon energy 2.4 eV ($\lambda = 515$ nm) [50], [52]. Even if the photon energy of a laser pulse exceeds the band gap of a semiconductor, such as Si with $\varepsilon_{gap} = 1.12$ eV, the laser efficiency is almost the same for different wavelengths used in the APT from IR to UV. However, the absorption coefficient of Si at UV is known to be five orders of magnitude higher than at IR [53]. At the same time, the laser intensities in APT are well below those needed to cause significant non-linear absorption.

Several phenomena can be invoked for such strange behavior. First, free holes are attracted to the surface by an external field and can additionally absorb laser energy in the same way as electrons do in metals [54]. Also, in the presence of high electric fields the absorption of a semiconductor is increased due to photon-assisted tunneling of electrons from the valence to the conduction band (Franz–Keldysh effect) [55], [56]. In addition, the laser pulse can be absorbed by defects that have much smaller band-gaps between different defect states which might have been introduced unintentionally during specimen

preparation [51], [57]. Finally and more importantly, when the electric field approaches the evaporation field value of the material, its band-gap drastically decreases as we will show throughout this thesis.

Another surprising feature of APT of dielectrics is its very fast evaporation process. It was shown, for example, that the field evaporation of Fe takes place within several nanoseconds after the application of a 500 fs laser pulse. At the same time, the duration of the field evaporation of MgO, FeO and Si was shorter than detector response time (<500 ps) [52], [58]. The thermal conductivities of these materials, however, are similar: 80 W/mK for Fe, 30 W/mK for MgO, 4 W/mK for FeO, and 130 W/mK for Si. This is again an indication that the laser absorption in a dielectric tip is confined to the surface of the tip, where the effect of the external field is the strongest. Thus, heating of the tip takes place in a very small zone that then also leads to a fast cooling process. The recent two-pulse correlation APT experiment on a Si tip has shown that the evaporation process was faster than 10 ps [59]. This observation raises the question whether we can still define a temperature at such a short time scale (short compared to the phonon–phonon and phonon–electron scattering time) and speak about thermally-assisted evaporation. In this case, one should rather consider an ‘‘effective temperature’’ as a measure of the energy density in a phonon bath or even take into account non-equilibrium ballistic phonons and understand their role in the evaporation process [60], [61]. Moreover, lasers not only heat the sample by energy transfer but also generate free charges that can alter the surface electronic structure and, thus, influence the DC field and potential distribution [62], as well as cause electronically-induced atomic bond breaking [63]. Thus, after being absorbed by a semiconductor or dielectric specimen, a laser pulse can influence the field evaporation in APT through thermal as well as electronic processes.

One of the frequently discussed questions is whether the laser pulse can simply ionize a surface atom and, thus, cause its immediate desorption [64], [65]. Positively ionized atoms can be found in many materials, e.g. in n-doped semiconductors the impurities are positively charged; in ionic crystals like MgO the magnesium atoms are always positively charged. However, these structures are shown to be stable until a sufficiently high field is

applied to them. It means that it is not enough just to ionize an atom in order to evaporate it.

Thus, many experimental observations indicate that laser absorption is confined to the surface of dielectric tips. This is not excluding the possibility of the laser absorption in the bulk of the specimen which can lead to delayed evaporation, unfortunately decreasing the APT mass resolution [52], [66], [67], and causing non-hemispherical tip formation, which in turn leads to artefacts in the reconstructed images [68]. To account for such effects, one has to consider the interaction of a laser pulse with a nanometric tip and calculate the absorption patterns and then temperature evolution inside the tip in three dimensions as it has been done for metallic tips [69] but also taking into account the diffusion and recombination of laser-generated carriers.

In conclusion we want to stress again that the experimental confirmation of the theoretically predicted closure of the band gap in high electrostatic fields will, in our opinion, advance our understanding of APT significantly. Theoretical closure is discussed in Chapters 3 and 4 with experimental confirmation of band gap closure shown in Chapter 5.

CHAPTER 3 Field Evaporation of MgO: a Theoretical Study

The majority of this chapter has been published in Ultramicroscopy (vol. 132, pp. 54–59, Sep. 2013) as an article with the title "Field evaporation of oxides: a theoretical study" [70]. The authors are Markus Karahka and Hans Jürgen Kreuzer. Markus Karahka's contribution to this work consists of all calculations and drafting 50% of the manuscript. Permission to use this work has been granted by the editor of Ultramicroscopy, a copy of the permission letter is attached to this thesis. Also included are parts from "Atom Probe Tomography and field evaporation of insulators and semiconductors: Theoretical issues" published in Current Opinion in Solid State and Materials Science (vol. 17, pp. 211–216, 2013) [10]. The authors are Elena Silaeva, Markus Karahka, and Hans Jürgen Kreuzer. Markus Karahka's contribution to this work consists of the DFT calculations and drafting 25% of the manuscript. Permission to use this work has been granted by the editor of Current Opinion in Solid State and Materials Science, a copy of the permission letter is attached to this thesis.

Abstract

To understand Atom Probe results on the field evaporation of oxides we use density functional theory on MgO clusters to follow the structural changes during field evaporation and to obtain potential energy curves, partial charges and desorption pathways. It is straightforward to understand that Mg evaporates doubly charged. We also show that MgO^+, $MgO_2{}^+$ and O^+ ions leave the surface.Two questions are however new for oxides. (1) Where do the electrons go? When the oxides are deposited on a metal tip it can be assumed that the electrons are used to complete the electrical circuit. However, this leaves the second question unanswered, namely (2) what happens to the oxygen? We will argue that there are two channels for the oxygen, namely: (a) to travel down the (metallic) surface of the tip and eventually to desorb either as atoms or molecules (b) The oxygen can recombine within the oxide layer itself and desorb as a neutral molecule accelerated in the inhomogeneous field due to its induced dipole.

3.1 Introduction

The atom probe, developed by Müller et al. in 1968 [7], allows for the identification of the atomic composition of micro- and nano-specimens, see section 1.2 for a description of atom probe tomography. Although originally developed for metallic tips and used extensively for the study of the atomic composition of steels and other alloys it has also been adapted for the study of semiconductors and more recently for insulators through the assistance of ultrafast laser pulses. Before laser assisted APT, anaylsis of oxides was restricted to small geometries such as thin tunnel barrier layers of Al_2O_3 up to 2.5 nm thick [71] and 2 nm thick MgO layers in magnetic tunnel junctions [72]. Now with laser assisted APT the analysis of much thicker oxide layers is possible such as 15 nm thick NiO [73], [74], 50 nm thick WO_3 [73], 4 and 32 nm thick MgO [52], and bulk MgO and ZnO [75]. The analysis of bulk insulating ceramics such as zirconia/spinel nanocomposites has also proven successful [76].

A quantum-mechanical theory was developed in the 1980's and 90's for field desorption of atoms and molecules on metal tips and also for the understanding of field-induced chemistry [1]–[4], see Chapter 2. When we proceed to insulators or semiconductors the situation is of course more complicated as the field itself inside the material gets locally reduced to various degrees. That is why self-consistent calculations at the quantum mechanical level are needed as we will demonstrate in this and further chapters. A similar first principles approach is largely lacking for semiconductors, and for oxides and other insulators, key materials in micro-electronics. As the authors of a recent laser assisted APT study of MgO state [52]: "Although APT has provided a large number of results on a wide panel of materials, interpretation of 3-D images are sometimes difficult due to a lack in the understanding of the different evaporation mechanisms involved in semiconductors and oxides". It is the objective of this thesis to develop the lacking theoretical framework.

Field evaporation of insulators and oxides in particular, needs additional considerations. To establish the large fields necessary for field evaporation one needs a metallic field emitter tip. On this, layers of oxide or any other insulator are formed using various methods which produce layers thick enough to establish proper crystal structure and to allow sufficient ion yields. As a result the electric field penetrates the insulating layer and is further enhanced by its dielectric constant. What is observed in the laser assisted APT of MgO are mostly Mg^{2+} ions [52], [75], and more recently also MgO_2^+, MgO^{2+}, MgO^+, Mg^+, O_2^+, and O^+ [75], [77]. Our *ab initio* cluster calculations will reproduce these findings, give explanations, and also answer questions like what happens to the oxygen? We will establish several pathways to remove oxygen: (a) O^- can migrate down the metallic shaft of the field emitter tip and eventually desorb as a molecule. (b) Oxygen can recombine on top of the oxide layer and desorb as a neutral species or even as O_2^+. An excellent theoretical treatment of the laser assisted field evaporation of bulk MgO was done by Tsukada et al [78]. They investigated the effects of holes on the sublimation energy of corner ions and potential energy surfaces of corner Mg ions without a field and in a field of 0.514 V/Å. The result was that holes reduce the sublimation energy and activation barrier for desorption. However they did not look at the various ionic species produced during the field evaporation of MgO as we have done in our calculations.

As for the computational approach to field-induced chemistry it should be noted that relative changes in molecular energy levels are of the order of eV, so that field effects can be adequately described by the simplest methods such as the tight binding approach as has been shown in comparisons with density functional theory [24], [79], [80]. Nevertheless, because of the ready availability nowadays of sophisticated software packages we will base our calculations on density functional theory as implemented in the GAUSSIAN'09 software package [40], see section 1.6 for computational details. The underlying metallic tip enters the calculations as the source of a constant electric field across the cluster. The use of a cluster model in a (homogeneous) electric field has several advantages: (1) The internal field is automatically generated. (2) The crystal structure of the cluster adjusts to the electric field. (3) Edge effects can be studied. (4)

Negative ion loss in the downward field can be avoided by fixing the bottom plane of atoms in the cluster.

The chapter is structured as follows: In the next section we start with a single MgO molecule in a field to establish the minimal wave function set needed for reliable results. Next we look at various cluster sizes from 3 × 3 × 3 to 4 × 4 × 4 to see how cluster size influences field disintegration of these clusters. At the end of the chapter we will summarize our findings and add some speculative ideas.

3.2 Results

3.2.1 Preliminary: MgO Molecule in a Field

As a preliminary exercise we study the effect of a large electric field on the structure and energetics of a MgO molecule, also with the aim to establish the minimum wave function basis set such that adding more wave functions does not alter the results by much. After many trials we found that the set B3LYP/6-311+G* is sufficient.

For MgO in a field we fix the position of the oxygen to avoid that the molecule as a whole drifts down the field. In Figure 3.1 we show the potential energy curves $V(d) = -[E_{el}(\mathrm{MgO},d) - E_{el}(\mathrm{Mg}) - E_{el}(\mathrm{O})]$. Here $E_{el}(\mathrm{MgO},d)$ is the total electronic energy of the molecule with its constituent atoms separated by a distance d, and $E_{el}(\mathrm{Mg})$and $E_{el}(\mathrm{O})$ are the respective energies of the isolated atoms. In the absence of a field we find a bond length $b_0 = 1.9 \pm 0.09$Å, a vibrational frequency $\nu = 1.8 \times 10^{13}\mathrm{s}^{-1}$, and a bond dissociation energy $E_{diss} = 2.52$ eV in reasonable agreement with the experimental bond length of $b_0 = 1.749$ Å [81] and a theoretical value of $E_{diss} = 2.65 \pm 0.16$ eV [82].

In a field, $E > 0$, the adiabatic potential energy curve goes through a maximum at which the Mg is sufficiently charged to get accelerated away from the oxygen. The energy difference between the Schottky hump and the potential minimum is the activation

energy for dissociation. It enters the rate constant of dissociation which in a simplified Arrhenius parametrization reads $r_{diss} = \nu \exp[-E_{diss} / k_B T]$. Thus to keep the molecule intact for one minute after applying a field at room temperature we need $E_{diss} > 0.1$ eV. This is reached at a field of the order of 1 V/A, i.e. at considerably lower fields than the field strength of spontaneous disintegration, $E = 2$ V/Å.

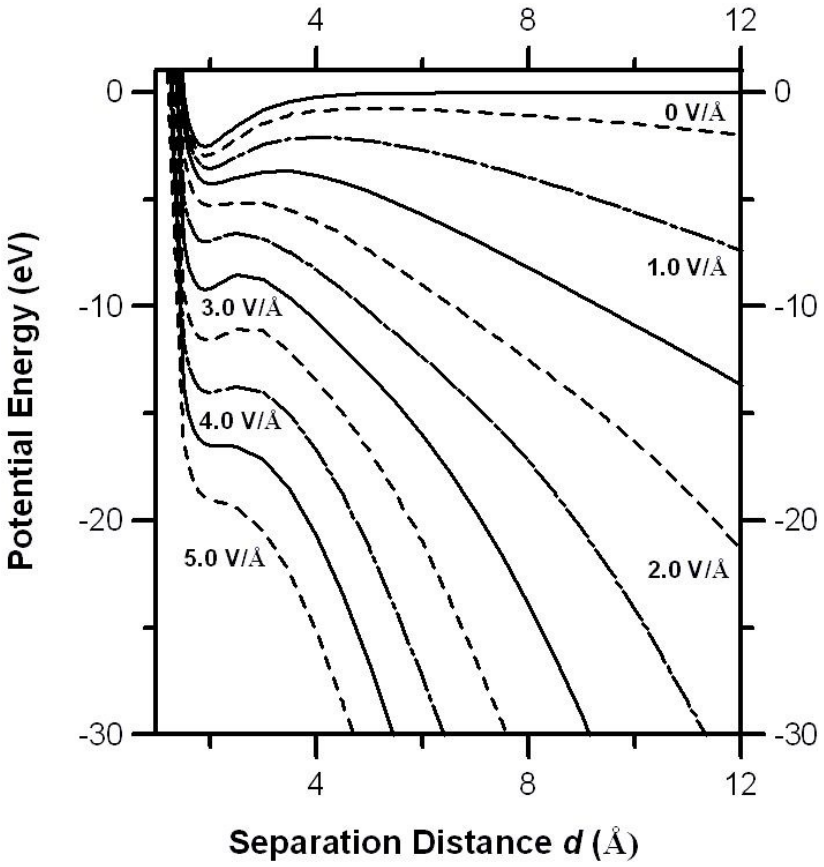

Figure 3.1 Potential energy curves of MgO molecule in a field. The top curve is at 0 V/Å with the field strength increasing in 0.5 V/Å steps for each lower curve.

An unexpected feature of the field dependence is the fact that for fields larger than 2 V/Å a Schottky hump develops again to disappear at a much higher field of 4.5 V/Å. This could be reached by increasing the field rapidly so that dissociation does not happen at 2 V/Å. To shed some light onto this phenomenon we have plotted in Fig 3.2 the HOMO-LUMO gap which shows a marked minimum around 2 V/Å to rise again after that. Curiously the bond length changes by less than 0.1 Å over the full field range whereas the partial (Mulliken) charge increases from 0.4 e to 1.0 e. Also plotted, in the central panel, is the dissociation barrier for completeness.

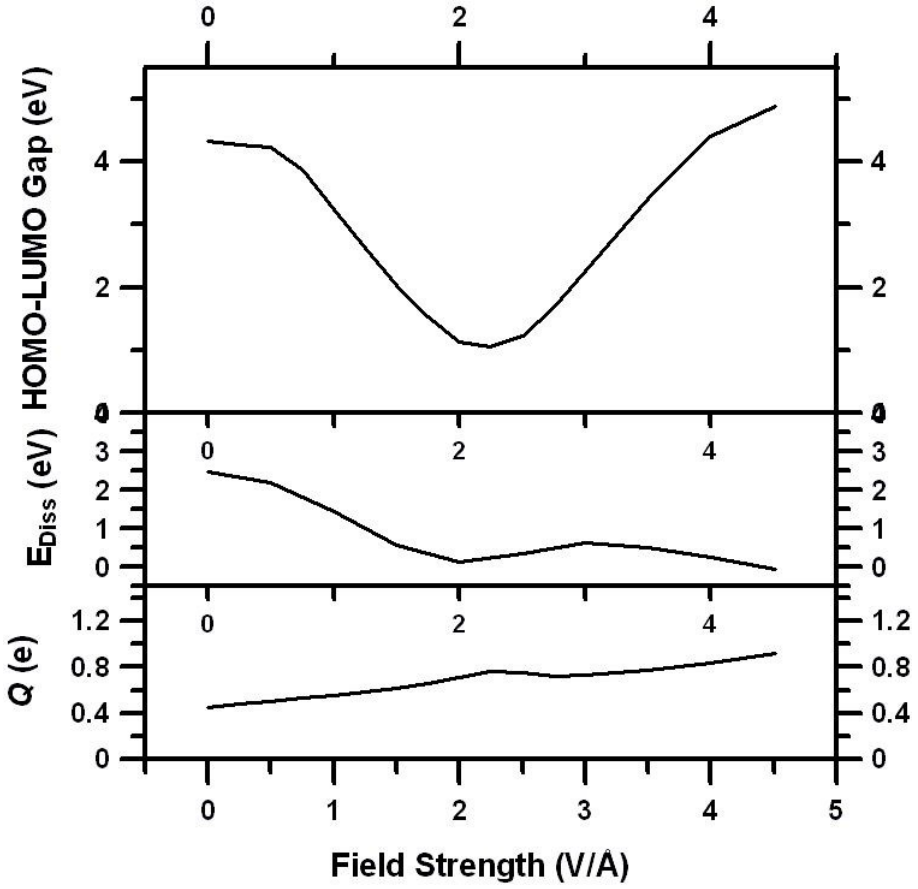

Figure 3.2 MgO molecule in a field displaying the HOMO-LUMO gap, the energy barrier for field dissociation, and the Mulliken charge.

3.2.2 MgO Clusters

On our quest to understand field evaporation of solid MgO we start with a small cluster of 3 × 3 × 3 atoms in zero field obtaining the proper crystal structure with a bond length of 1.9 Å. Keeping the lowest layer of the cluster fixed we apply a field and find that up to a field of about 2 V/Å little happens to the cluster apart from a small upward move of the Mg atoms. Things change drastically beyond 2.5 V/Å when a Mg has been removed as Mg^{2+} and the top two layers "melt" without reaching a stable equilibrium except when only the lowest fixed layer remains. Typical snapshots during the iterative procedure are shown at 2.5 V/Å in Figure 3.3. The first picture in the top row is the starting configuration at field zero with the second image showing the upward buckling of the Mg

atoms in the top layer. A few iterations later, image three, the first Mg leaves the cluster as Mg^{2+}. This is followed in the last image of the top row with a situation where the top layer has more or less disintegrated leading to the evaporation of a second Mg^{2+} in the first image of the bottom row, and further re-arrangements in the following two pictures. It is crucial to note that the negative charge left on the cluster after the Mg^{2+} evaporations resides in the centre of the leftover cluster, and no oxygen has left the cluster at this stage. Of course in the APT experiment an MgO layer is deposited on a metal tip. This allows the negative charge to flow into the tip. In addition, negative O^- can also migrate down the metal shaft. To see what happens if the leftover negative charges were removed from the cluster we do this manually and take the last (now neutral) structure in the top row of Figure 3.3 as the starting point for further iterations, see Figure 3.4.

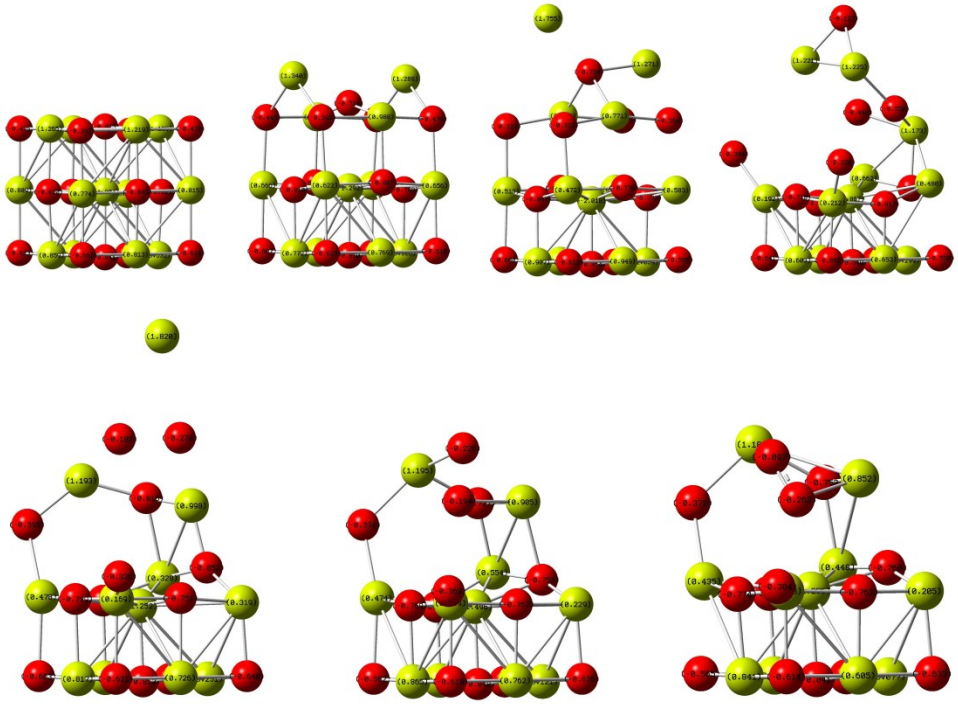

Figure 3.3 3 × 3 × 3 cluster of MgO in a field of 2.5 V/Å. Shown are snapshots during the DFT iterations leading to the evaporation of Mg^{2+} and melting of the top row. The O atoms are red and the Mg are yellow-green.

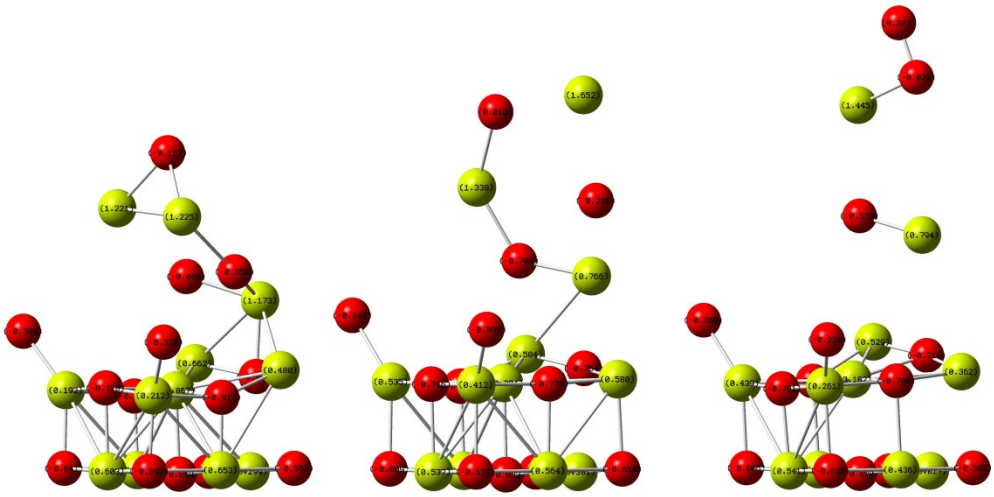

Figure 3.4 Further iterations beginnning with the last structure in the top row of Figure 3.3 with two electrons removed to make it neutral. The O atoms are red and the Mg are yellow-green.

After several iterations another Mg^{+2} ion is removed and the stretched structure left over breaks up further with singly charged MgO_2^+ and MgO^+ leaving.

Next we look at the same cluster but this time tilted so that an apex shows in the field direction to mimic a protrusion or an edge showing again evaporation events while iterations proceed, this time in a field of 3 V/Å, see Figure 3.5. Similarly to the cluster in the top row of Figure 3.3 we see in the top row of Figure 3.5 the upward buckling of the center Mg atom and its evaporation as Mg^{2+}. After that, new phenomena appear. In the iteration represented by the first image in the second row we note an O atom moving up as a positively charged ion. Another effect takes place after that, namely that an O atom moves downward on the side of the cluster to begin its journey down the shaft.

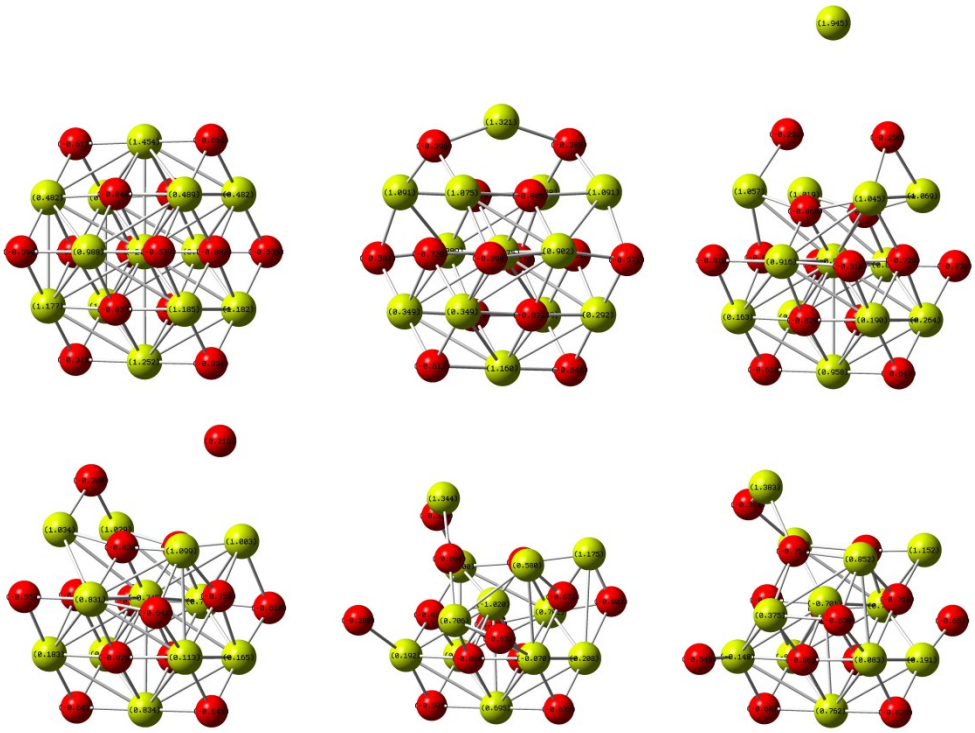

Figure 3.5 3 × 3 × 3 cluster of MgO tilted into a field of 3 V/Å. Shown are snapshots during the DFT iterations leading to the evaporation of Mg^{2+} and melting of the top row. In addition to the evaporation of Mg^{2+} also O^{+} evaporates at a later stage, and a O^{-} migrates down the cluster. The O atoms are red and the Mg are yellow-green.

Lastly, we look at a larger cluster of four 3 × 3 layers in a field of 4 V/Å, see Figure 3.6. Buckling of Mg in the top layer is again the initiation of field evaporation. Soon two corner Mg atoms get loose and evaporate as Mg^{2+}. Shortly thereafter, a positively charged O^{+} moves towards the detector. In addition, a negatively charged Mg^{-} migrates down the cluster. Unfortunately, the size of this cluster prevented further iterations in a reasonable time. Similarly, one should examine the effects of charging and de-charging the cluster.

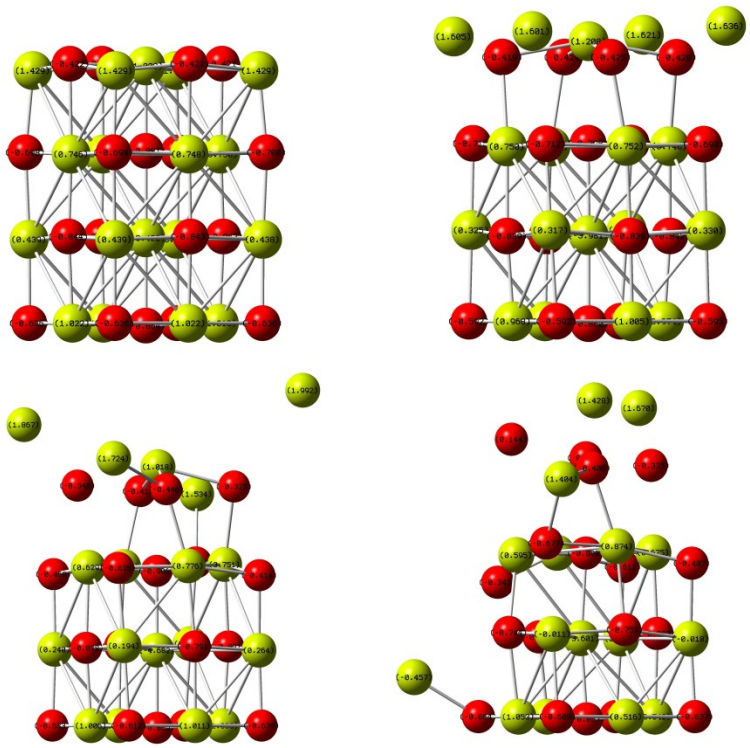

Figure 3.6 4 × 3 × 3 cluster of MgO in a field of 4 V/Å. Shown are snapshots during the DFT iterations leading to the evaporation of Mg^{2+} and melting of the top row. The O atoms are red and the Mg are yellow-green.

3.2.3 Local fields and HOMO-LUMO gaps

Density functional theory has also been used to calculate the field distribution inside a dielectric cluster. As an example we considered a small MgO cluster of 3 x 3 x 3 atoms. The left layer of the cluster was fixed to prevent its drifting in the field as a homogeneous external field was applied to it. Figure 3.7 shows the electric field profile along the central atomic chain inside the cluster through an O atom in the left layer, a Mg atom in the middle and O atom again in the right layer. One can see that the field is enhanced above the first O atom by a factor similar to that as above a metallic adatom. It is interesting to note that at a higher external field the MgO cluster is rearranged in such a way that the enhancement factor is higher (1.5 at E = 0.5 V/Å and 1.8 at E = 1 V/Å) and the average field in the middle of the cluster is lower. At a field of 0.5 V/Å the average internal field (between -2 and 2 Å) corresponds approximately to the external field divided by the dielectric constant of MgO (ϵ_r = 10). At a field of 1 V/Å the internal field is decreased by

a factor of 100, demonstrating that in such high electric fields the dielectric behavior departs from that predicted by classical electrostatics. This strong screening of the external electric field by the bound charges can also explain the absence of the large potential drop at the atom-probe tip apex, mentioned in section 1.2.

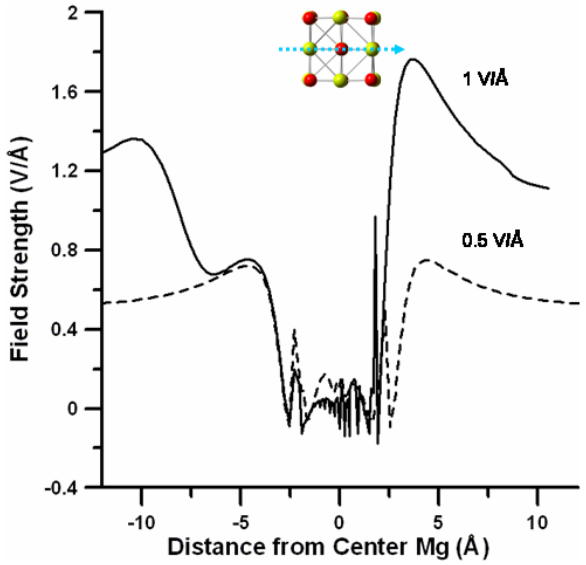

Figure 3.7 Electrostatic field distribution in and around a MgO cluster.

One question remains as to whether or not field-induced metallization is a surface phenomenon or affects the entire bulk. Figure 3.8 shows the induced electric field through a 3x3x3, 4x4x4, 2x2x6, and 2x2x10 MgO cluster in an applied field of 1.0 V/Å. The field is calculated along a hollow site i.e. between the atoms in the cluster and not through any atoms. The average internal induced field was found to be reduced by approximately 2, 26, 9, and 44 for the 4x4x4, 3x3x3, 2x2x10, and 2x2x6, respectively. The 4x4x4 has two layers between the hollow site and the outside whereas the others only have one. We see that the field reduction increases as the cluster gets smaller or as the layers decrease. While a more exhaustive analysis across different sites, cluster thicknesses, and field strengths needs to be performed, we can take this as an indication that field-induced metallization is a surface phenomen restricted to the first few monolayers.

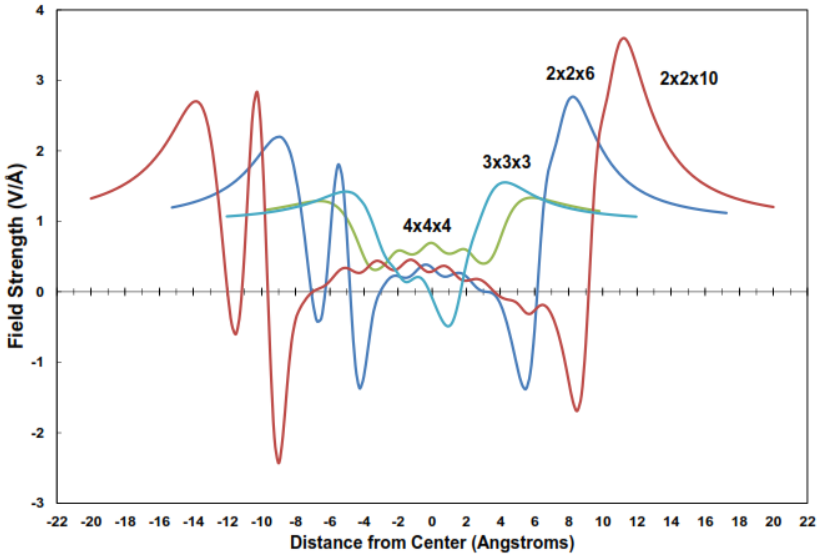

Figure 3.8 The induced electric field through a hollow site of a MgO cluster in an applied field of 1.0 V/Å.

In Figure 3.9 we plot the HOMO–LUMO or band gap, for Si_6 and also for MgO 3x3x3 cluster, as a function of field strength. It decreases steadily and drops to zero at the predicted evaporation field strength as an indication that in such fields Si and MgO, and, by implication, all semiconductors and insulators, become conducting. This effect was first observed some years ago that the disintegration of polymers such as poly-thiophene in high fields was also accompanied by the closing of the HOMO–LUMO gap, i.e. the molecule disintegrated while it became conducting [83]. This, in our opinion has far-reaching implications to understand APT of insulators and semiconductors as we will discuss in the next two chapters.

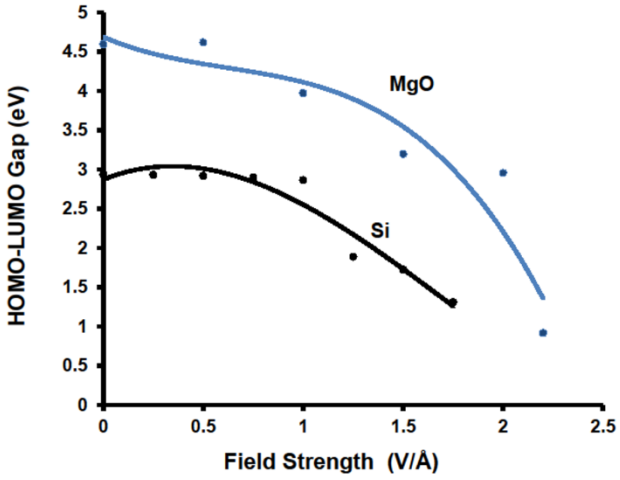

Figure 3.9 HOMO–LUMO gap for Si and MgO clusters.

For MgO, 14 systems of varying size and basis set have been calculated and are shown in Figure 3.10, note the number in brackets indicates multiplicity.

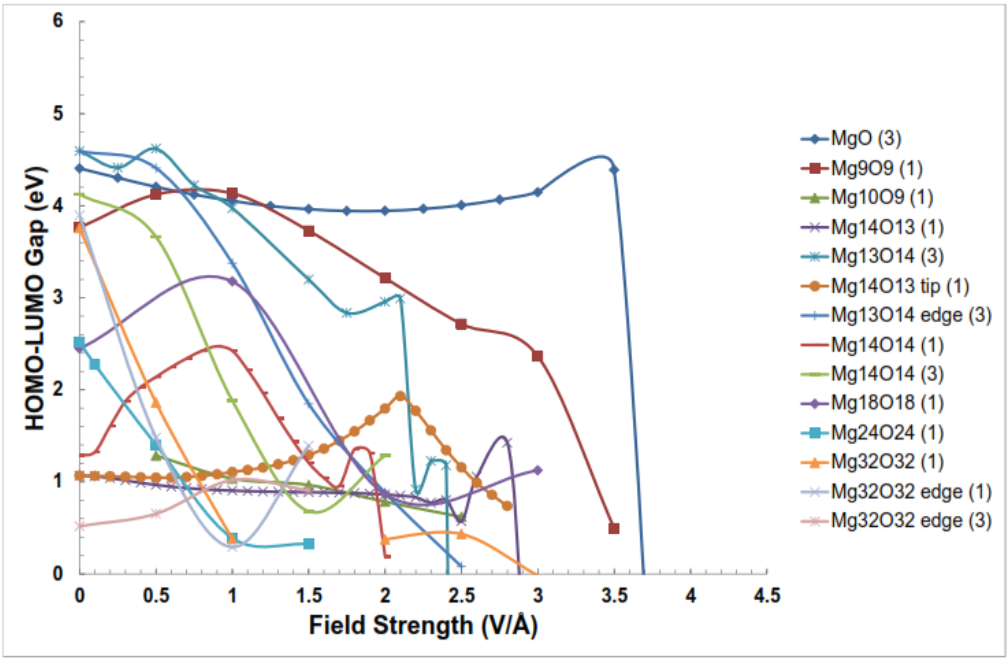

Figure 3.10 HOMO-LUMO gaps vs. electric field strength for different size MgO clusters. The numbers in brackets indicate the multiplicity.

The HOMO-LUMO gaps can increase or decrease due to structural changes caused by the electric field. Instead of following the ups and downs, so to speak, of the gaps, we focus on the effects of cluster size on the gap at zero field and the critical evaporation field strength. Figure 3.11 shows the HOMO-LUMO gap at zero field vs. the number of atoms *n*. For the singlet systems (3-21G, 3-21G*, and 6-31G*) the HOMO-LUMO gap increases in general with the number of atoms. Interestingly enough for the triplet systems the opposite is true. Most likely this is due to the fact that the HOMO-LUMO gap for anything other than a singlet isn't well defined. For a triplet system there are 4 possible gaps one could look at: α-α, β-β, α-β, and β-α. The α-α gap was chosen here because when one changes the wavefunctions from unrestricted to restricted for the MOs, it is the α-α gap that is left. None of the systems have a HOMO-LUMO gap equal to the bulk MgO bandgap of 7.8 eV but that isn't surprising. It has been found that 3 nm MgO nanocubes absorb light at 5.6 eV and 4.6 eV [84]. A 3 nm cube would be about 15 atoms across where as the largest cluster calculated here is 4 atoms across. More clusters should be calculated to see when the HOMO-LUMO gap approaches that of the bulk and nanocubes. All that being said, a 3x3x3 ($Mg_{13}O_{14}$) triplet system does have a HOMO-LUMO gap of 4.6 eV, see Figure 3.9. As for closure we see that approximately half of the gaps close completely (MgO, $Mg_{14}O_{13}$, $Mg_{13}O_{14}$, and $Mg_{32}O_{32}$) with most of the rest decreasing to less than 0.5 eV at evaporation. It is quite possible they would close as well if the optimizations were run further. Due to time constraints this was not done.

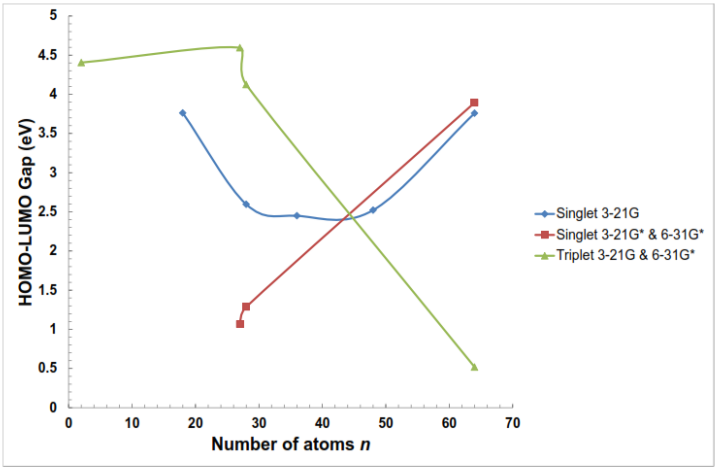

Figure 3.11 HOMO-LUMO gap at zero field vs. number of atoms in a MgO system.

Looking at the critical evaporation field strength, E_{ev}, we find that for systems of low coordination, such as with one Mg atom adsorbed on the face of a cube, the strength is 1.5 V/Å < E_{ev} ≤ 2.0 V/Å ($Mg_{14}O_{14}$). The evaporation field strength for a MgO molecule and the $Mg_{10}O_9$ cluster are 3.5 V/Å < E_{ev} ≤ 4.0 V/Å and 2.5 V/Å < E_{ev} ≤ 3.0 V/Å, respectively. The reason for this is due to charge separation. In Gaussian all charges (including electrons) must be based on atoms, thus when an electron comes off a Mg atom in a MgO molecule it goes onto the O atom and stays there regardless of field strength. There is now an ionic attraction working against the applied field. As we increase the layers or charge separation distance, the ionic attraction gets weaker causing the evaporation field strength for a singly bonded Mg atom to decrease from > 3.5 V/Å to > 1.5 V/Å as we go from a single molecule to a 3x3x3 cube.

The evaporation field strength for higher coordination atoms such as on the edge, atomic terraces, or corners are 2.5 V/Å < E_{ev} ≤ 3.0 V/Å for a 4x4x4 ($Mg_{32}O_{32}$) cluster, 2.6 V/Å < E_{ev} ≤ 2.8 V/Å for a 3x3x3 ($Mg_{14}O_{13}$), 2.4 V/Å < E_{ev} ≤ 2.5 V/Å for a 3x3x3 ($Mg_{13}O_{14}$), and 3.0 V/Å < E_{ev} ≤ 3.5 V/Å for 2 layers of 3x3 or 3x3x2 (Mg_9O_9). So we see that the evaporation field strength for an atom will depend on coordination i.e. geometry (as will be discussed in Chapters 4 and 6) and the local charge distribution i.e. charge screening.

3.3 Discussion and Outlook

The crucial difference in field evaporation of metals and insulators is the basic fact that metals expel electrostatic fields and insulators allow them full penetration, with semiconductors somewhat in between. This has a direct consequence for the operation of the Atom Probe. (a) Metals: the fields penetrate less than the first atomic surface layer and are enhanced by up to a factor of three at protrusions, corners and edges. Thus atoms at these exposed sites are removed first, exposing atoms in the layer below and thus achieving layer-by-layer compositional analysis in Atom Probe Tomography of metals and alloys. (b) Insulators: electrostatic fields penetrate insulators whether they are isolated species or grown on a metal substrate. The immediate consequence is that the field attacks the complete crystal simultaneously with perhaps some more action on the surfaces with fewer bonds and mobility out of the surface. However, if large fields are used the whole crystal structure will change much akin to melting so that site specificity could be lost. We have demonstrated in this chapter that the HOMO-LUMO gap closes with two consequences: if it goes to zero the tip becomes metallic. This is beneficial for at least two reasons: (i) charge accumulation inside the cluster is avoided, and (ii) the field is actually expelled, at least partially, from the cluster. Both effects will aid APT. If the gap does not close completely we still get a narrow gap semiconductor instead of an insulator with the effects just discussed for a metallic tip at least partially invoked. The fact that APT can be applied to non-metallic systems is perhaps clear evidence of the field screening. The field penetration may be very limited even in dielectrics. Of course, using laser irradiation either resonantly or thermally, will aid the evaporation process as well and is possibly the reason why fields used in the experiment are smaller than the ones used in our calculations.

Our cluster calculations also suggest that in addition to Mg^{2+} one should also see MgO^{+}, MgO^{2+}, MgO_2^{+}, and O^{+} ions in the mass spectrometer in fields of more than 2 V/Å. These ions have recently been observed in APT mass spectra by Chen et al. [75] and Larson et al. [77]. In this paper we have only addressed static questions but did not address the kinetics of field evaporation. This can be done using the framework worked

out 20 years ago for field evaporation of metals provided one has the right computational equipment [21], [30].

CHAPTER 4 Field evaporation of ZnO: theoretical insights

This chapter has been published in Ultramicroscopy (vol. 159, pp. 156–161, Dec. 2015) as an article with the title "Field evaporation of insulators and semiconductors: theoretical insights for ZnO"[85]. The authors are Markus Karahka and Hans Jürgen Kreuzer. Markus Karahka's contribution to this work consists of all calculations and drafting 50% of the manuscript. Permission to use this work has been granted by the editor of Ultramicroscopy, a copy of the permission letter is attached to this thesis.
Section 4.4 of this chapter has been adapted from an article published in the Journal of Applied Physics (vol. 118, pp. 025901–7, July 2015) with the title "Field evaporation of ZnO: a first-principles study [86]. The authors are Yu Xia, Markus Karahka and Hans Jürgen Kreuzer. Markus Karahka's contribution to this work consists of assistance with the calculations and drafting 25% of the manuscript. Permission to use this work has been granted by the editor of Journal of Applied Physics, a copy of the permission letter is attached to this thesis.

Abstract

We look at the new challenges associated with Atom Probe Tomography of insulators and semiconductors with regard to local fields inside and on the surface of such materials. The theoretical discovery that in high fields the band gap in these materials is drastically reduced to the point where at the evaporation field strength it vanishes will be crucial in our discussion. To understand Atom Probe results on the field evaporation of insulators and semiconductors we use density functional theory on ZnO clusters to follow the structural and electronic changes during field evaporation and to obtain potential energy curves, HOMO-LUMO gaps, field distributions, desorption pathways and fragments, dielectric constants, and polarizabilities. Our results also help to explain problems related to stoichiometry in the mass spectra measured in atom probe tomography. We also examine the effects of electric field reversal on the evaporation of ZnO and compare the results with Si.

4.1 Introduction

Field evaporation of insulators, and oxides in particular, needs certain considerations as discussed in section 1.2 on APT and 3.1 on APT of MgO. To establish the large fields necessary for field evaporation one needs a metallic field emitter tip. On this, layers of oxide or any other insulator are formed using various methods of oxidation. As a result the electric field penetrates the insulating layer and is further modified by its dielectric constant. What is observed in the laser assisted APT of ZnO are mostly Zn^{2+} ,Zn^{+}, $O_2{}^{+}$ ions with other combinations such as Zn_2O^{2+} present to a lesser degree [49], [75], [87]. However, there is an overlap of $O_2{}^{+}$ and Zn^{2+} in the mass spectra making it difficult to determine which is the dominant ion. Our ab initio cluster calculations will reproduce these findings, give explanations, and also answer questions such as what happens to the evaporation process if the field direction is reversed and whether the predominant ion seen in the mass spectra of ZnO is $O_2{}^{+}$ or Zn^{2+}?

The chapter is structured as follows: In section 4.2 we start with a single ZnO molecule in a field to establish that we have the correct level of theory for the ZnO clusters. Next in section 4.3 we look at pyramidal clusters, $Zn_{10}O_7$ and Zn_9O_7, to see how cluster size and applied field direction influences field disintegration of these clusters and compare our results with an Si_{18} conical tip. Then we investigate a "large" $Zn_{26}O_{26}$ cluster under high electric field conditions in section 4.4. A criteria for the size of the smallest cluster is that a unit cell should be fully enclosed by another layer with the proper structure and stoichiometry, the volume is very critical especially if a large concentration of holes is needed on the surface to screen the fields. By using such a cluster we are able to look at the local field distribution inside the cluster and the stoichiometry of the evaporated ion species. We will show evidence for field-induced metallization of the cluster at the evaporation field strength i.e. expulsion of the electrostatic fields, divergence of polarizability and dielectric constant, and closure of the HOMO-LUMO gap. Lastly we will summarize our findings and add some ideas concerning missing oxygen in APT.

4.2 ZnO molecule

We study the effect of a large electric field on the structure and energetics of a ZnO molecule with the aim to establish the correct level of theory such that the molecule is well characterized and therefore the clusters are as well. The computational method as outlined in Chapter 3.1-3.2.1 is used and the basis set B3LYP/6-311G*.

We investigate the electronic structure of the ZnO molecule by looking at the singlet (double bond) and triplet (single bond) cases. For ZnO in a field we fix the position of the oxygen to avoid that the molecule as a whole drifts down the field. In Figure 4.1 we show the potential energy curves $V(d) = - [E_{el}(ZnO,d) - E_{el}(Zn) - E_{el}(O)]$ of the singlet(triplet) in panel a(b). Here $E_{el}(ZnO,d)$ is the total electronic energy of the molecule with its constituent atoms separated by a distance d, and $E_{el}(Zn)$ and $E_{el}(O)$ are the respective energies of the isolated atoms. In the absence of a field we find a bond length d_0=1.8 Å (2.0 Å) ± 0.09 Å and a dissociation energy E_{diss} = 2.8 eV (0.65 eV) for the singlet (triplet) case. The bond lengths are in reasonable agreement with experimental values of d_0=1.95 Å for ZnO wurtzite, and the singlet dissociation energy is within the experimental value of E_{diss} = 2.8 ± 0.2 eV [88]. The calculated E_{diss} of 0.65 eV for the triplet is much lower than the value reported above by Wicke et al [88] but in theoretical agreement with E_{diss} =0.66 eV calculated by Dolg et al [89]. We define the evaporation field E_{ev} as the field strength at which the molecular structure is unstable and an ion moves down the field. For the singlet E_{ev} =4.7 V/Å and the molecule breaks apart into O^{2-} and Zn^{2+}, and for triplet E_{ev} =2.5 V/Å with O^- and Zn^+ as the evaporation products; in essence the field strength required to break a double bond is almost twice that to break a single bond.

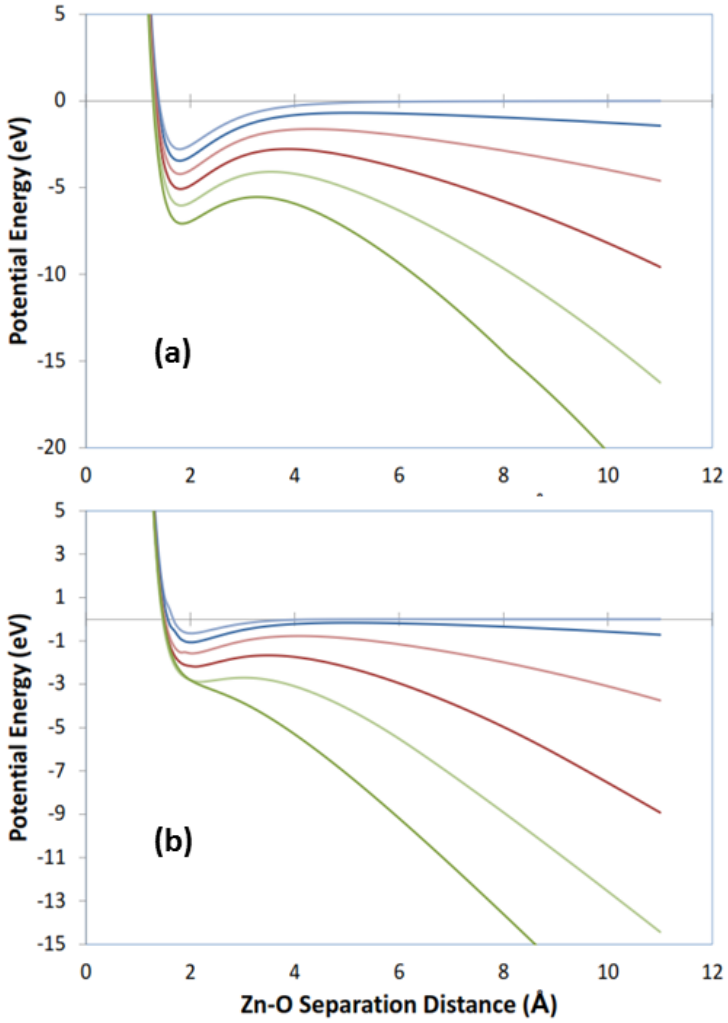

Figure 4.1 Potential energy curves of a ZnO molecule in a field of 0, 0.5, 1.0, 1.5, 2.0, and 2.5 V/Å (top-to-bottom) indicated by light blue, blue, pink, red, light green, and green colours, respectively. Panel (a) is the singlet and panel (b) is the triplet.

As we are interested in the effect of external electrostatic fields on properties of ZnO, the optical mode with a vibration component in the direction of the external electrostatic field is presented in Figure 4.2. For both the singlet and triplet the frequency increases slightly and then starts to decrease ever more rapidly until reaching zero at E_{ev}. Physically what occurs is that the bond is stretched in the field direction causing a decrease in the frequency until the bond breaks at which point the frequency is zero. The singlet has a higher frequency mode due to its shorter bond length. Finally we calculated the dipole moment of the singlet (triplet) and found that in both cases it increased linearly from 6 D (3.5 D) to 15.1 D (8.8 D) with a slope, i.e. molecular polarizability, of ≈ 1.8 DÅ/V (2.0 DÅ/V) until E_{ev} when it drastically increases due to the large separation of the charges.

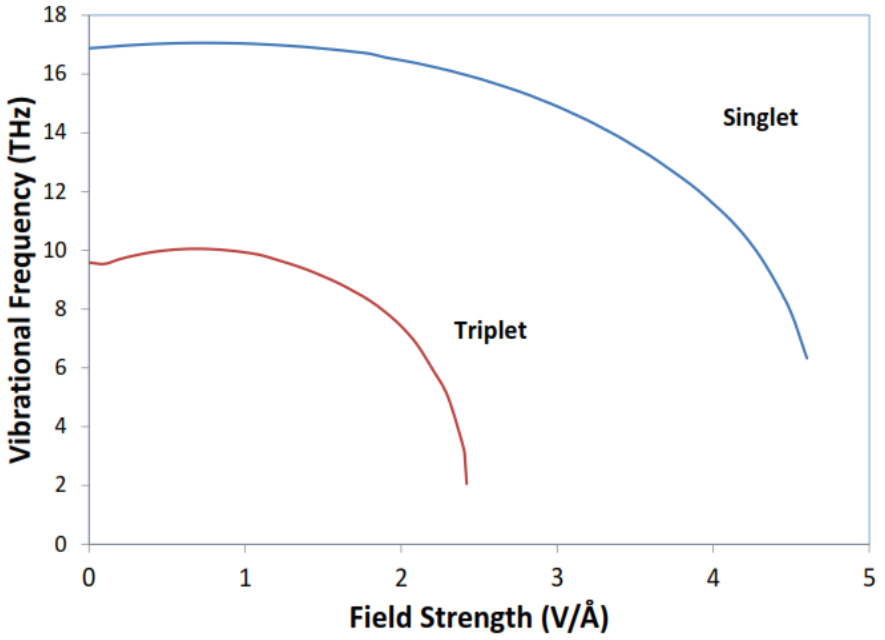

Figure 4.2 Vibrational modes of ZnO in a field.

4.3 $Zn_{10}O_7$ and Zn_9O_7 clusters

On our quest to understand field evaporation of solid ZnO we start with a small pyramidal cluster of $Zn_{10}O_7$ arranged in a wurtzite structure as shown in Figure 4.3. Keeping the lowest layer of the cluster fixed we apply a positive field (pointing up in the side view) and let the top 5 atoms relax in the field. We first follow the changes in $Zn_{10}O_7$ in a positive field and find that the top 5 atoms stretch upwards in the field until E_{ev} = 1.7 V/Å when the top Zn evaporates and leaves as Zn^+ which then post-ionizes in the uniform field into Zn^{2+}, as shown in Figure 4.4.

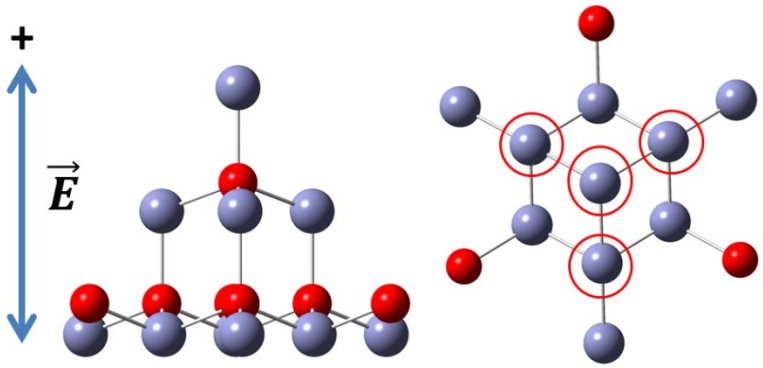

Figure 4.3 Side and top down view of the $Zn_{10}O_7$ cluster in its initial geometry. The red atoms are O and the grey are Zn with applied field direction indicated on the left. The locations of the underlying O are indicated by red circles in the top down view.

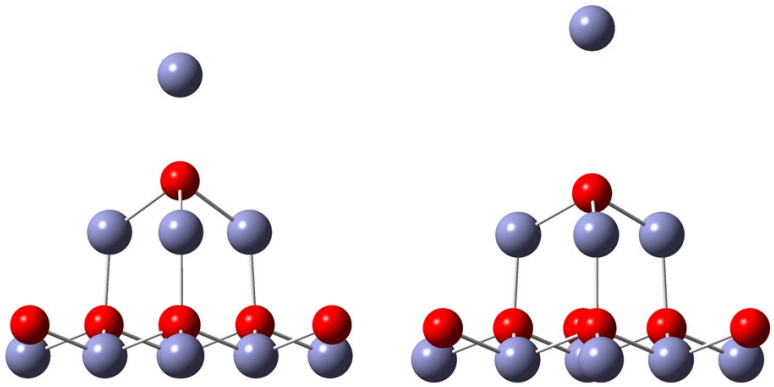

Figure 4.4 Dissociation of $Zn_{10}O_7$ in a field: (left) Stable configuration in a field of 1.6 V/Å; (right) Evaporation of the cluster in a field of 1.7 V/Å into Zn^+ and Zn_9O_7.

Increasing the field rapidly to 2.5 V/Å results in the direct evaporation of Zn as Zn^{2+}. After a Zn cation has evaporated there is a negative charge build up in the remaining cluster modifying the local electric field. In reality this negative charge would move into the metallic emitter tip and flow down the circuit. To recreate this situation we start the calculations again from a neutral Zn_9O_7 cluster, i.e. the same configuration as $Zn_{10}O_7$ minus the top Zn. A positive field is applied and there is a slight stretching of the top three Zns and a lowering of the top O until 2.5 V/Å when the stretching of the zincs appears to break their bonds to the oxygens on the lower layer but the stucture is still stable until E_{ev} =3.1 V/Å. At this stage a Zn^{2+} evaporates first followed by a Zn_2^{2+}together with an O^- which however combine into a Zn_2O^{2+}. Shown on the left in Figure 4.5 is the last stable configuraton for Zn_9O_7 in a field of 3.0 V/Å and on the right the cluster after evaporation at 3.1 V/Å with charges indicated by the atoms.

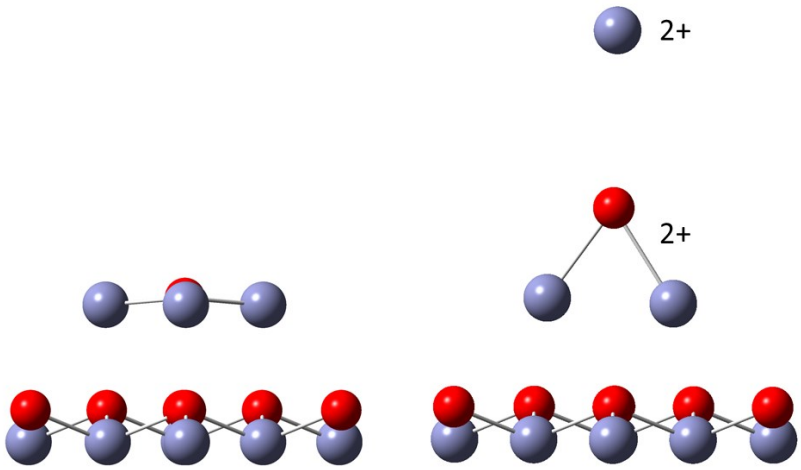

Figure 4.5 Dissociation of Zn_9O_7 in a field: (left) Stable configuration in a field of 3.0 V/Å; (right) Evaporation of the cluster in a field of 3.1 V/Å into various ions.

Now we answer the question of what would happen if we reverse field directions instead of continuing to apply a positive field to Zn_9O_7 after evaporation of the topmost Zn. As before, we neutralize Zn_9O_7 but now apply a uniform negative (pointing down) field. As the field increases rapidly the cluster goes through a series of different structures as shown in Figure 4.6. The top 4 atoms become increasingly open until they form a linear structure at 1.5 V/Å which persists until 2.1 V/Å. This opens a bit more at 2.2 V/Å with a Zn below the O separating (not shown) but then the 4 atoms form a small pyramid above the bottom layer from 2.3-2.5 V/Å with E_{ev} =2.6 V/Å. Alternatively if the field were to increase more slowly i.e. allowing the atoms to relax before increasing the field, then the structures from 0.1-0.7 V/Å are identical with a transition to the structure in the lower left of Figure 4.6 occuring at 0.8 V/Å instead of 1.5 V/Å and persisting until 2.1 V/Å. The evaporation products seen are ZnO^{2-}, Zn_2O^{2-}, O^{2-}, and Zn^- at field strengths up to 3.2 V/Å.

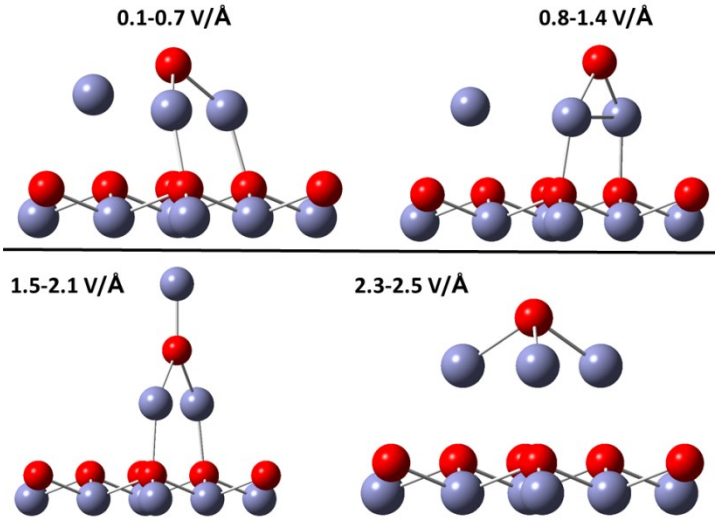

Figure 4.6 Changes in the structure of Zn_9O_7 in a negative field.

For a singlet the HOMO-LUMO gap is well defined but for triplets, such as the larger clusters, there are three gaps to consider: α (spin up electrons), β (spin down electrons), and a mix of α and β. In Figure 4.7 we plot the HOMO-LUMO gaps of the singlet ZnO molecule, $Zn_{10}O_7$ (β), ± Zn_9O_7 (α) with ± indicating applied field directions, and Si_{18} (α) up to E_{ev}. As we have discussed in the previous chapter the closure of the α or β HOMO-LUMO gap indicates that the insulator becomes conductive or metallizes with the result that an atom is field evaporated. This behaviour can be seen in Figure 4.7 with full closure of the gap for the Si_{18} cluster and partial closure of the gap for the ZnO clusters.

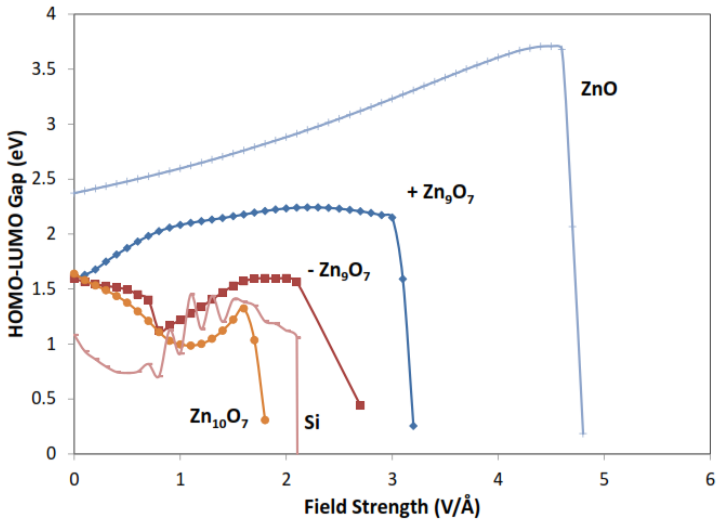

Figure 4.7 HOMO-LUMO gaps of a ZnO molecule, ZnO clusters, and a Si cluster in a field.

As discussed in the previous chapter the induced internal electric field will be reduced by more than the dielectric constant given in the classical electrostatic case, for ZnO (ϵ_r=8.5). Figure 4.8 shows the induced electric field profile along the central axis inside the pyramid cluster of $Zn_{10}O_7$ from the bottom layer through an O atom approximately 3.5 Å from the bottom and a Zn atom approximately 6 Å from the bottom; the fields for Zn_9O_7 and Si_{18} are qualitatively similar. The induced electric field is calculated using Eq. 27 in Chapter 1. One can see that the field is enhanced above the top Zn atom by a factor of three as above a metallic adatom [24]. The oscillations in the induced internal field are due to insufficient cancellation of the fields close to the position of the nuclei. At a field of 0.1 V/Å the average internal field (between 0 and 5 Å) corresponds approximately to the external field divided by the dielectric constant of ZnO (ϵ_r =8.5). At a field of 1.0 V/Å the internal field is decreased by a factor of 20. The Si_{18} cluster in a field of 2.0 V/Å has the internal field decreased by a factor of 1000, demonstrating that in such high electric fields the dielectric behaviour departs from that predicted by classical electrostatics.

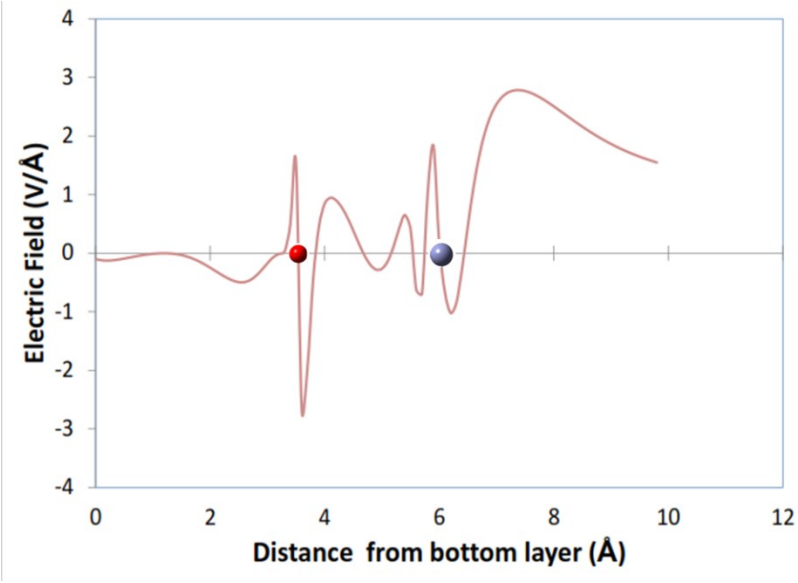

Figure 4.8 Induced electric field through the central axis of the $Zn_{10}O_7$ cluster caused by an applied field of 1.0 V/Å. The position of the Zn (grey) and O (red) atoms are shown.

Although the field is greatly reduced along a given axis we can also calculate the dielectric constant and polarizability of the entire cluster as a function of the applied electric field using a simple model. In this model the dielectric constant ϵ_r is given by

$$\epsilon_r = 1 + \frac{\vec{p}\cdot\vec{E}}{\epsilon_0 V \vec{E}\cdot\vec{E}} \tag{42}$$

where p is the calculated induced dipole moment of the cluster, ϵ_0 is the permittivity of free space, V is the volume of the cluster, and E is the applied electric field. In Figure 4.9 we see that the dielectric constants of the ZnO (Si) clusters are within 10% of their experimental values of ϵ_r =8.5(11.7) at low fields (< 0.6 V/Å) with greater variation for different clusters at higher fields. If the structure becomes more open, such as in the lower left panel of Figure 4.6, then the dielectric constant will be reduced. Abrupt changes in the dielectric constant indicate field-induced changes in the geometry of the small clusters and will most likely be smoothed for larger clusters. As the dielectric constant is a bulk parameter, and these are nanoclusters, one should not expect the dielectric constant to be the same for bulk and clusters. More importantly, upon field evaporation of an atom from a cluster the dielectric constant heads to infinity i.e. to that of a metal indicating metallization of the semiconductor or insulator.

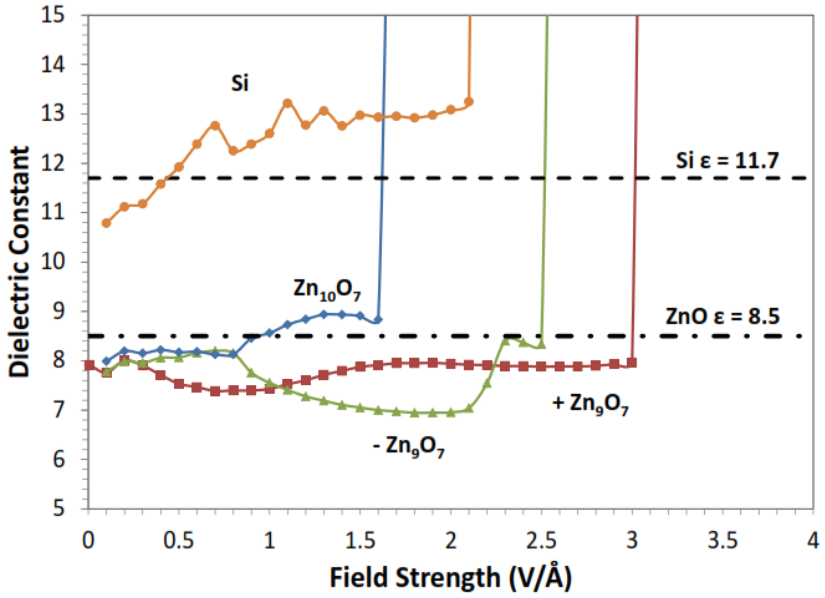

Figure 4.9 The dielectric constants of ZnO and Si clusters in a field with experimental values indicated by dashed lines.

The atomic (molecular) polarizability is given by

$$\alpha = \frac{\vec{p}\cdot\vec{E}}{4\pi\epsilon_0 n\vec{E}\cdot\vec{E}} \tag{43}$$

where n is the number of atoms (molecules). As one can see in Figure 4.10 we obtain good agreement with the experimental values of α=4.47 (5.38) Å^3 for the Z_9O_7 cluster and Si cluster, respectively. The polarizability of the $Zn_{10}O_7$ and - Zn_9O_7 clusters are higher than the experimental values due to the lone Zn at the top of the cluster which is easier to polarize than a Zn with higher coordination. The polarizability also increases dramatically upon field evaporation.

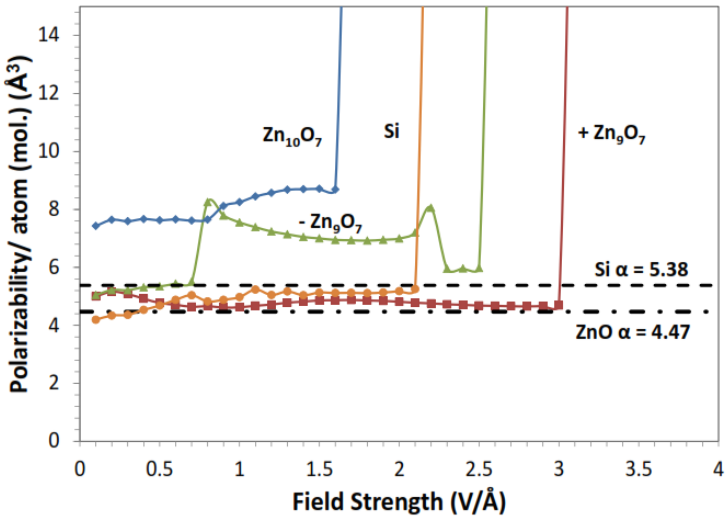

Figure 4.10 Atomic (molecular) polarizability of Si and ZnO clusters in a field with experimental values given by the dashed lines.

4.4 $Zn_{26}O_{26}$ Clusters

A $Zn_{26}O_{26}$ cluster arranged in a wurtzite structure is used as a model of the oxide layers on the metallic tip. To prevent drifting of the whole cluster in the applied electric field and to simulate the bulk we fix the geometry of the bottom half of the $Zn_{26}O_{26}$ cluster allowing however the electronic structure to reach self-consistency in the iterations. The top half of the cluster, which is allowed to relax, transforms to a graphitic-like structure in zero field, consistent with previous DFT calculations [90]–[93]. As the applied field increases the cluster is stretched but remains stable up to 2.5 V/Å.

To understand the mechanism of the strong field expulsion we look at the dielectric constant of the cluster, which can be estimated by applying the Clausius-Mossotti equation

$$\epsilon_r = \frac{1+8\pi\alpha/3V}{1-4\pi\alpha/3V}, \tag{44}$$

where α is the polarizability per molecule in the cluster for the applied field given by the second derivative of the energy with respect to the applied field, and V is the volume per molecule, which we simply take as the volume of the unit cell of the wurtzite bulk (containing 4 atoms) divided by 2 to account for 2 molecules per unit cell. The polarizability and the dielectric constant are presented in Figure 4.11, respectively. At fields lower than 2 V/Å, α and ϵ_r are within a factor of two of the experimental values of 4.01 $Å^3$/mol. and 8.81 [94] respectively at $E = 0$. As the field is increased from zero, α and ϵ_r decrease due to the fact that the static dipole moment of the cluster is in the same direction as the applied field. From 0.5 to 0.7 V/Å there is an increase in the polarizability and dielectric constant which is caused by a simultaneous field-induced vertical expansion (stretching) and horizontal contraction of the cluster. At 0.8 V/Å this trend changes and the cluster undergoes expansion vertically and horizontally. The external positive field has to counteract the inherent negative field. As the evaporation field strength is approached α and ϵ_r increase rapidly and eventually approach infinity as an indication of an insulator-to-metal transition.

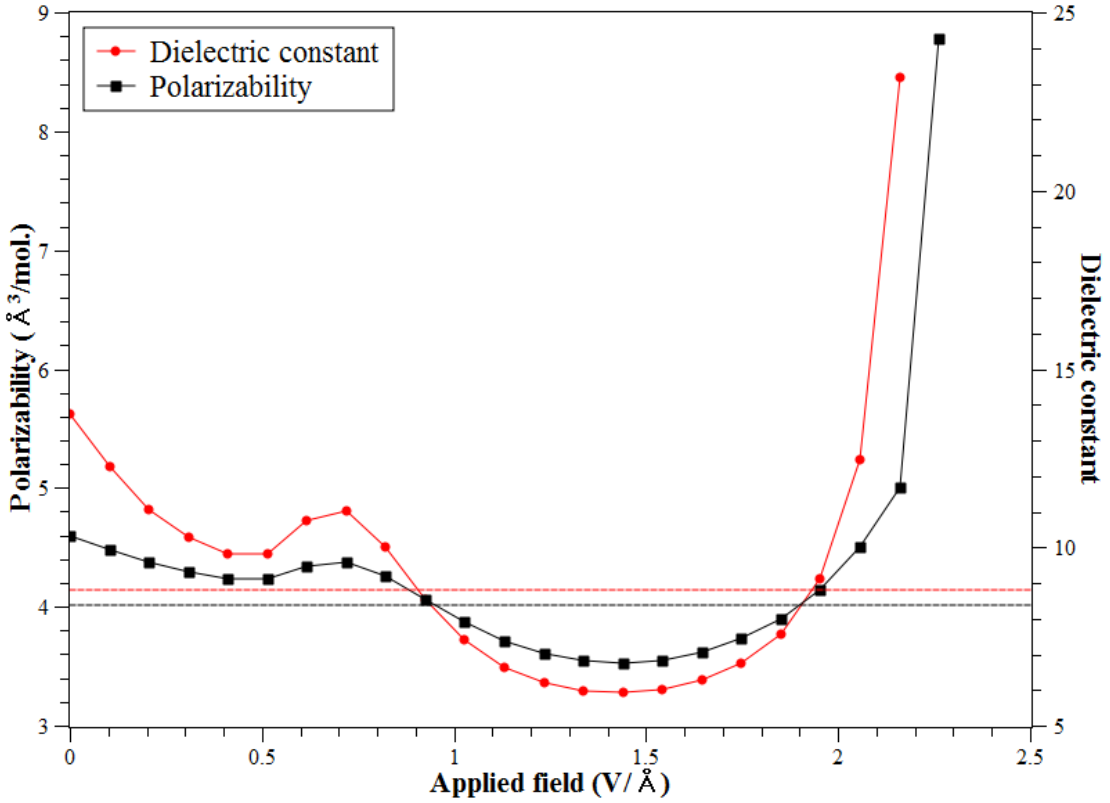

Figure 4.11 The polarizability (black) and dielectric constant (red) of the $Zn_{26}O_{26}$ cluster. The straight lines are the experimental values of ZnO wurtzite bulk [94].

In the previous section on small conical $Zn_{10}O_7$ and Zn_9O_7 wurtzite tips we found that the polarizability of the $Zn_{10}O_7$ cluster is approximately twice the experimental value, due to the dominant number of Zn atoms. Compared to that, the polarizability of the $Zn_{26}O_{26}$ cluster here is close to bulk values; this is important from a practical point of view, namely as a justification to use "small" clusters to simulate bulk properties. The criterions for how small a cluster can be are simply that (a) there is at least one additional layer around a unit cell, and (b) it must be stoichiometric.

An additional indication of metallization is the fact that the strong applied field leads to a shrinkage of the HOMO-LUMO gap of the cluster, as discussed in Chapter 3 and the previous section [10], [70], [85]. In Figure 4.12 we plot the HOMO-LUMO gap as a function of applied field strength. After an initial rise, the gap decreases steadily and

eventually drops to zero as the evaporation field is approached similar to the smaller clusters.

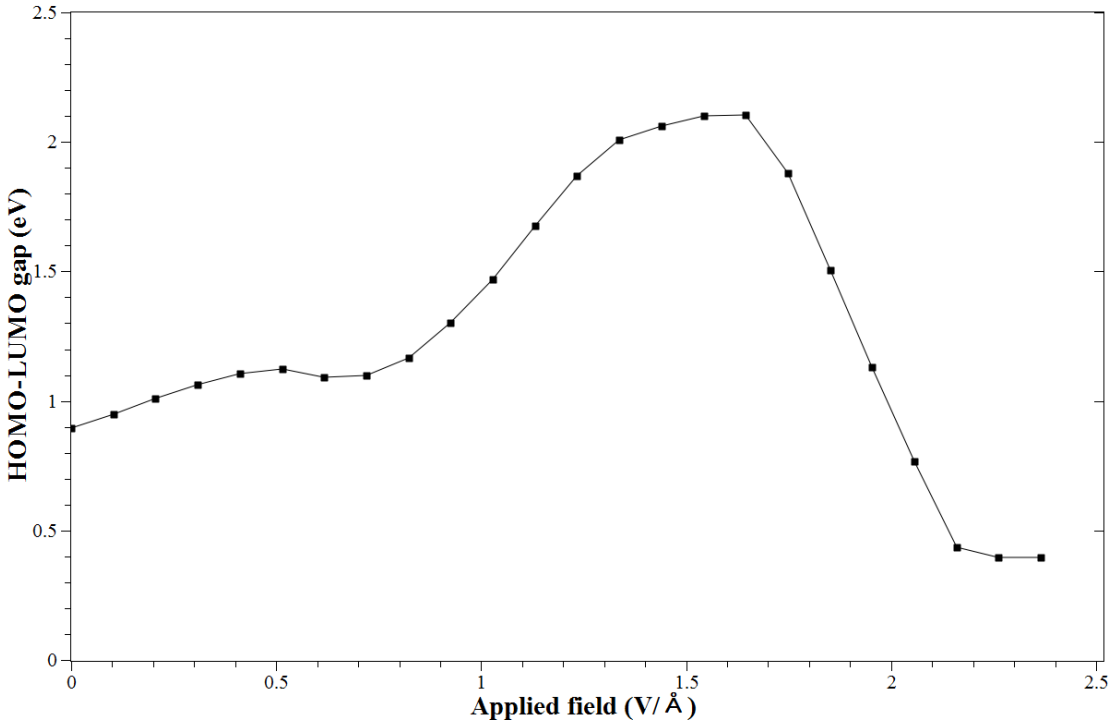

Figure 4.12 The HOMO-LUMO gap of the $Zn_{26}O_{26}$ cluster.

The HOMO-LUMO gap of a cluster is the equivalent of the band gap of the corresponding bulk material. For the bulk, the applied field leads to a band-bending in the surface region. Experimental evidence of the shrinkage of the band gap can also be inferred from the strong enhancement of the optical absorption, observed recently in MgO which will be discussed in the next chapter [95].

Next we look into the field evaporation process of ZnO itself. At the evaporation field strength the cluster is no longer stable and DFT geometry optimization does not converge to a stable minimum. What is observed as the iterations proceed is the motion of ions away from the surface. This is demonstrated in Figure 4.13 for a field of 2.6 V/Å. Note that the snapshots of the iterations do not stand for the exact evaporation pathway. However, they can still be used to obtain information on the evaporated species and also on the time scale of field evaporation. In the beginning the edge of the cluster is stretched

strongly and disintegration starts at the corner. Initially only Zn atoms evaporate as Zn^{2+}, as shown in the first row. After that an O_2^+ evaporates followed by a Zn_2O^{3+} which is post-ionized and breaks down into a Zn^{2+} and a ZnO^{2+} at a height of ~4 Å where there is still sufficient overlap between the wave functions on the ion and the cluster. At the next stage more Zn^{2+}, ZnO^{2+} and O_2^+ are produced.

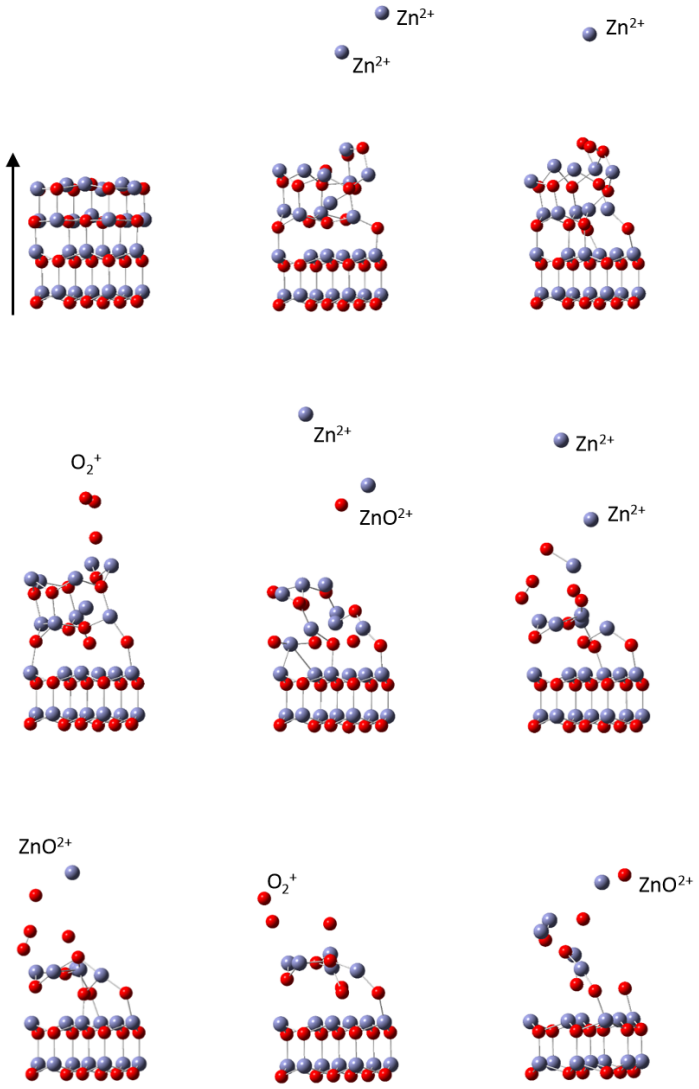

Figure 4.13 The evaporation of the $Zn_{26}O_{26}$ cluster at a field of 2.6V/Å. Shown are snapshots of the iterations during the calculation. The arrow indicates the direction of the applied electric field. The bottom two layers are fixed.

To obtain information on the time scale involved in the field evaporation we follow the energy V of a Zn atom at the corner of the cluster as a function of its position z from the

geometry optimization as it evaporates (Figure 4.14). The force f can be approximately given by $f \approx \Delta V/\Delta z$ amounting to about 1.0 eV/Å. According to Newton's equation of motion a mass m will travel under a constant force f a distance Δz in a time $t = [2m\Delta z/f]^{1/2}$ which gives the time scale it takes for the Zn atom to be evaporated of $\sim 10^{-14}$ s. The Zn is partially charged at the surface (due to the internal polarization) and becomes a Zn^{2+} during the evaporation. To estimate the ionization time scale we look at the electron potential energy through the corner of the cluster at field strength of 2.4 and 2.5 V/Å showing also the two highest HOMOs (Figure 4.15). The tunneling time of the electron to tunnel from the Zn to the cluster in 2.4 V/Å calculated using the WKB approximation [96] is $\sim 10^{-16}$ s, two orders of magnitude faster than the evaporation time; at 2.6 V/Å the electron is free to travel through the "metallic" cluster.

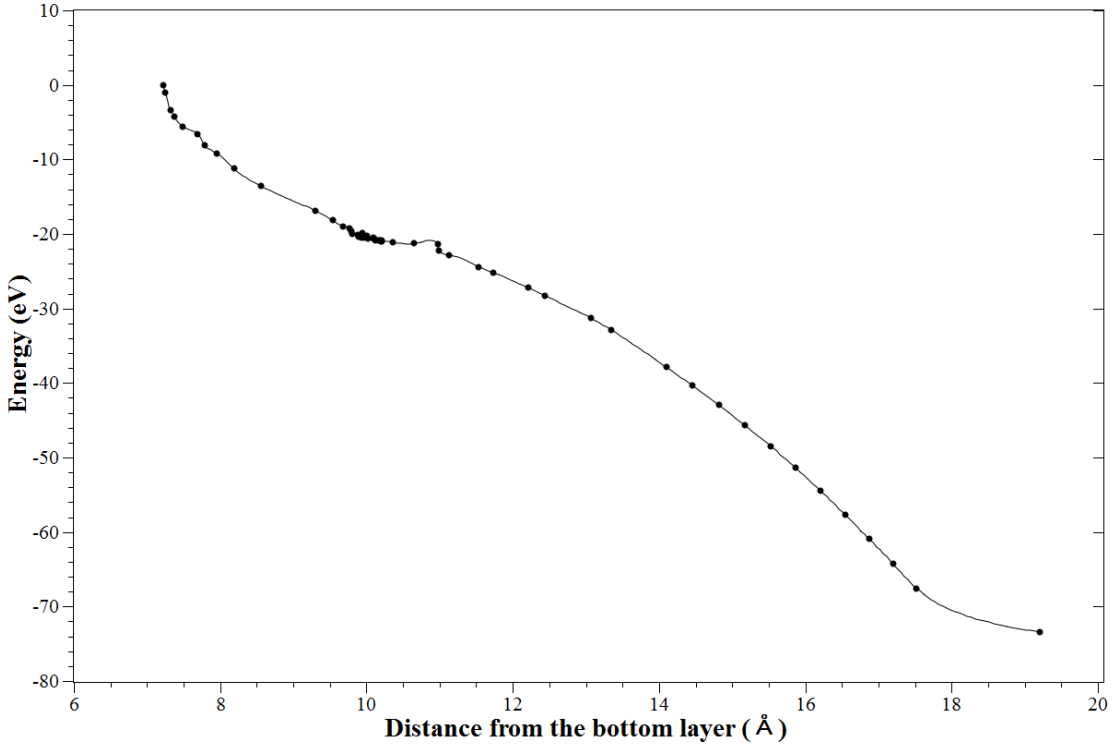

Figure 4.14 Potential energy of the first evaporated Zn as a function of the position z during the evaporation at a field of 2.6 V/Å.

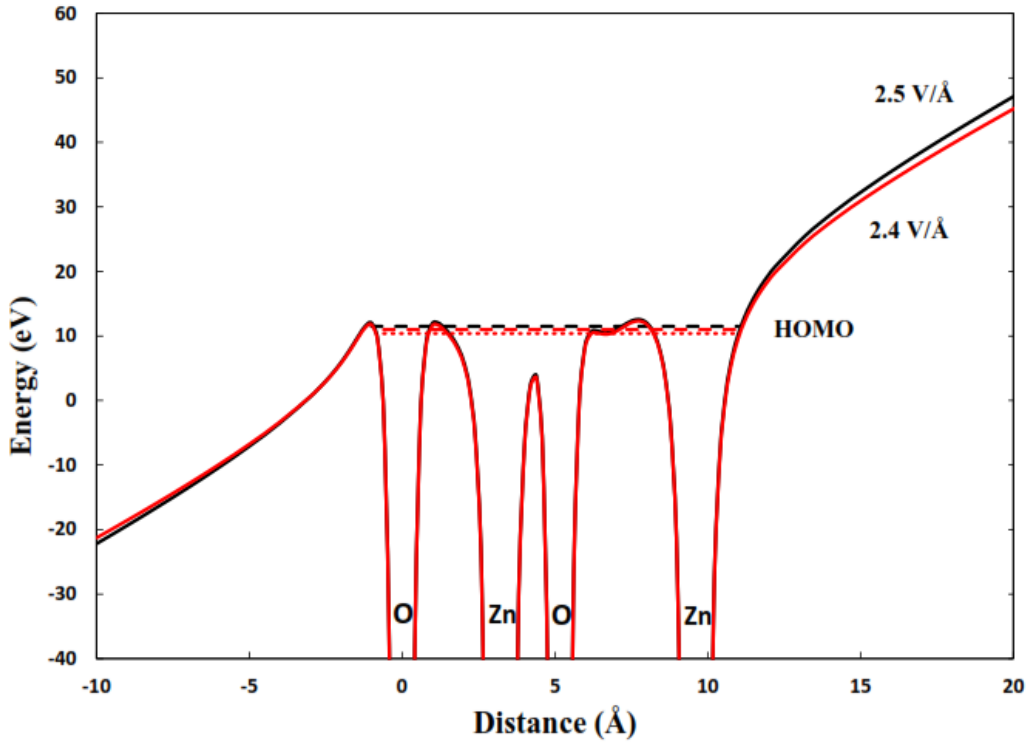

Figure 4.15 The electron potential energy through the corner of the cluster. The HOMOs are indicated by the dashed lines. The dotted line is the second-HOMO at 2.4 V/Å.

In our calculations the first evaporated atom is always a Zn at the corner of the top layer, which has a coordination of 2 and a binding energy of 6.4 eV. In comparison with this, the other Zn has a coordination of 3 and a larger binding energy of 7.6 eV. The binding energies of the outer O and the central O are 10.5 eV and 12.1 eV, respectively. The local induced field is also dependent on the coordination. At the evaporation field E_{ev} = 2.5 V/Å, the field enhancement factor at the corner Zn is ~2.5, resulting in a local field of ~6 V/Å. Meanwhile, the enhancement factor at other atoms is ~1.5 and the local field is ~4 V/Å. This is consistent with previous calculations on the conical ZnO tips [85] and single-walled carbon nanotubes [97].

The evaporated species we get are Zn^{2+}, ZnO^{2+}, O_2^+ and O^+, all of which have been observed in various APT experiments [49], [75], [87], [98]. Looking in detail at the various experiments one notes that their mass spectra differ significantly in the abundance of the various ions. Based on our results we can speculate about a possible

cause for these discrepancies: they might be simply due to the fact that in the experiment it is difficult to determine the local field strength accurately, because it depends crucially on the tip shape and the thickness of the oxide layer. Another cause for the difference is the fact that the dissociation field of a ZnO^{2+} molecule is only 0.5 V/Å so that the ion can break apart on its way away from the surface and be observed in some of the experiments as additional Zn^{2+}; this again may be more likely for some tip shapes than others.

4.5 Conclusions

We have demonstrated the field-induced insulator-to-metal transition of a ZnO wurtzite cluster as the applied field strength approaches the evaporation field strength. This can be seen in the reduction of the internal field by a factor greater than the dielectric constant, 20 instead of 8.5 for the $Zn_{10}O_7$ cluster, 1000 instead of 11.7 for the Si cluster, and 100 instead of 10 for a MgO cluster, see Chapter 3. The field above the top zinc in $Zn_{10}O_7$ is enhanced by a factor of three in an applied field of 1.0 V/Å which is the same enhancement for a metal tip. Using a simple model we showed that one can calculate bulk quantities such as the dielectric constant and polarizability from small clusters with reasonable accuracy. The rapid increase of the dielectric constant to infinity upon field evaporation of an atom confirms metallization of the semiconductor or insulator. The HOMO-LUMO gap declines towards zero. This behaviour is seen for the Si cluster and ZnO clusters with closure and partial closure of the gaps at evaporation. Such a transition for a MgO cluster was shown in the previous chapter.

We also analyze the optical phonon spectrum of ZnO molecules that is varying with the applied field. It is found that the normal frequencies decrease first smoothly and then exponentially as the electric field increases, with the frequencies going to zero upon fragmentation. Reversal of the applied electric field on Zn_9O_7 produces ZnO^{2-}, Zn_2O^{2-}, O^{2-}, and Zn^- ions and looks like an interesting option to remove O from the material. However, the effects of field emission are not taken into account with this DFT model. Our cluster calculations also show that the evaporated species in a positive field are Zn^+, Zn^{2+}, Zn_2O^{2+}, ZnO^{2+}, O_2^+ and O^+. These ions have been observed in APT mass spectra

[49], [75], [87], [98]. We also observe the fragmentation of ionic compound molecules such as Zn_2O^{3+} and ZnO^{2+}.

One of the current issues in the APT of oxides is the difficulty in measuring the accurate stoichiometry, for instance, due to the overlap of Zn^{2+} and O_2^{+} in the mass spectra. Our calculations suggest that the peak is Zn^{2+}, in agreement with Mancini's experiments [98] using different Zn isotopes. A serious problem with APT experiments on ZnO is the fact that the ion yield is not stoichiometric with oxygen ions missing in mass spectra. Our calculations confirm this finding: we see that field evaporation always starts with the Zn atoms at the corner of the top layer desorbing first, due to the fact that field enhancement is largest there. After Zn ions evaporate, the cluster becomes O-rich, and surface diffusion of O is effective above 100K. This leads to associative thermal desorption of neutral molecular oxygen which cannot be detected in APT. However, some O_2 can get field-ionized showing up in APT measurements but not enough for stoichiometry.

CHAPTER 5 Field-induced metallization of semiconductors

This chapter has been published in NanoLetters (vol. 14, pp. 6066–6072, 2014) as an article with the title "Do Dielectric Nanostructures Turn Metallic in High-Electric dc Fields?" [95]. The authors are E. P. Silaeva, L. Arnoldi, M. L. Karahka, B. Deconihout, A. Menand, H. J. Kreuzer, and A. Vella. Markus Karahka's contribution to this work consists of the DFT calculations and drafting 10% of the manuscript. Permission to use this work has been granted by the editor of NanoLetters, a copy of the permission letter is attached to this thesis. Reprinted (adapted) with permission from (NanoLetters (vol. 14, pp. 6066–6072, 2014)).

Abstract

Three-dimensional dielectric nanostructures have been analyzed using field ion microscopy (FIM) to study the electric dc field penetration inside these structures. The field is proved to be screened within a few nanometers, as theoretically calculated, taking into account the high-field impact ionization process. Moreover, the strong dc field of the order of 0.1 V/Å at the surface inside a dielectric nanostructure modifies its band structure leading to a strong band gap shrinkage and thus to a strong metal-like optical absorption near the surface. This metal-like behavior was theoretically predicted using first-principle calculations and experimentally proved using laser-assisted atom probe tomography (APT). This work opens up interesting perspectives for the study of the performance of all field-effect nanodevices, such as nanotransistor or super capacitor, and for the understanding of the physical mechanisms of field evaporation of dielectric nanotips in APT.

Do Dielectric Nanostructures Turn Metallic in High-Electric dc Fields?

Nanostructures are rapidly making inroads into advanced device systems wherein they could be subjected to high current densities, electric fields as well as thermal transients due to their typical geometries and size-dependent properties [99]–[101]. In the device

context, the latter mostly include electronic, optical, or optoelectronic properties that are also mutually intertwined in interesting ways on such tiny length scales. In many cases, the modifications are so dramatic that none of the bulk considerations seem to have any relevance to the device functionalities. Thus, in the emergent and futuristic nanoelectronic devices a precise and direct understanding of the properties on that specific length scale is a must. Among various issues that are important to nanodevices, the implications of very high electric fields for the electronics states (band structure), carrier transport, and optical excitation are perhaps the most relevant because in many devices such as field-effect transistors and supercapacitors, geometry effects lead to highly enhanced local fields. Although several phenomena pertaining to the effects of high fields on solids have been addressed theoretically and experimentally in the past [55], [102]–[104], understanding of the dramatic changes in the response and properties of a dielectric subjected to high electric fields is severely lacking, especially insofar as the intriguing observation of their metal-like behavior is concerned. Because the consequences of enhanced local fields can be easily examined in the case of metallic nanostructures via field emission, one could envision the application of this method in the case of dielectric as well. This is nontrivial however in view of the possibility of dielectric breakdown effects. Thanks to the recent developments in the use of laser-assisted atom probe 3D tomography technique, it is now possible to control these phenomena to unprecedented accuracy and address issues that could not be otherwise addressed before. In this work, we apply this technique to the observation of high electric field-induced metal-like behavior of dielectrics that has been a subject of a long debate.

Depending on the field strength, several different physical processes can be responsible for this behavior. At fields of the order of 0.01–0.1 V/Å, light absorption was predicted to be enhanced due to the Franz-Keldysh effect, when photon-assisted tunneling leads to a decrease of the band gap of the dielectric [105], [106]. Higher fields (0.1–1 V/Å) cause the recently predicted adiabatic metallization and increased polarizability of the dielectric films due to Wannier–Stark localization [107], [108]. Above 1 V/Å, Zener interband tunneling takes place [55], [102], injecting a substantial number of free electrons into the conduction band of the dielectric. High-field band-bending can cause the accumulation of

high (semimetallic) densities of free carriers at the surface of a semi-infinite low-resistivity semiconductor [11], [17], [109]. All of these phenomena were predicted theoretically in the references cited above but never confirmed experimentally in the case of strong dc field. In this work, to create a strong dc field dielectrics are nanostructured in the form of nanotips, such as samples used in field ion microscopy (FIM) and APT [11]. Note that these nanotips have a typical size and shape of a functional nanostructure found in many nanoscale devices and in many high-field applications. Moreover, the nanotips are not only subjected to strong electrostatic fields but can also be illuminated with light to trigger field emission. Hence, the change of the optical properties of the sample under a high field can easily be probed.

In this chapter, we show by a combination of experiment and theory that (i) internal fields of the order of 0.1 V/Å are generated at the apex of a dielectric nanotip when biased to a high voltage; (ii) this field penetrates a few nanometers into the tip surface; (iii) such a high field causes the band gap to decrease leading to metallization of the dielectric tip surface, thus, strongly enhancing its optical absorption. Using APT, we follow these changes of the optical properties. DFT calculations are also reported that confirm this new picture of dielectrics behavior in high dc fields.

This work opens a new understanding of the role of the electric field in laser-matter interaction and in the laser-assisted field evaporation of nonmetallic materials. This work also closes a long debate inside the APT community on the light absorption process and the following field evaporation of dielectric samples. Although APT is experimentally quite successful in applications for atom-resolved material analysis [76], [110]–[115], the mechanisms of laser-assisted field evaporation, the fundamental process that forms the basis of APT, of nonmetallic tips remained unclear.

To characterize the tips and map out the field distribution we use FIM, a projection microscope able to image the surface of the sample with atomic resolution [11]. The sample is introduced into a high vacuum chamber and is cooled down to a temperature of $T = 20$ K. A schematic representation of the chamber is shown in Figure 5.1a. An

imaging gas, Ne, at a pressure of about 10^{-5} mbar is field ionized close to the tip surface due to tunneling, provided the field at the tip apex is higher than the ionization field of Ne (E_i = 3.5 V/Å). Positive ions of Ne^+ are, then, projected onto the detector and an image of the surface of the sample with atomic resolution is obtained, as shown in Figure 5.1b for MgO. More details on the Experimental Method are reported in the supporting information [95]. This measurement shows that the field inside the MgO tip is on the order of E_i/ϵ_r = 0.35 V/Å, where ϵ_r = 10 is the relative dielectric constant of MgO. A scanning electron microscope (SEM) image of the MgO tip is reported in Figure 5.1c.

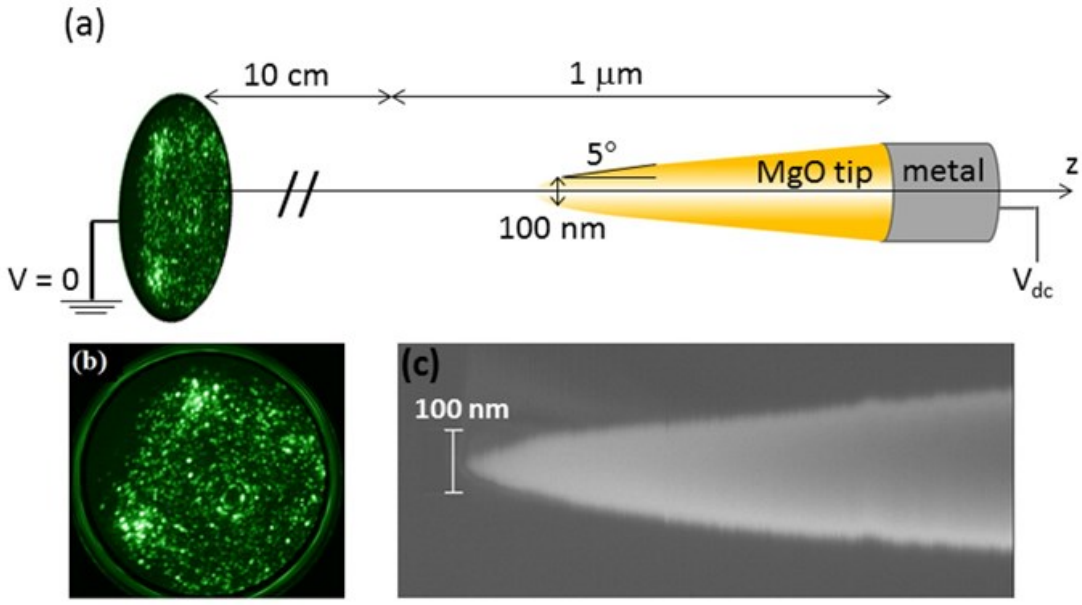

Figure 5.1 (a) Schematic diagram of FIM experimental setup, V_{dc} = 8 kV. (b) FIM image of MgO at 20 K with 10^{-5} mbar of Ne as imaging gas.(c) SEM image of MgO tip used in the experiments.

The field at the apex of the MgO tip can be calculated by solving the Laplace equation for the geometry in Figure 5.1a. For an applied voltage of V_{dc} = 8 kV we get a field inside the tip of about 0.05 V/Å, see Figure 5.2a at 0 ns. It is several times lower than the value obtained experimentally [10], [62]. In reality, under this field the free carriers move inside the tip to screen the field in the bulk of the tip and increase the field at its apex, which is not accounted for in the classical electrostatic picture.

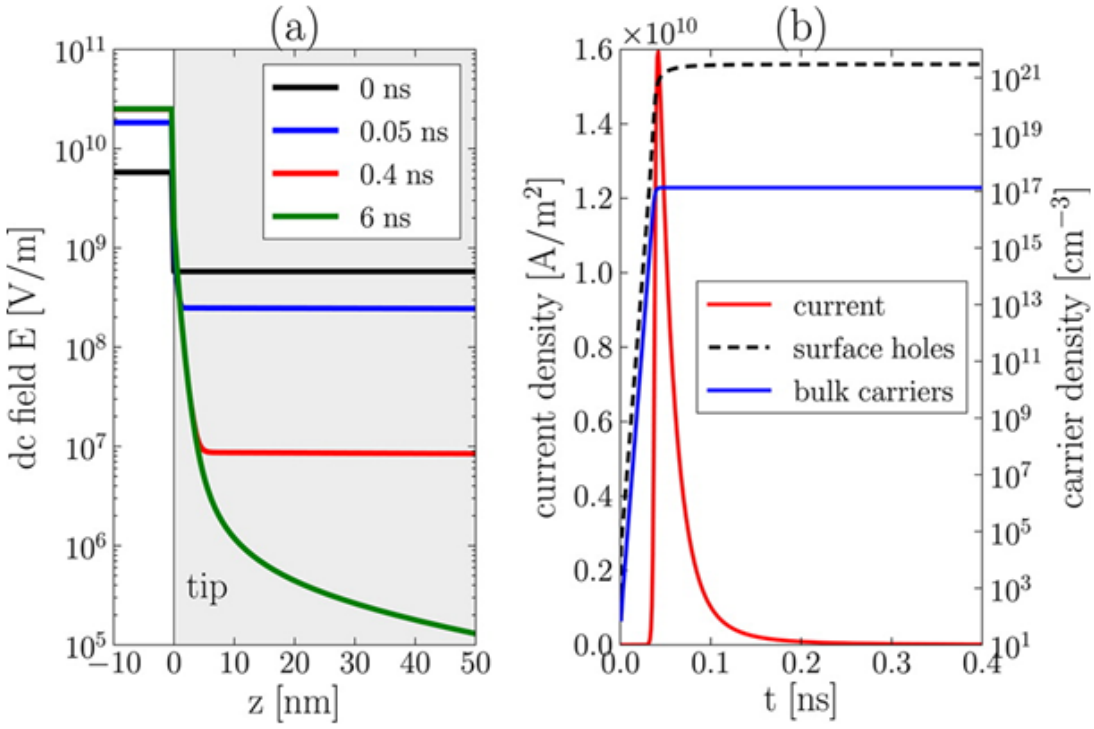

Figure 5.2 (a) Field distribution along a MgO tip axis of symmetry in vacuum (white) and inside the tip (gray zone) at different times after application of voltage, obtained from the numerical solution of eqs 45. (b) Time evolution of average current (solid red line), average carrier (electron and hole) density in the bulk of MgO tip (solid blue line), and surface carrier density (dashed line) at the surface of MgO tip after application of voltage.

The screening of the field can be described using a simplified, that is, one-dimensional model (parallel to the tip axis of symmetry) valid for 3D spherical geometries with radius of curvature not much less than 20 nm [109]. To reproduce the same initial field in 1D as obtained by solving the Laplace equation in 3D, the tip is represented by a short vacuum region (300 nm) and a long MgO "line" (13 μm); a positive potential difference V_{dc} is applied between the ends. Then we solve numerically the drift-diffusion equations for the density of electrons n_e and holes n_h together with the Poisson equation for the potential V to obtain the evolution in time t of the field inside this system along its axis of symmetry z:

$$\begin{cases} \dfrac{\partial n_{\mathrm{h}}}{\partial t} + \dfrac{1}{e}\dfrac{\partial}{\partial z}J_{\mathrm{h}} = S_{\mathrm{h}} - \dfrac{n_{\mathrm{h}}}{\tau} \\ \dfrac{\partial n_{\mathrm{e}}}{\partial t} - \dfrac{1}{e}\dfrac{\partial}{\partial z}J_{\mathrm{e}} = S_{\mathrm{e}} - \dfrac{n_{\mathrm{e}}}{\tau} \\ \dfrac{\partial}{\partial z}\varepsilon_{\mathrm{r}}\left(\dfrac{\partial V}{\partial z}\right) = -\dfrac{e}{\varepsilon_0}(n_{\mathrm{h}} - n_{\mathrm{e}}) \end{cases} \tag{45}$$

where e is the absolute value of electronic charge and ϵ_0 is the vacuum permittivity. The electron and hole current densities J_{e} and J_{h}, respectively, are given by

$$J_{\mathrm{h}} = e\mu_{\mathrm{h}}En_{\mathrm{h}} + eD_{\mathrm{h}}\frac{\partial n_{\mathrm{h}}}{\partial z}; \quad J_{\mathrm{e}} = e\mu_{\mathrm{e}}En_{\mathrm{e}} - eD_{\mathrm{e}}\frac{\partial n_{\mathrm{e}}}{\partial z} \tag{46}$$

with the field $E = -\partial V/\partial z$. The diffusion coefficients D_{h}, D_{e} and mobilities μ_{h}, μ_{e} of holes and electrons are considered for Fermi–Dirac statistics [54]. The equilibrium values are taken to be $\mu_{\mathrm{h}} = \mu_{\mathrm{e}} = 10$ cm^2/(Vs) [116] and $D_{\mathrm{h}} = D_{\mathrm{e}} = \mu_{\mathrm{e}}k_{\mathrm{B}}T/e$ where k_{B} is Boltzmann constant.

The recombination time $\tau = 300$ ms is obtained experimentally as reported in the supporting information [95]. The generation rate of holes S_{h} and electrons S_{e} depend on the presence of the high dc field inside the dielectric. The initial field inside the tip (0.05 V/Å) is lower than the typical field for metallization that has been shown to happen at internal fields higher than 0.1 V/Å [107]. Moreover, this field is lower than the critical field needed for the Zener-type interband tunneling [103], [108]

$$E_{\mathrm{crit}} = \frac{\varepsilon_{\mathrm{gap}}}{ea} \sim 1.8\ \mathrm{V\AA^{-1}} \tag{47}$$

where $\varepsilon_{\mathrm{gap}} = 7.8$ eV is the band gap of MgO and $a = 4.2$ Å is its lattice constant. However, this field is high enough to cause carrier generation by impact ionization [117]

$$S_{\mathrm{h}} = S_{\mathrm{e}} = \frac{\kappa}{e}(|J_{\mathrm{e}}| + |J_{\mathrm{h}}|) \tag{48}$$

where κ is the coefficient of impact ionization given by [118]

$$\kappa = \kappa_0 \exp\left(-\frac{H}{E}\right) \tag{49}$$

Unfortunately, the constants κ_0 and H are not known for MgO. We take $\kappa_0 = 6.5 \times 10^{13}$ m^{-1}reported for SiO_2 [118]. The value of H is determined experimentally to be 1.5×10^{10} V/m, see the supporting information [95]. Now, the system of eqs 45-49, describing the field screening inside the tip, can be solved numerically. The initial carrier density is taken to be 6×10^2 cm^{-3}. This value is calculated from the reported value of resistivity of MgO 10^{13} Ohm·m [119]with the known mobility. The potential is fixed to zero at the left boundary and to 8 kV at the right boundary.

At the initial time, the drift current of carriers is strong enough to cause the generation of electron–hole pairs through impact ionization. This leads to a rapid increase of the average carrier (electron and hole) density up to 10^{17} cm^{-3} and current density in the bulk of MgO tip (Figure 5.2b) and, thus, the increase of surface hole density up to a semimetallic value of $3 \times 10^{21}$$cm^{-3}$ and rapid field screening (Figure 5.2).

The field in the bulk of MgO tip decreases below 10^{-5} V/Å leading in turn to the decrease of impact ionization rate, and the carrier generation stops. The average carrier current also decreases because diffusion tends to balance the drift current. At the same time, the surface field in vacuum increases from 0.5 V/Å up to 3 V/Å (Figure 5.2a). After the establishment of a stationary condition, the recombination of the excess carriers takes place everywhere inside the sample except at the surface due to charge separation [56]. The electron and hole densities have then the spatial profiles typical for stationary band-bending in semiconductors under high positive dc field [54]. The holes accumulated at the surface of MgO can also be trapped at low coordinated sites [120]. Note also that while screening is going on the electric current is very high. However, it does not lead to the breakdown of the tip due to its very short duration (∼100 ps).

The field is quite strong within the screening distance of a few nanometers (Figure 5.2a) where it can strongly affect the optical properties of the dielectric. To understand this phenomenon we use DFT [40] to investigate the electronic structure of a MgO cluster of $3 \times 3 \times 3$ atoms in the presence of external electrostatic fields, see Figure 5.3. In Figure 5.4a, we plot the HOMO–LUMO gap of the cluster as a function of field strength; the HOMO–LUMO gap in clusters translates into the band gap in bulk. The HOMO–LUMO gap strongly decreases with the field and shrinks to zero at the evaporation field strength, calculated here to be $E = 2.6$ V/Å, which is in agreement with Durach et al [107] where the band gap collapses and resulting metallization of the dielectric is found to be at an internal field of $E/\epsilon_r = 0.1$ V/Å or greater. Further increasing the field leads to cluster disintegration and the evaporation of a Mg atom as an Mg^{2+} ion. We have made several checks to ensure that our cluster is sufficiently large. (1) We repeated the calculations for a larger $4 \times 4 \times 4$ cluster (Figure 5.3) and found a similar evaporation field strength and the similar band gap dependence on the field but a larger HOMO–LUMO gap of 5.3 eV at zero field as expected, see Figure 5.4b. (2) From the electric dipole moment, we extracted the polarizability in small fields to be 3.1 $Å^3$ for both cluster sizes, which is in good agreement with the experimental value 3.3 $Å^3$. (3) From the DFT calculations, we can also determine the static dielectric constant to be 8.5 for the small cluster and 9.5 for the large cluster, again in excellent agreement with experiment. (4) It is noteworthy that the polarizability and dielectric constant go to infinity at the evaporation field strength as an indicator of metallization, see Figures in the supporting information [95].

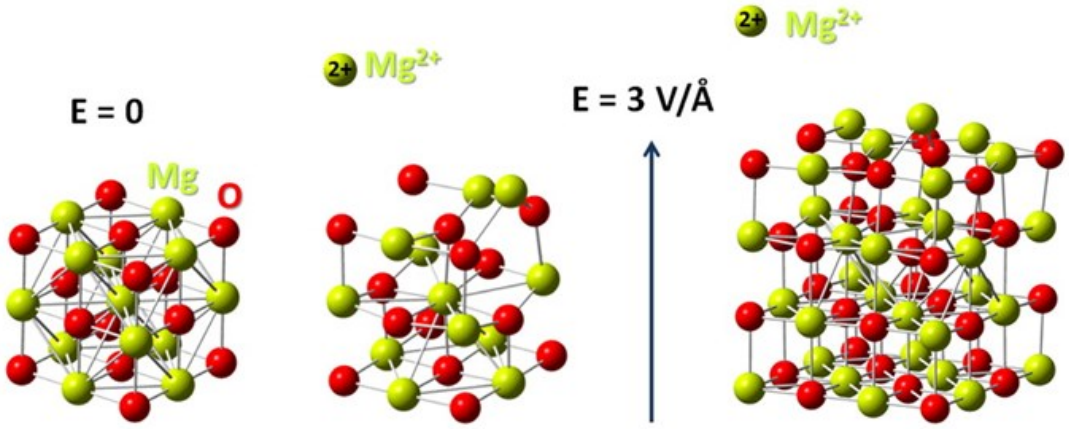

Figure 5.3 Atomic clusters of 3 × 3 × 3 atoms at zero field (left image) and of 3 × 3 × 3 and 4 × 4 × 4 atoms at field E = 3 V/Å (middle and right image, respectively). Mg is in yellow and O is in red. Arrow indicates the direction of the field E, considered in DFT calculations.

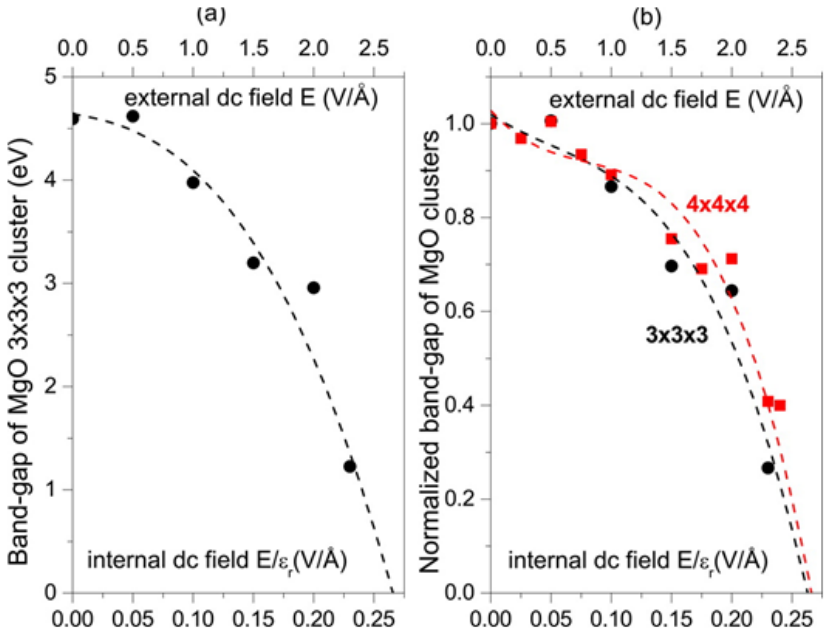

Figure 5.4 (a) HOMO-LUMO gap of MgO cluster of 3 × 3 × 3 atoms as a function of the dc field: external E and internal E/ϵ_r, calculated by DFT. (b) HOMO-LUMO gap normalized by zero-field gap as a function of dc field for 3 × 3 × 3 MgO cluster (black round dots) and for 4 × 4 × 4 MgO cluster (red square dots). Absolute value of HOMO-LUMO gap of 4 × 4 × 4 cluster at zero field is calculated to be 5.3 eV. Dashed curves is a polynomial fitting of the points from DFT calculation.

To prove experimentally that a high dc field induces strong metal-like optical absorption due to the collapse of the band gap at MgO tip apex we use laser-assisted APT [121]. The detection rate of field-evaporated ions is measured as a function of laser fluence F_{laser} of a 500 fs laser pulse at 343 nm wavelength and 100 kHz repetition rate.

Different physical mechanisms can be responsible for photodesorption of atoms from dielectric surfaces [59], [65], [122], [123]. How exactly it happens under high dc field during APT analysis has not been yet understood. However, it was experimentally demonstrated that the evaporation rate increases nonlinearly with temperature [124]. This experimental behavior was explained by different theoretical models [59], [122]. For all of them, the evaporation rate follows an Arrhenius law [11]

$$\phi = \nu\langle N\rangle\tau_{\text{evap}}\exp\left(-\frac{Q_{\text{n}}}{k_{\text{B}}T}\right) \tag{50}$$

where ν is the surface vibration frequency, $\langle N\rangle$ is the number of kink site atoms within the field of view of the detector, τ_{evap} is the evaporation time, Q_{n} is the activation barrier, and T is the tip temperature at the surface. The detection rate (φ) is lower than the evaporation rate due to the detector efficiency (q = 0.5)

$$\varphi = q\phi \tag{51}$$

After the interaction with the laser pulse (for any of the possible mechanisms), the tip temperature increases due to laser energy absorption

$$T = T_0 + \gamma F_{\text{laser}} \tag{52}$$

with γ a proportionality factor related to the absorption properties of the sample. Hence, to measure this γ factor the voltage applied to the sample was fixed at V_{dc} = 9.3 kV (Figure 5.5a) and the base temperature at T_0 = 80 K. Then, the ion detection rate was measured as a function of laser fluence. The same procedure was repeated for T_0 = 20 K [54], [125].

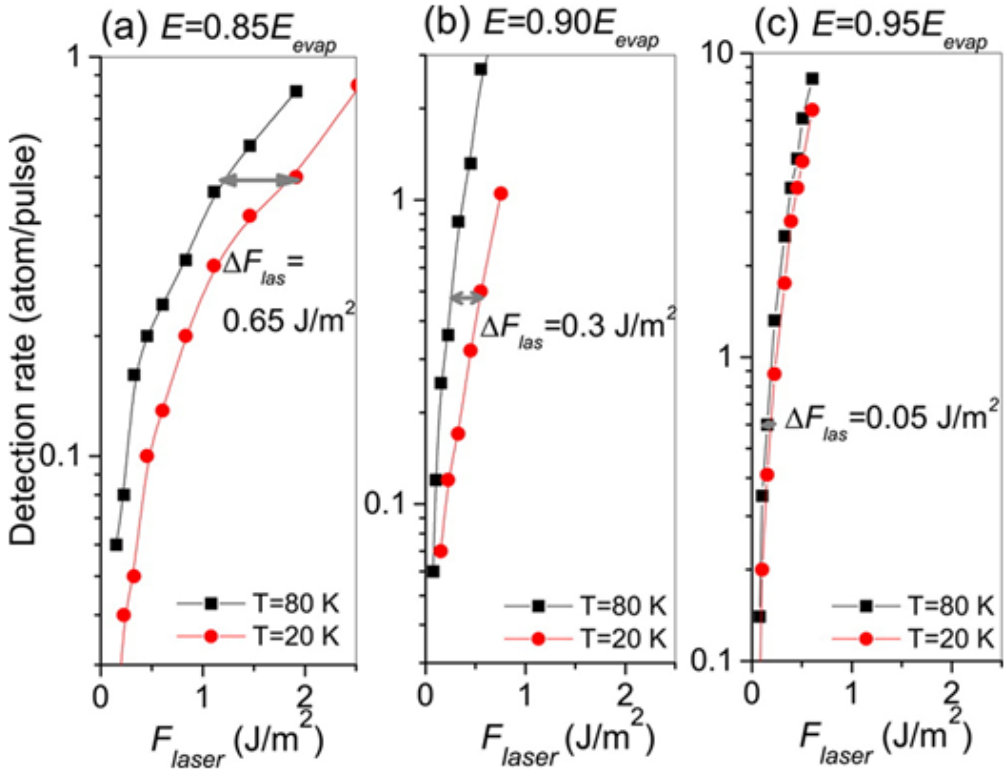

Figure 5.5 Number of detected ions per pulse as a function of the laser fluence at applied voltage of 9.3 kV (a), 10 kV (b), and 10.4 kV (c). Laser wavelength is 343 nm and pulse duration is 500 fs. Round red dots (connected by the red line to guide eyes) correspond to data collected for a base temperature of 20 K, and square black dots (connected by the black line to guide eyes) correspond to a base temperature of 80 K.

As reported in Figure 5.5, for a given value of the detection rate a higher laser fluence is required to evaporate the sample at lower temperature. Moreover, by increasing the dc field, this difference in the laser fluence decreases from $\Delta F_{\text{laser}} = 0.65$ J/m^2 at low dc field to $\Delta F_{\text{laser}} = 0.05$ J/m^2 at high field for a detection rate of 0.5 atom/pulse. According to the charge-state behavior of Mg ions during the experiment [126] we can deduce the value of the external field for the three analysis: $E = 0.85E_{\text{ev}} = 2.2$ V/Å at low field, $E = 0.90E_{\text{ev}} = 2.35$ V/Å at medium field, and $E = 0.95E_{\text{ev}} = 2.5$ V/Å at high field.

The value of ΔF_{laser} is the laser fluence necessary to increase the temperature of the sample from 20 to 80 K

$$\int_{20}^{80} C_{\text{p}}\,(T)\mathrm{d}T = \alpha(1-\Gamma)\Delta F_{\text{laser}} \tag{53}$$

where the left-hand side describes the energy stored in the system due to the change of temperature. Taking into account the heat capacity C_p of MgO [127] and the measured fluence difference we get an estimate for the absorption $\alpha(1-\Gamma)$, where α is the absorption coefficient and Γ is the reflectivity of the sample for the three values of the dc field, as reported in the first line of Table 5.1.

Table 5.1 Experimental Values of the Absorption, the BandGap Shrinkage, the Effective Photon Energy, and the Theoretical Value of the Absorption for Three Values of the dc Field[a]

	$E = 0.85E_{evap}$	$E = 0.90E_{evap}$	$E = 0.95E_{evap}$
Exp. $\alpha(1-\Gamma) \times 10^5$ cm^{-1}	1.5	3.0	18.0
$\Delta\mathcal{E}_{gap}$(eV)	4.6	6.0	7.0
$\hbar\omega_{eff}$ (eV)	8.2	9.6	10.6
Theor. $\alpha(1-\Gamma) \times 10^5$ cm^{-1}	3.8	6.2	8.8

[a]Laser wavelength is 343 nm and pulse duration is 500 fs.

These values of absorption are extremely high and correspond to the ones typically observed for metals [128]. This cannot be explained by considering the optical properties of a MgO nanostructure in field-free case. The bulk MgO is transparent to the laser light used in our experiment: the linear absorption coefficient is only 0.4 cm^{-1} [128] at the given laser wavelength (343 nm) and the nonlinear three-photon absorption coefficient is negligible at the given laser intensity ($<10^9$ W/cm^2). The defects of MgO surface can absorb such light better [129]. However, the absorption of the last atomic layer does not increase the tip temperature at the surface sufficiently to observe the temperature-related changes reported experimentally.

The DFT calculation predicts field evaporation of the MgO cluster at a field $E_{ev} = 2.6$ V/Å. At the dc fields of the experimental analysis, the DFT calculation shows that the gap decreases from 4.6 down to 1.7 eV at low field and to 0.5 eV at high field, as reported in Figure 5.4a. This corresponds to a relative band gap shift of 60% at low field and 90% at high field (Figure 5.4b). For the bulk MgO band gap of 7.8 eV, this corresponds to an absolute band gap shrinkage $\Delta\mathcal{E}_{gap}$ reported in the second line of Table 5.1. The change of the absorption coefficient for a photon of energy ω due to the band

gap shrinkage can be estimated from the corresponding shift of the absorption spectrum of MgO: $\alpha(\hbar\omega + \Delta\mathcal{E}_{gap})$. The same is valid for the reflectivity value. Thus, for the given wavelength 343 nm ($\hbar\omega$ = 3.6 eV), we have to consider the absorption coefficient and the reflectivity of MgO at the photon energy of $\hbar\omega_{eff} = \hbar\omega + \Delta\mathcal{E}_{gap}$, reported in Table 5.1. Using the values of $\alpha(\omega)$ and $\Gamma(\omega)$ reported in Palik [128], the theoretical values of $\alpha(1-\Gamma)$ are calculated; they are within an order of magnitude to the ones obtained in our experiment, as reported in Table 5.1.

Moreover, the dependence of the absorption on the dc field can be experimentally proved, looking at the voltage necessary to obtain a given detection rate as a function of the laser fluence. For each value of the laser fluence, the dc voltage applied to the tip is adjusted to evaporate the tip at a detection rate of 0.5 atom/pulse.

As reported in Figure 5.6, the voltage dependence on the laser fluence is nonlinear. This is unexpected because, for dc field in the range of 80–95% of E_{ev}, the energy barrier Q_n in Eq. 50 is a linear function of the dc field [130]

$$Q_n = Q_0' \left(1 - \frac{E}{E_{ev}}\right) \tag{54}$$

with Q_0' a proportionality factor resulting from the linearization of $Q_n(E)$ with E. The field E at the tip surface is controlled by the applied voltage V_{dc} according to the relation

$$E = \frac{V_{dc}}{\beta r_{tip}} \tag{55}$$

where r_{tip} = (50 ± 5) nm is the tip apex radius of curvature and β is a dimensionless factor that varies with the exact geometry of the tip within the range of 2 to 8. From eqs 50-55, for a constant detection rate the voltage applied to the sample becomes a linear function of the laser fluence

$$\frac{V_{dc}}{V_{ev}} = 1 - \frac{\ln(\varphi) - \ln(q\nu\langle N\rangle\tau_{evap}}{Q_0'}(\gamma F_{laser} + T_0) \tag{56}$$

This linear behavior was already reported on metals [131]. In the case of MgO, however, this dependence is not linear, and for high laser intensity the laser contribution to the evaporation saturates. As discussed before, this saturation is related to the decrease of the dc voltage. At lower voltage (and thus field), the band gap shrinkage and thus the absorption will be lower. Therefore, to evaporate the sample a much higher intensity is required.

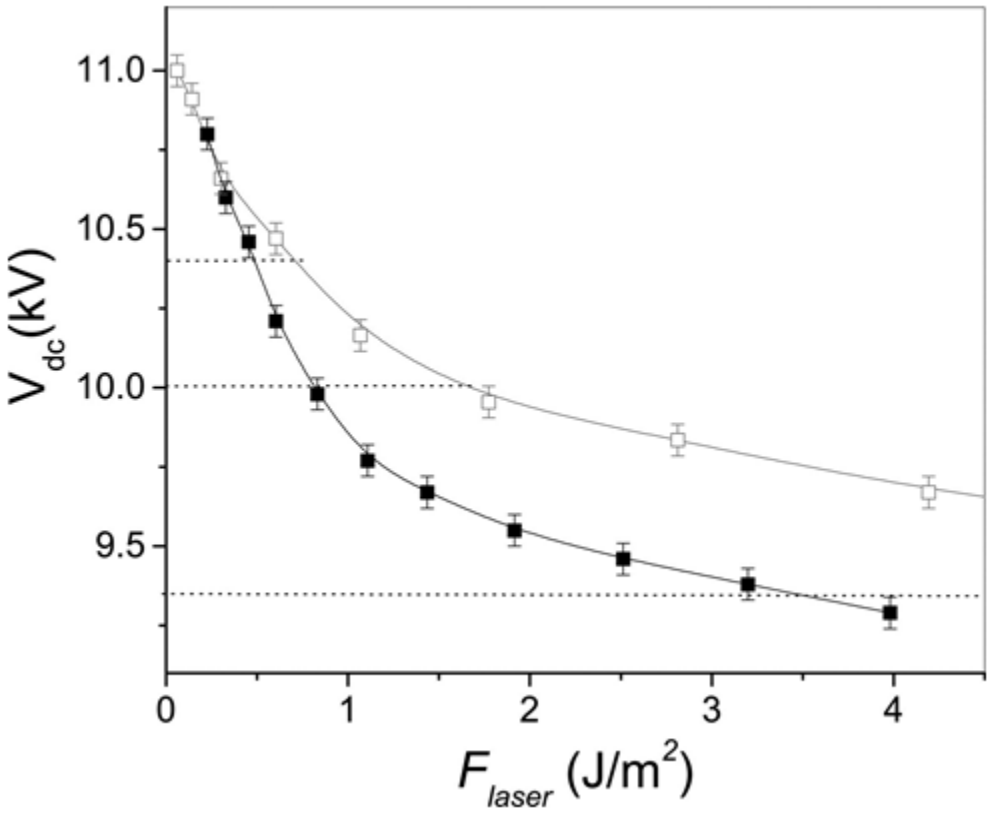

Figure 5.6 The dc voltage as a function of the laser fluence at a detection rate of 0.5 atom/pulse for a MgO tip. Full squares (connected by the black line to guide eyes) correspond to data collected using a UV laser (wavelength of 343 nm), open squares (connected by the gray line to guide eyes) using a Green laser (wavelength 515 nm). Dashed lines indicate the values of the voltage corresponding to the field values of (2.5, 2.35, 2.2 V/Å) from the higher to the lower. The laser pulse duration is 500 fs for both wavelengths.

The change in the laser wavelength from UV (343 nm) to green (515 nm) does not affect the behavior of the dc voltage as a function of the laser fluence, as shown in Figure 5.6. At dc field higher than 0.95 E_{ev} (V_{dc} > 10.4 kV), laser light is absorbed with the same

efficiency at both wavelengths because the band gap shrinkage is so strong that the surface behaves like a metal.

However, at lower field values the laser fluence required to obtain a fixed detection rate is now higher for Green laser. We indicate in Figure 5.6 with dashed lines the values of the voltage corresponding to the three values of the field considered before (2.5, 2.35, 2.2 V/Å). For each dc field value, we report in Table 5.2 the ratio of the laser fluence used during green and UV analysis. Moreover, as explained before, we calculate the theoretical value of the absorption at two laser wavelengths, considering the band gap shrinkage, reported in Figure 5.4. Comparing the experimental values of the ratio of the laser fluences with the ratio of the calculated values of the absorption, we can note a good agreement between experimental and theoretical results. Note that at a dc field of 0.85 E_{ev} using green laser, the evaporation is not reported experimentally, as predicted by the extremely low value of the calculated absorption.

Table 5.2 Experimental Value of the Ratio of UV and Green Laser Fluences and the Ratio of the Theoretical Values of the Absorption Calculated for UV and Green Light for Three Values of the Dc Field[a]

	$E = 0.85E_{evap}$	$E = 0.90E_{evap}$	$E = 0.95E_{evap}$
$F_{laser}^{Green}/F_{laser}^{UV}$	>2.4	1.8	1.5
$\alpha(1-\Gamma)^{UV}/\alpha(1-\Gamma)^{Green}$	630	1.5	1.5

[a]Laser pulse duration is 500 fs.

In summary, we have performed the first experiments proving that high electrostatic fields of the order of 0.1 V/Å inside a dielectric nanostructure strongly enhance its laser absorption up to the value typical for metals ($\sim 10^5$ cm^{-1}), as was recently predicted theoretically [107], [108]and proved experimentally only for high optical fields [103], [104]. We have also performed a first-principle DFT calculation for atomic clusters of MgO crystal showing that a high dc field modifies the band structure of a dielectric nanostructure and in particular its band gap decreases significantly down to total band gap collapse, which is in very good agreement with experimental data.

Atom probe tomography (as well as field ion microscopy) has been shown to be a unique technique to study high-field phenomena. In practice, the high dc field penetrates inside the dielectric samples of APT or FIM, but it does not lead to its damage because the electric current inside the tip is controlled charge by charge.

The phenomenon of the band gap collapse and further metallization of dielectric nanostructures in high dc fields has important consequences on the performance of field-effect transistors and supercapacitors. It has to be taken into account as one of the reasons (besides Zener tunneling and avalanche ionization) of their breakdown. The high-field metal-like properties of dielectric nanotips also strongly influence the field ionization and field evaporation processes in FIM and APT of dielectrics. In APT of nonmetallic tips, two scenarios were proposed to explain these processes: thermal activation and field-assisted evaporation [54], [62]. In the former, laser energy is absorbed by the tip generating hot carriers that migrate to the apex of the tip due to the applied field. Here, the hot carriers relax their energy, heating the apex region sufficiently for evaporation to become efficient [54]. On the other hand, in the field-assisted scenario a high density of positive charges, generated by laser absorption, is accumulated at the surface due to drift in the field leading to field enhancement sufficient to field-evaporate ions [62]. In both models, high dc field inside the nanotip drives the free carriers generated by the laser to the surface. Our work shows that this hypothesis is wrong because the dc field is screened inside the dielectric nanotip. Moreover, the strong metal-like optical absorption (even for sub-band gap photon energies) of the extreme surface finally explains the ultimate depth resolution of laser-assisted atom probe tomography achieved for nonconductive materials and therefore the exceptional analytical performances at an atomic scale of this technique [50], [52], [58].

CHAPTER 6 The mystery of missing species in Atom Probe Tomography of composite materials

This chapter has been published in Applied Physics Letters (vol. 107, pp. 062105–4, August 2015) as an article with the same title [132]. The authors are Markus Karahka, Yu Xia, and Hans Jürgen Kreuzer. Markus Karahka's contribution to this work consists of 80 % of the calculations and drafting 40% of the manuscript. Permission to use this work has been granted by the editor of Applied Physics Letters, a copy of the permission letter is attached to this thesis.

Abstract

There is a serious problem in Atom Probe Tomography of composite materials such as oxides that, even from stoichiometric samples, one observes non-stoichiometric ion yields. We present a quantitative model that explains the non-stoichiometry allowing a fit to experimental data of ion yields as a function of applied field to extract activation barriers and prefactors and compare with density functional theory. We also show that for oxides the missing oxygen is thermally desorbed as neutral O_2, either directly or associatively. Finally we suggest methods to improve the experimental setup.

The mystery of missing species in Atom Probe Tomography of composite materials

The atom probe, developed by Müller et al in 1968 [7], allows for the identification of the atomic composition of micro- and nano-specimens, see section 1.2. Although originally developed for metallic tips and used extensively for the study of the atomic composition of steels and other alloys it has also been adapted for the study of semiconductors and more recently for insulators through the assistance of ultrafast laser pulses. A number of outstanding issues have recently been resolved for APT of insulators and semiconductors including the discovery that at high fields the bandgap in semiconductors and insulators goes to zero leading to their metallization [10], [95].

A very interesting puzzle, however, remains unsolved, namely that even in stoichiometric samples of oxides, as an example, one observes non-stoichiometric ion yields, namely that there are missing oxygen ions depending on the field strength and on the oxide itself with e.g. different behavior for MgO and ZnO as examples. Similarly, for AlN and GaN the nitrogen yields are always less [98], [133], and in alkali halides there are less halide ions [134]. This is a serious problem as it precludes a proper compositional analysis of oxides and other insulators and semiconductors by APT. In this chapter we will give a quantitative model that explains the non-stoichiometry and show where the missing oxygen goes. The reader may refer to Mancini et al [98] for other models. Our picture will also suggest methods to improve the experimental setup.

To simplify matters we write the ion yield per surface site in the Arrhenius parametrization

$$Y = \nu \exp[-\Delta V / k_{\mathrm{B}} T] \tag{57}$$

We have shown elsewhere that the activation barrier is well approximated by [135]

$$\Delta V = V_0 (1 - E/E_{\mathrm{ev}})^2 \tag{58}$$

where V_0 is the binding energy of the atom to be removed and E_{ev} is the maximum evaporation field where the barrier ΔV disappears. The prefactor $\nu=\nu(E)$ is a function of the field strength and temperature. The prefactor also contains a kinetic coefficient (such as the sticking coefficient in thermal desorption) which accounts for the ionization process whether it is by tunneling or by laser excitation. We mention that the binding energy and the evaporation field strength are functions of the binding sites, being weaker for single atoms on flat surfaces and on corners and edges where local field enhancement occurs [1], [27], [28], [85].

We define the relative metal ion yield

$$f_M = \frac{Y_M}{Y_M + Y_O} \tag{59}$$

Thus the ratio of metal to oxygen yield is given by

$$R = \frac{f_M}{f_O} = \frac{Y_M}{Y_O} = \frac{\nu_M}{\nu_O} \exp\left(- \frac{V_M\left(1 - E/E_{ev}^{(M)}\right)^2 - V_O\left(1 - E/E_{ev}^{(O)}\right)^2}{k_B T} \right) \tag{60}$$

With $f_M + f_O = 1$ we have $f_M = R / (1+R)$. We look at two situations, namely (1) that at the evaporation field the ion yield is stoichiometric as in ZnO but not at lower fields, and (2) at the highest fields the ion yield is not stoichiometric like for MgO.

To simplify the model further we assume that the evaporation fields for the metal and oxygen components are equal. This is not the case for most oxides and needs further discussion below where we show explicitly that for instance for MgO not only are the fields for Mg and O different but even for different geometrical sites. We then imply that, for the ion yield to be stoichiometric at the evaporation field, we need $\nu_M(E_{ev}) = \nu_O(E_{ev})$ and Eq. 60 leads to

$$f_M = \left\{ 1 + \exp\left(\frac{(V_M - V_O)(1 - E/E_{ev})^2}{k_B T} \right) \right\}^{-1} \tag{61}$$

so that for $V_M < V_O$ the metal ion fraction is larger than that of oxygen , and v.v. As an example we know from DFT calculations that for both ZnO and MgO the metal atoms are weaker bound than oxygen, see Chapters 3 and 4 [85]. And for both materials the metal fractions are larger. The important point here is that even for this simple model the ion yields are only stoichiometric at the highest fields but not at smaller fields.

We next look at situations where even at the evaporation fields there is no stoichiometry in the ion yields, i.e. the ratio $\tilde{R}$ $(E = E_{ev}) = Y_M / Y_O = \nu_M / \nu_O \neq 1$, and the metal fraction becomes

$$f_M = \left\{1 + \tilde{R}^{-1}\exp\left(\frac{(V_M - V_O)(1 - E/E_{ev})^2}{k_B T}\right)\right\}^{-1} \quad (62)$$

To have the metal fraction larger than the oxygen fraction we need $\tilde{R}$ ($E = E_{ev}$) > 1. The various scenarios for $\tilde{R}$ =1, ≶ 1 are shown schematically in Figure 6.1.

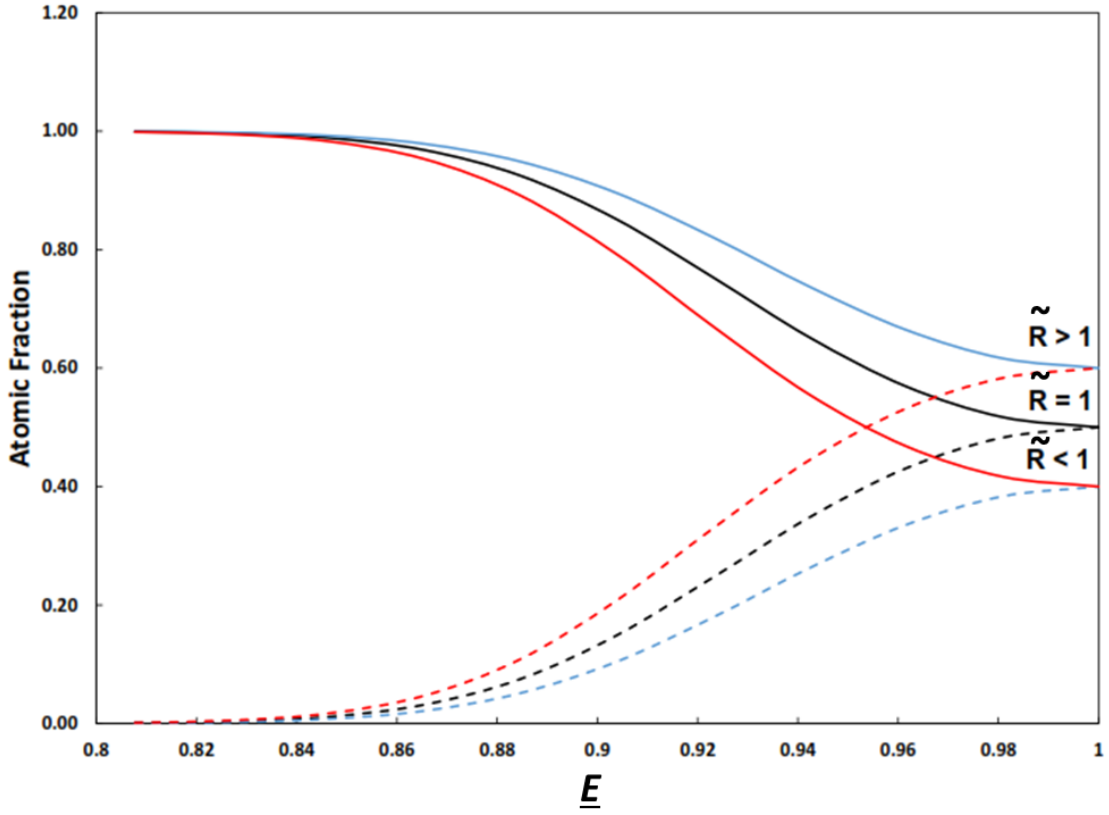

Figure 6.1 Schematic of ion fractions versus normalized field $\underline{E} = E/E_{ev}$, upper curves (solid lines) for metal ions and lower curves (dashed lines) for oxygen ions, for different values of $\tilde{R}$.

Next we apply our model to experimental data for MgO and ZnO [98]. MgO field evaporation has $\tilde{R}$ ($E = E_{ev}$) = 1.5. A fit of Eq. 62 is shown in Figure 6.2; it yields a binding energy difference (V_O-V_M) = 0.30 eV and an evaporation field strength of E_{ev} = 1.74 V/Å. The electronic structure calculations are based on DFT as implemented in the Gaussian 09 software package. We choose the B3LYP exchange-correlation functional, the 3-21G* basis set, and default convergence criteria [40]. Our calculations for a cubic 4×4×3 MgO cluster, based on density functional theory yielded values for the binding

energies of corner atoms of V_{Mg} = 10.62 eV and V_O = 10.88 eV in very good agreement with the fit to the experimental data. The evaporation field obtained from the DFT calculations in chapter 3 is 2.4 V/Å for a 3 layer cluster, [70], quite different from the experimental field of ~1.6 V/Å [98]. However, this discrepancy is irrelevant for the fit to the data because the fit is done with the normalized field $\underline{E} = E/E_{ev}$. We comment on the uncertainties of the experimental determination of evaporation field strengths below.

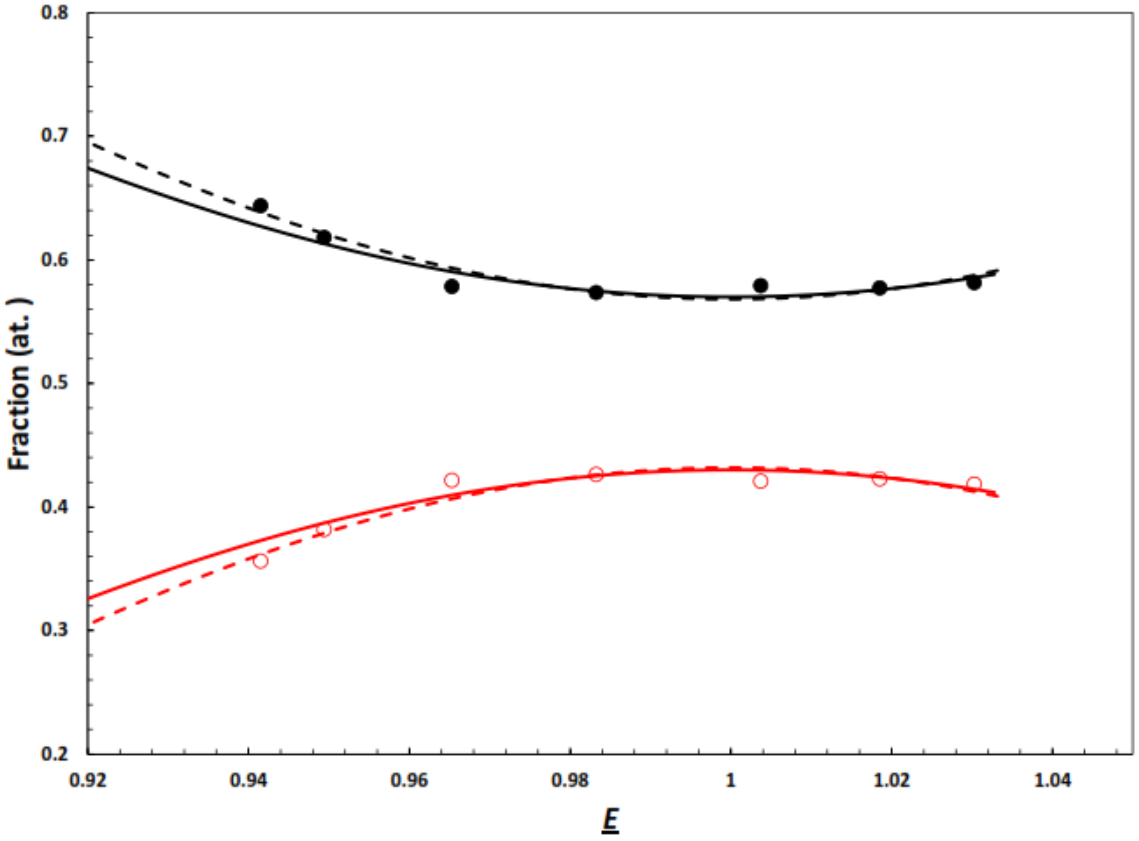

Figure 6.2 Atomic fractions of Mg (black curves) and O (red curves) from a MgO tip. Dashed lines from fitting Eq. 62 to the experimental data; solid curve calculated with DFT parameters. The experimental data points were taken from [98]. Those authors used a commercial APT instrument from CAMECA which records mass/charge ratios of species arriving in the detector which also counts them.

For ZnO measured with constant flux[98], Figure 6.3, we have $\tilde{R}$ ($E = E_{ev}$) = 1 and the analysis (V_O-V_M) = 0.25eV for a nanowire and 0.12eV for a bulk tip and E_{ev} = 2.27 V/Å and 2.50 V/Å, respectively.

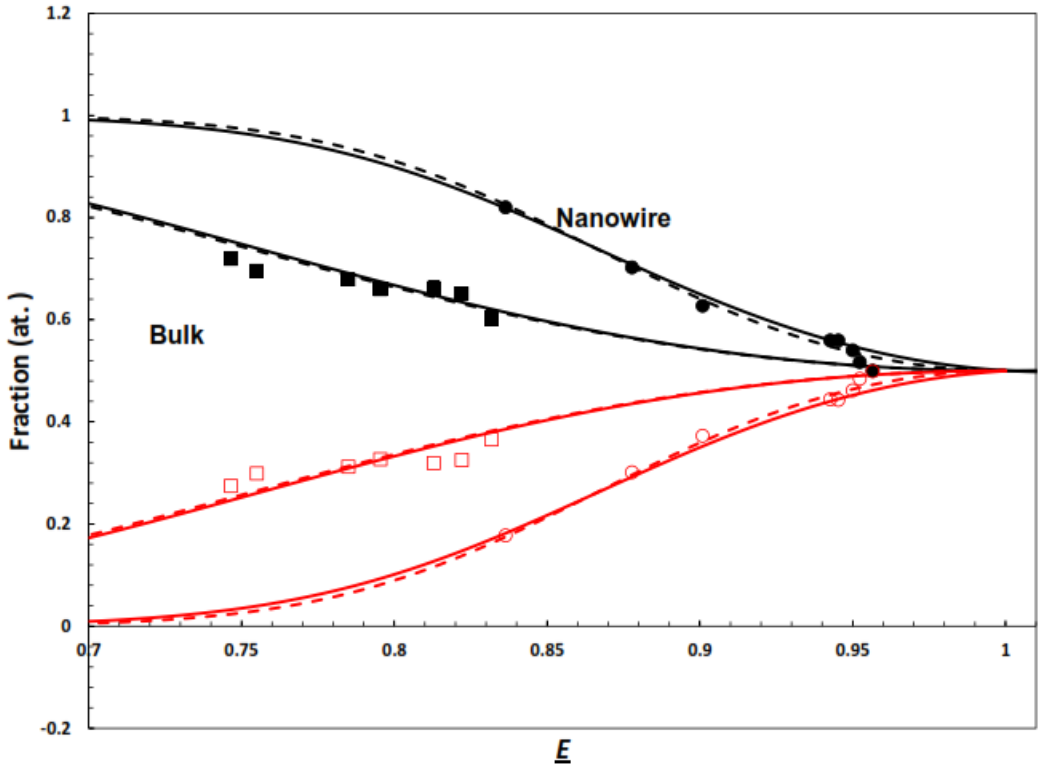

Figure 6.3 Atomic fractions of Zn (black curves) and O (red curves) from a ZnO tip. Dashed lines from fitting Eq. 61 to the experimental data; solid curve calculated with DFT parameters. The experimental data points were taken from [98]. Those authors used a commercial APT instrument from CAMECA which records mass/charge ratios of species arriving in the detector which also counts them.

We calculated evaporation fields and binding energies for a $Zn_{26}O_{26}$ wurtzite cluster as shown in Chapter 4 [86]. We note that obviously corner atoms are least bound, e.g. a corner Zn is bound by 6.42 eV and a corner O by 7.68 eV whereas those atoms in the interior of a surface plane are more strongly bound by an additional 2 eV. The evaporation field was determined by calculating the disappearance of the activation barrier as a function of field strength. As a result the evaporation field of the corner Zn and O is 2.6 V/Å and 3.2 V/Å, respectively. Neither of these would field evaporate at temperatures around 50K. We have therefore repeated the calculations for a pyramidal cluster with Zn and O on top finding binding energies of 1.24 eV and 1.45 eV which would be in agreement with the experimental result for a nanowire but not for bulk. The pyramid structure is appropriate for calculating the effects of low coordination on binding energies such as would be found on jagged edges, kinks, and O or Zn-rich surfaces versus the bulk crystal. Experiments with constant laser power for a nanowire [98] yield a

binding energy difference of 1eV which would agree with DFT calculations for corner O and Zn of the large $Zn_{26}O_{26}$cluster. This confirms our earlier observations in chapters 3-4 that atoms at different lattice sites have different binding energies and evaporation field strengths. More experiments are needed.

In laser-assisted APT of insulators and semiconductors there is no direct evidence that the laser energy is coupled into the phonon degrees of freedom thus heating up the tip above the base temperature. If this were the case the tip could be heated by up to 100K which would lead to significant thermal effects such as desorption of neutral species. However, it has recently been argued that the laser energy is used to create electron-hole pairs that aid in field ionization [95]. In this scenario any heating would be minimal. There is an additional uncertainty in APT, namely in the determination of the field at the tip. In APT of metals this can be determined quite accurately from the shape of the tip. However, the situation is almost unresolvable for insulators: They are deposited on a metal tip which is needed for a contact to apply the voltage. However, neither thickness nor morphology of these insulating layers are known to any accuracy. Thus values of local fields in experimental papers are not reliable and vary greatly for different groups.This is usually done based on the Kingham post-ionization model [126]. It turns out that the so-determined field variation from 1.9 to 2.2 V/Å in the ZnO experiments, as an example [136], is smaller by at least 10% than what one would naïvely expect from the variation of the applied DC voltage. Our DFT calculations in Chapter 4 [85], [86] also suggest that the evaporation field is about 2.5 V/Å. As to the use of the Kingham post-ionization model we want to make two cautionary comments: (1) APT of ZnO yields Zn^{2+} ions that are created instantly as the ion moves away, i.e. it is not a spatial sequence where first Zn^{+} is created that further away is post-ionized [85], [86]. So it is not surprising that a Kingham analysis for ZnO does not produce consistent results. (2) The Kingham model, originally developed for metals, is based on largely classical arguments without taking any account of quantum chemistry in high electrostatic fields: (i) The metal surface is treated using a jellium model so no account is taken of the surface density of states and the local environment at the surface is ignored. (ii) No account is taken of the observed crystallographically dependent variation in the proportions of various ion charge states.

(iii) Variations in the field strength due to different crystal faces and distance from the surface are ignored. (iv) The theory assumes initial evaporation is due to the image-hump model or the charge-exchange model. (v) All the approximations result in uncertainties of the order of at least 20% for the critical field strengths required for post-ionisation according to Kingham [126].

Because APT yields non-stoichiometric ion yields from oxides we need to find a second channel by which O is removed. There are two options: negative O ions can migrate down the surface of the tip and eventually desorb thermally after forming O_2. With atomic O accumulating at the tip, we have, in addition to surface diffusion, two possible desorption channels for its removal: (i) molecular oxygen forms on the surface; this seems to be the case for ZnO [85], or (ii) associative desorption, i.e. $2O_{ad} \rightarrow O_2^{(gas)}$ where two adsorbed O atoms need their surface binding energy $V_O(E)$ to break their surface bonds and gain the molecular binding energy or dissociation energy D_{O_2} in the gas phase.

The desorption rate constant (desorption rate per site) for an adsorbed molecule is [137]

$$r_{des}^{(mol)} = S^{(O_2)}(T)\frac{a_S}{\lambda_{th}^2}\frac{k_B T}{h}\frac{Z_{int}}{q_3 z_{int}}\exp\left[-V_{O_2}/k_B T\right] \quad (63)$$

Here a_s is the area of the adsorption site of one molecule on the surface, $\lambda_{th} = [h/(2\pi m_{O_2} k_B T)^{1/2}$ is the thermal wavelength of the molecule, Z_{int} and z_{int} are the partition functions for the internal vibration and rotations of the molecule in the gas phase and adsorbed, respectively, $S^{(O_2)}(T)$ is the sticking coefficient of O_2, and q_3 is the partition function of the translational motion of the molecule parallel and perpendicular to the surface. We have done DFT calculations and found that O_2 adsorbs on a ZnO wurtzite surface in the absence of a field with a binding energy of about 1.2 eV in agreement with earlier results [138]. Of more relevance for the present discussion is the fact that this binding energy is reduced to about 0.2 eV in fields above 2 V/Å. A Mulliken population analysis [44] shows that the adsorbed molecule is neutral; in addition, its bond length and internal vibration is very similar to that in the gas phase, and the vibrational frequencies relative to the surface, needed for the calculation of q_3, are "normal", i.e. of the order of

10^{12} s^{-1}. We then find that the desorption rate at temperatures around 80K is of the order of 10^{2} s^{-1}. We can thus conclude that for fields above 2 V/Å molecular oxygen forms on the surface but desorbs rapidly at temperatures above 80K as a neutral species and is thus not detected in APT.

Next we consider associative thermal desorption for which the desorption rate is given by [137]

$$r_{des}^{(ass)} = 2S^{(O)}(T)\frac{a_S}{\lambda_{th}^2}\frac{k_B T}{h}\frac{Z_{int}}{q_3^2}\exp\left[-\left(2V_O - D_{O_2}\right)/k_B\,T\right] \tag{64}$$

This rate constant differs drastically from the molecular rate constant in several factors: (i) There is an overall factor 2 to account for the fact that two adsorption sites are emptied to form a gas phase molecule, (ii) the translational partition function appears twice, and (iii) the activation energy involves the atomic surface binding energy V_O and the gas phase dissociation energy D_{O_2}. In a stoichiometric ZnO surface both Zn and O are bound very strongly. However, in an O-rich surface left by the field desorption of Zn, we find from DFT calculations that at corners or at the apex of a small pyramid the binding is reduced to less than 1eV so that the desorption energy $2V_O$-D_{O_2} is less than zero because the dissociation energy of molecular oxygen is 5.1eV. This is not yet the end of the story because for two atoms to desorb associatively they must first come together on the surface by diffusion. For oxygen atoms on the surface of ZnO this is possible because from DFT calculations we know that at 2 V/Å the diffusion or hopping barrier is reduced to 0.2 eV. Thus at temperatures around 80K two oxygens on the surface are removed instantly through associative desorption as neutral O_2, again avoiding detection in APT.

Trying to demystify the issue of missing oxygen in APT ion yields of oxides we have shown:

(1) Metal atoms in an oxide are typically less bound than O and thus can be field evaporated at lower fields.

(2) Although some O can be field evaporated e.g. as O_2^+ the surface will be enriched with O which however, is not bound too strongly at high fields and can easily migrate over the

surface. Thus thermal desorption of preexisting neutral molecules or associatively from atomic O will remove the excess O. However, these species, being neutral, will not be detected as ions.
(3) If metal atoms field-desorb preferentially, one would obtain an oxygen-rich surface which could be cleared by a burst of oxygen. Such bursts have not been reported and if they were to take place a layer-by-layer analysis would be impractical.
(4) Increasing the field above the evaporation field strength of the metal component is usually not an option to obtain stoichiometry as the higher fields will "melt" the surface structure invalidating the claim that APT can obtain site-specific atomic maps layer-by-layer.

The question then remains on how to make APT work stoichiometrically for oxides. We have several suggestions:
(a) For some, but not all oxides there seems to be an optimal field where stoichiometry can be maintained, e.g. the maximum field for the ZnO-like system depicted in Figure 6.3, or the cross-over field in Figure 6.1.
(b) Block's pulse mode [139] will clean the surface during the high field pulses which would come off as ions although no longer site specific.
(c) As our results in this chapter and in previous publications have made amply clear DFT calculations can provide guidelines on optimal fields and also on the binding characteristics that ultimately dictate which ions come off and which desorb thermally as neutrals. Ideally a comprehensive catalogue of relevant atomic data would be generated and made available.
These remedial methods may however distort the surface themselves so some serious testing is required.

As a final statement we would like to repeat the obvious: Although we have dealt exclusively with oxides in this chapter our approach also explains the absence of stoichiometry in nitrides (GaN, AlN etc.) and in alkali halides.

CHAPTER 7 Field-induced polymerization of water

The contents of this chapter have been published in two journals: Physical Chemistry Chemical Physics (vol. 13, no. 23, pp. 11027–11033, May 2011) as an article with the title "Water whiskers in high electric fields" [140] and Biointerphases (vol. 8, no. 1, p. 13, Jun. 2013) as an article with the title "Charge transport along proton wires" [141]. The authors are Markus Karahka and Hans Jürgen Kreuzer. Markus Karahka's contribution to this work consists of all calculations and drafting 60% of the manuscripts. Permission to use this work has been granted by the editors of Physical Chemistry Chemical Physics and Biointerphases.

7.1 Water Whiskers

Water is no doubt the most important molecule for life and its structure and dynamics have thus been explored extensively in natural selection and in the pursuit of intellectual curiosity. An unexpected discovery was made in the late 80s and early 90s by Block and his colleagues[142]–[146] that exposing Ni, Ag and W field emitter tips in the field ion mode to water vapor lead to the adsorption of a water layer that desorbed under high fields and in photodesorption as protonated water clusters as demonstrated in the mass spectrum in Figure 7.1. Such clusters had been observed earlier by Beckey[147], [148], Schmidt[149], and Tsong and Liou[150]. It was speculated on the basis of a simple model by Anway[151] that in high electric fields water aggregates become linear and the formation of long chains of water is triggered. Outside the small community of the field emission society this work remained unnoticed. So it is no surprise that recent papers[152]–[154] do not discuss all this information as we will detail below. In passing we should also note that Block and associates demonstrated the polymerization of sulfur chains, avoiding the closure of the sulfur ring at 8 atoms and producing linear chains of up to twelve sulfur atoms[2], [155].

The inference of water whiskers was originally made on the basis of a simple argument[143], [151]: the water molecule has a dipole moment μ_{water}= 1.85 Debye. Thus

aligning a water molecule in an electric field E at an angle γ leads to an energy gain of $\mu_{water}E\cos\gamma$. To maintain one hydrogen bridge bond between two successive water molecules in a linear array the dipoles are at an angle relative to the axis of the linear array. If the latter is also the direction of the electric field we need $\gamma = 75^{0}$. Thus this alignment results in an energy gain of about 0.26 eV per molecule in a field of 1 V/Å. This is larger than a hydrogen bridge bond which is typically 0.05-0.25 eV. In the surface layer of a water film adsorbed on a metal the coordination is typically between one and three. Thus, the formation of chain molecules of water or water whiskers in a field of 1 V/Å is plausible.

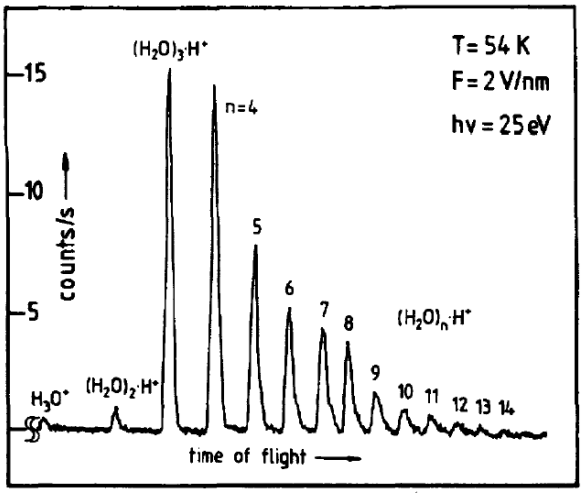

Figure 7.1 Time-of-flight spectrum of water clusters from a water-covered silver field emitter, obtained by photon-stimulated field desorption [145].

We now come to a review of recent theoretical work on small water clusters in a uniform electric field. James and Wales[153] used classical rigid-body models of the TIPnP family of effective pair potentials to study the energy landscape for an investigation of stability and diffusion pathways. Similar calculations were done earlier by Dykstra for the water trimer[156]. Such models ignore all effects of field-induced chemistry which are of utmost importance at fields of the order of V/Å. Because classical models are based on fixed charges within the molecules they cannot account for the fact that in strong fields there is a substantial re-distribution of charges within a water molecule as well as between molecules in a whisker, as an example. Thus to retain the utility of classical models one needs to re-fit the charges as a function of the field, of course again

based on ab initio calculations. A detailed discussion of this point, relevant for water clusters as well, has been presented for the behavior of a more complicated molecule, poly(ethylene glycol) [157], [158]: there is a significant modification of the local electronic structure including a large charge transfer down the electric field that cannot be described by polarization alone. Such effects are accounted for in quantum mechanical calculations. This was done for water clusters by Choi et al [152] who calculated the structure of water clusters of up to 6 molecules and found that some alignment into a linear molecule occurred. A follow-up paper [154] extended the calculations to clusters of up to 8 molecules finding similar results. Unfortunately the authors of both papers do not refer to the experimental facts. As a result they also missed a few important details that we will address in this work: (1) What are the lower and upper threshold fields for water whiskers of different lengths? (2) How valid is the dipole alignment argument presented above?
(3) What is the effect of protonation? In field-induced desorption of water from a field emitter the clusters are protonated. How does the presence of a charge at one end of the cluster affect its stability and how does a protonated cluster change into a hydration shell around the ion as it enters a field-free region?
(4) How does the field-aligned whisker re-adjust when it is taken out of the high field region?
(5) What are the electronic mechanisms such as charge transfer that result in the formation of water whiskers, and how does the whisker disintegrate at the highest fields?

Once we have the answers to these questions we will also address the question whether a water whisker in a high enough field will become conducting. This is motivated by the recent discovery that polythiophene, which is a semiconductor with a gap of about 2.5 eV, closes the gap and becomes conducting in fields around 1.5 V/Å [83], [159].

Because field emitter tips have typical radii of curvature of 100Å the field produced by a voltage drop to a counter-electrode is up to several V/Å, large enough to field-desorb surface atoms as ions. Also, because of the large curvature these fields decay within a few 100Å by several orders of magnitude so that the ions traverse an almost field-free

region on their way to the detector. It should also be pointed out that there is a significant field enhancement at step sites and above individual metal atoms on flat facets of the field-emitter tip by as much as a factor of three [27], [28].

As for the theoretical approach to field-induced chemistry we will base our calculations on density functional theory with a large basis set as used in previous studies of water. As shown elsewhere [160], a reliable choice for an exchange/correlation potential and basis set for water is B3LYP/6-311++G**. In this work we will only deal with isolated water clusters not in contact with a surface. The bottom oxygen is held fixed to avoid the structure drifting with the applied field. For each cluster size and external field strength, one starts from an initial geometry guess for which Gaussian calculates the electronic structure. This in turn is used to calculate internal forces on the atoms as a basis for the next geometry guess. Depending on the initial geometry one may wind up in a local minimum of the geometrical optimization which defines a conformer of higher energy than the absolute minimum of the ground state, see section 1.6 for details of geometry optimizations.

In the next subsection we start with a water trimer in a field and identify the molecular mechanism for the formation of a "linear" conformation followed by a look at how the cluster disintegrates in a field above 2 V/Å. Then we look at larger clusters, octamers and decamers and follow their field fragmentation. At the end of this chapter we will give answers to the questions asked above and add some speculative ideas.

7.1.1 Trimer

In the absence of an electric field the lowest energy conformation of a trimer is a triangle as depicted in the first column of Figure 7.2. Note that this molecule is not planar and thus not rotationally symmetric. This is well demonstrated by the distribution of the HOMO in contrast to the LUMO which looks almost symmetric. As we apply a "small" field up to 0.1 V/Å (pointing up according to the arrows in Figure 7.2) we can reach two local minima depending on the initial geometry we choose. If we start from the zero field

configuration we wind up in a similar, i.e. almost planar configuration; a side view is given in the second column in Figure 7.2. However, if we start the calculation from a strictly linear configuration the self-consistent end result of the geometry optimization is a stretched molecule of almost the same energy, more precisely within 1 meV, similar to the third column in Figure 7.2. This configuration persists up to a field of 0.5 V/Å. What is apparent in this conformation is a significant shift opposite the applied electric field direction for the HOMO and up for the LUMO, see the third column in Figure 7.2, as indicated graphically by enlarged molecular orbitals.

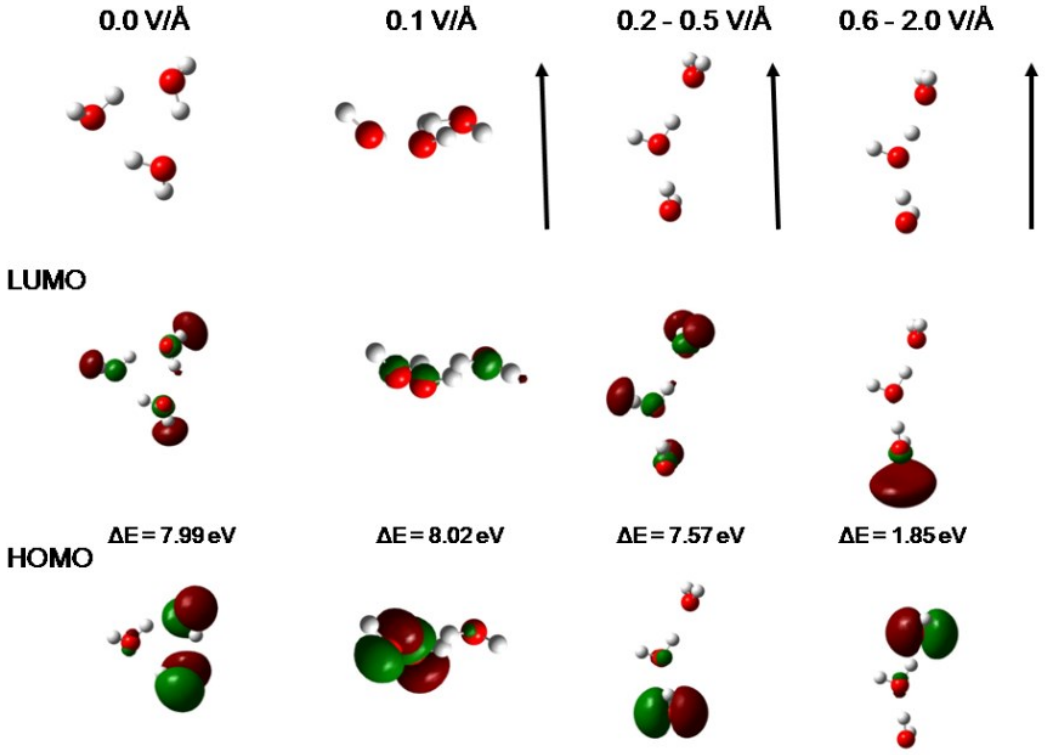

Figure 7.2 A water trimer at various field strengths with the field pointing parallel to the arrows. The O (H) is coloured red (white). Also shown are the orbitals of the HOMO and LUMO and their energy difference. The color coding (red-green) indicates two different phases of the molecular wave functions [140].

For fields above 0.5 V/Å the trimer stretches more and the HOMO and LUMO enhancements above reverses direction as evidenced by the difference between the third and fourth column in Figure 7.2. Although puzzling at first, the explanation is simple: for

"low" fields (< 0.6 V/Å) the HOMO-LUMO gap is quite large, i.e. around 8 eV. All that a low field does is orient the molecular dipoles in the field direction. This can be interpreted as simple polarization. However, for high fields the MO energy level at the top of the trimer is raised relative to the MO at the bottom and becomes the HOMO, while an electron will want to move against the applied field to the bottom of the trimer and fill the LUMO. The gap closes quickly; this leads to field-induced re-hybridization as discussed for the AB molecule in Chapter 2. The field dependence of the HOMO-LUMO gap is plotted in Figure 7.3 as the top curve which also gives the gap in the pseudo-planar configuration (crosses at low fields). Of note is the fact that the gap gets larger for fields up to 0.5 V/Å after which it starts to close. If all the field does is raise the HOMO relative to the LUMO one would expect the slope to be given by $-qEd$ where d is the distance between the centers of mass of the HOMO and LUMO, *i.e.* $d \approx 5$ Å. In fact it is somewhat smaller due to the fact that rehybridization also takes place. Also plotted is the dipole moment $\mu(\boldsymbol{E})$ which also rises quickly for weak fields up to 0.5 V/Å after which it increases almost linearly with field. The initial rise from E=0.1 to 0.2 V/Å is the result of the individual dipole moments on the three water molecules aligning with the field direction. The subsequent increase has two contributions: (a) In this field range (0.5-2.0 V/Å) the dipole moment of a single water molecule increases more or less linearly from 2.3 to 2.9 Debye with a polarizability of 1.2×10^{-40} Cm²/V. With 3 molecules in a trimer this accounts for a total of 8.7 Debye. (b) As the field increases there is a net negative charge transfer down the molecule which rises in this field range from 0.01e to 0.3e, or for the dipole moment itself an additional contribution of about 1.5 Debye leaving 1.8 Debye unaccounted for. As mentioned in section 1.1 the induced dipole moment is linear if the field isn't too strong, but as the applied field is increased past 1.5 V/Å the dipole moment increases nonlinearly as seen in Figure 7.3. This could account for the missing 1.8 Debye.

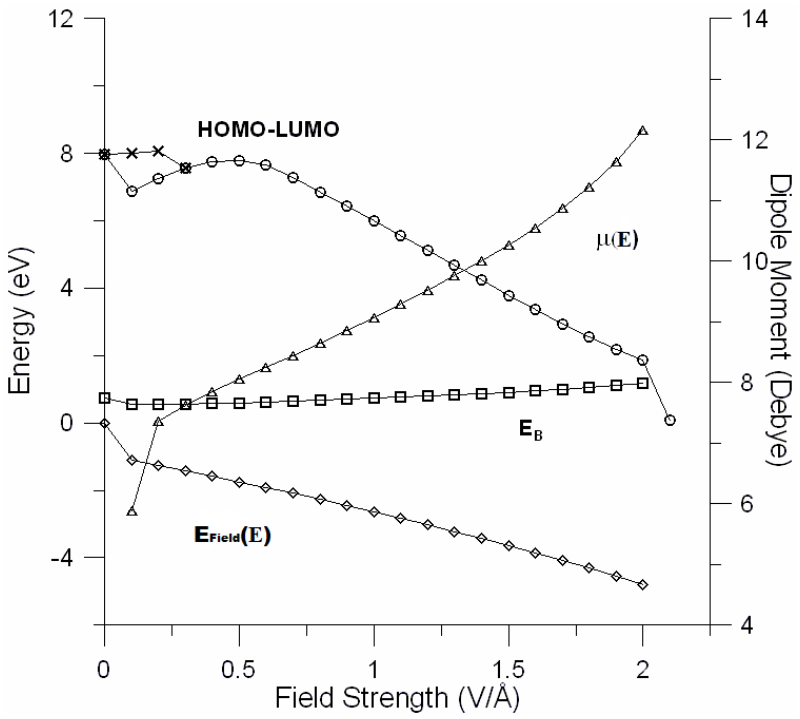

Figure 7.3 Various energies (the HOMO-LUMO difference, the field energy $E_{Field}(\boldsymbol{E})$, and the binding energy E_B, see text), and the dipole moment μ of the trimer as a function of field strength. The crosses in the HOMO-LUMO difference at low fields refer to the planar configuration, and the open circles to the whisker [140].

Also plotted is the field energy $E_{Field}^{(3)}(\boldsymbol{E}) = E_{el}^{(3)}(\boldsymbol{E})-E_{el}^{(3)}(\boldsymbol{E}=0)$ which is the change in the electronic energy of the trimer as a function of field; it decreases almost linearly. Similarly, the binding energy per molecule $E_B^{(3)} = E_{el}^{(1)}-E_{el}^{(3)}(\boldsymbol{E})/3$ remains almost constant. For fields above 2 V/Å the stress on the whisker is too large and field-induced dissociation or fragmentation occurs associated with the complete closure of the HOMO-LUMO gap. This can be interpreted as an insulator-metal transition just prior to fragmentation.

To get a picture of the fragmentation process we show in Figure 7.4 the molecular configuration as a function of the number of iterations in the geometry-optimization procedure. It is surprising that already after 10 iterations a proton from the lowest water molecule has migrated to the top molecule to form a hydronium ion which, by step 40, has separated from the molecule with the remainder disintegrating as well after about 100 iterations.

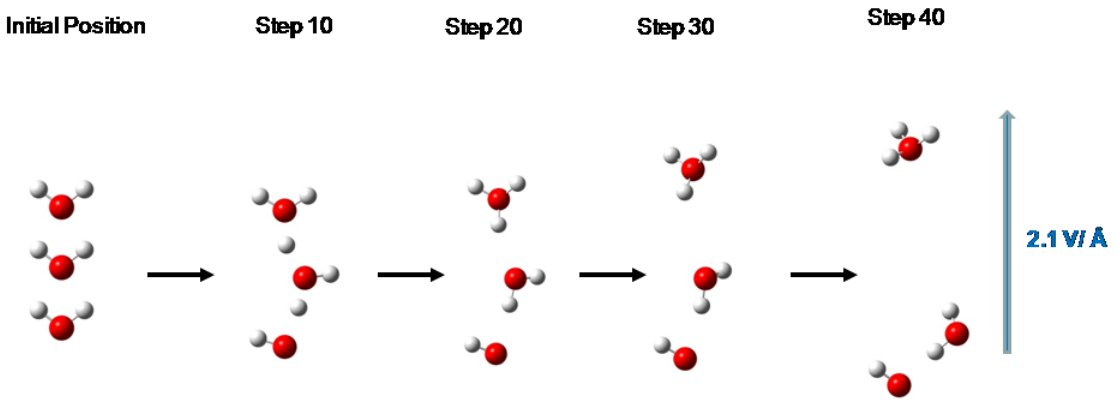

Figure 7.4 Disintegration of a trimer in a field of 2.1 V/Å. The step number refers to the geometry optimization procedure. The O (H) is coloured red (white) [140].

As a last feature for the trimer we begin with the linear configuration stabilized in a field of 0.3 V/Å which we then switch off to see how the trimer returns to its triangular shape in zero field. This is shown in Figure 7.5 as a function of the optimization steps in the iteration process; we recall that at each geometry Gaussian calculates the electronic energy self-consistently. Also plotted is the distance between the oxygen atoms on the two end water molecules. In panel (b) we re-plot the energy as a function of the O-O distance extended to smaller values to include the potential minimum and repulsion. We interpret the initial, almost linear decrease in the energy as the molecule re-arranges itself as the origin of a force which is given approximately by $f \approx \Delta E/\Delta d$ amounting to about 0.1 eV/Å. According to Newton's equation of motion a mass m will travel under a constant force f a distance Δd in a time $t = [2m\Delta d/f]^{1/2}$ which gives the time scale of re-arrangement from a linear to a triangular configuration of about picoseconds with an average velocity of roughly 100 m/s which is an order of magnitude less than the speed of sound in water, 1482 m/s at 293K. The kinetic energy gained in this re-arrangement will be dissipated into rotational and vibrational excitations. The calculated rotational temperatures of the trimer as a whole are around 0.3 K. In addition to the internal vibrational excitations of the individual water molecules (~ 2300 K, 5200 K, 5400 K) there are also lower vibrational excitations of the molecules against each other with

temperatures of the order of 270 K, 340 K, 500 K, and 1000 K. In contrast with experimental values of vibrational frequencies of 813 K, 2298 K, 2340 K, 5047 K, 5323 K for a water trimer [161]. Several of the calculated values are within 10% of experimental values.

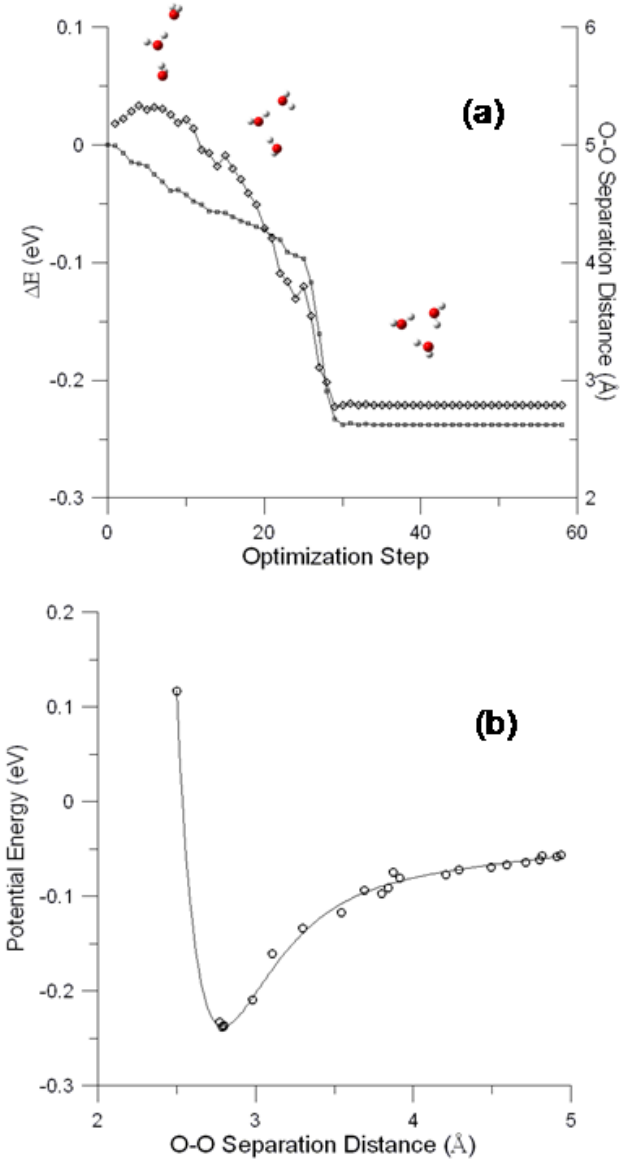

Figure 7.5 The linear trimer formed in a field of 0.3V/Å re-arranges itself into a triangular trimer after the field has been switched off. Panel (a): The circles (top curve) show the O-O separation distance between the top and bottom oxygens as a function of the optimization steps. The lower curve shows the change in energy as a function of the optimization steps. Panel (b): The potential energy seen by the re-arranging molecule as function of the O-O separation distance [140].

7.1.2 Octamer and Decamer

As we increase the number of water molecules in the cluster the minimum field needed to form a whisker remains about the same at 0.1 V/Å and the maximum field beyond which the whisker is unstable decreases. We therefore skip intermediate cluster sizes and go directly to octomers and decamers. The unprotonated species form compact clusters in zero field and remain stable whiskers up to fields 0.7 V/Å and 0.5 V/Å, respectively, see Figure 7.6.

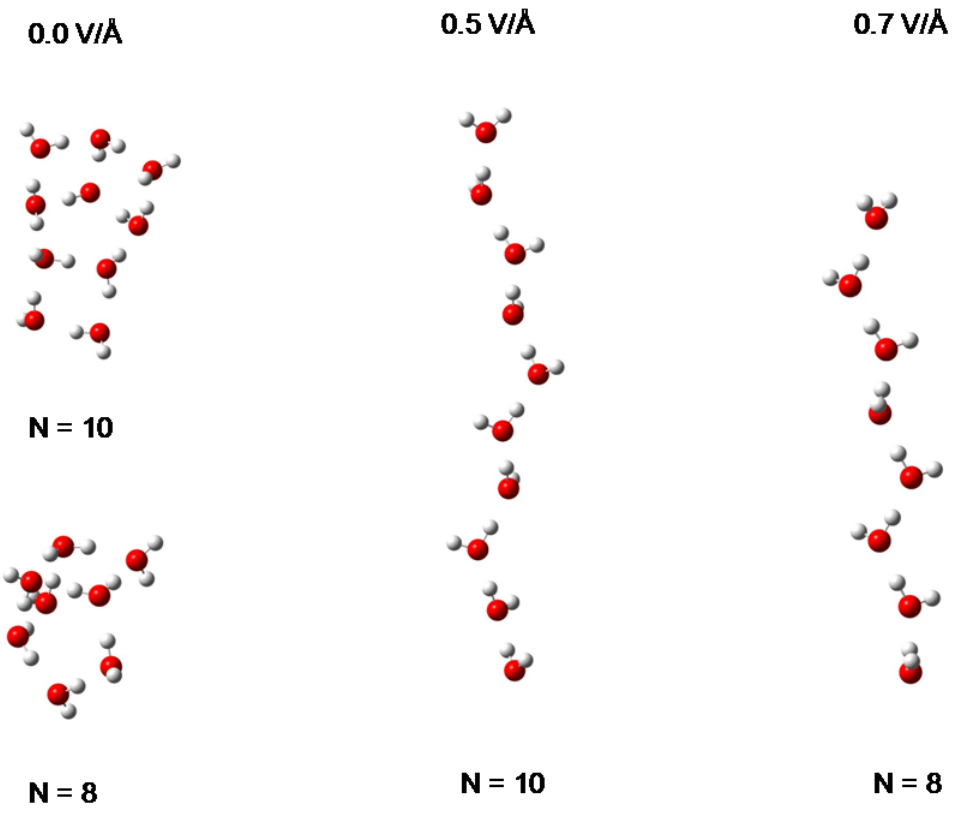

Figure 7.6 Octamer and Decamer as a function of field strength [140].

Beyond these fields dissociation sets in which we follow again as a function of the number of iterations in the geometry-optimization routine, see Figure 7.7. As a result smaller clusters, resulting from the dissociation of larger whiskers, become more abundant in the mass spectra as seen experimentally, see Figure 7.1.

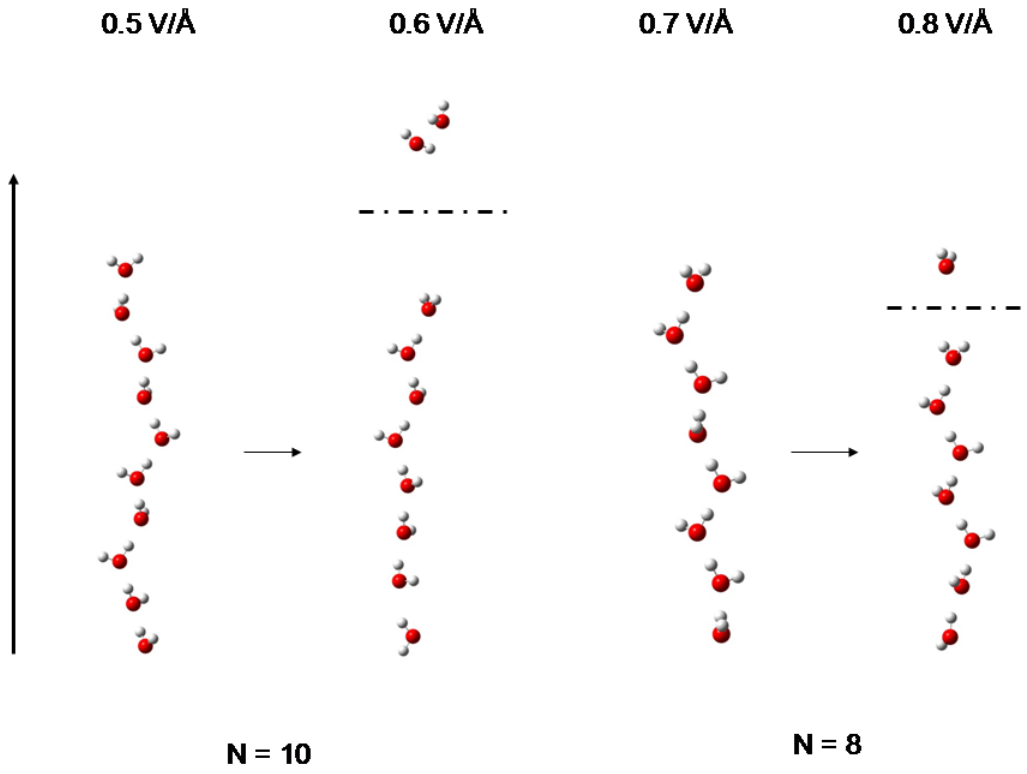

Figure 7.7 Successive field fragmentation of the decamer and Octamer [140].

The results of a stability analysis are shown in Figure 7.8 for the different size whiskers. The monomer number *n* is plotted as a function of the field strength before fragmentation i.e. the last stable whisker configuration.

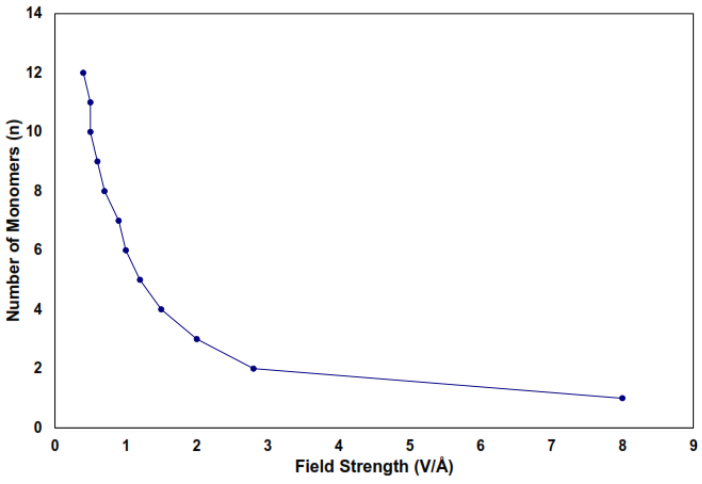

Figure 7.8 Water whisker stability diagram.

To avoid all possible misconceptions we stress again that we can show that water whiskers or the formation of chain molecules of water can be induced by strong electric fields of the order of volts per Angstrom but that such structures are unstable when taken out of the field. In this context it is intriguing to contemplate the role of electric fields in proton transfer along water whiskers (called proton wires in biology). With membrane potentials of the order of 80 mV and membrane thickness of 3 nm, the fields are at the lower end considered here. However, they are strong enough to allow protonated whisker formation as a higher energy state. In membrane channels they are of course further stabilized by the constraining proteins [162], [163]. This is explored further in the next section on proton wires.

7.2 Proton Wires

In 1978 Nagle and Morowitz [164] suggested that linear water structures in membrane channels may act as carriers for proton transfer through the membrane wall. They also coined the term proton wires for these water whiskers. These proton wires extend through membrane channels and connect the enzyme active site with the liquid phase outside the cell with enzyme functional groups inside the cell. We list a few examples. In the transmembrane channel formed by Gramicidin A proton wires are found within its helical structure [165], [166]. Proton wires are also found or suspected in bacteriorhodopsin [167]–[170], photosynthetic centers [171], in enzymes [172] and even in viruses [173]. In most of these systems amino acid residues (His, Glu, Asp, Ser) act as proton donors and acceptors at the respective ends of the water whisker. A comprehensive review, both experimental and theoretical, was given by Cukierman [162].

As an early model of charge transfer in proton wires Nagle and Morowitz [164] adapted classical ideas by Grotthuss who, as early as 1806, suggested that in diffusion of protons in bulk water an 'excess' proton propagates through the hydrogen-bonded network by

repeated cleavage and re-formation of hydrogen bonds [174]. Theoretical efforts since then have focused mainly on mixed classical/quantum methods such as a polarization model with discretized Feynman path integral-molecular dynamics (FPI-MD) as used by Pomès and Roux [175]–[177], an ab-initio FPI Car-Parrinello MD used by Klein *et al* [178], a Born-Oppenheimer local-spin-density MD used by Sadeghi and Cheng [179], a multiconfigurational MD with quantum transitions used by Hammes-Schiffer *et al* [180]–[182], a MD with a multi-state empirical valence band (EVB) model used by Voth *et al* [183], a quantum/molecular mechanical method used by Nemukhin *et al* [184], a "real time" MD used by de Groot and Grubmüller [185], and an EVB model with Langevin dynamics used by Warshel *et al* [186]. For the most part they are concerned with the stabilization of the proton wires by the walls of the membrane channel and also on simple kinetic models to describe the proton hopping process. Several groups looked at the effects of weak electrostatic fields [163], [180], [182], [186]. Various groups have also employed fully quantum mechanical approaches such as the multiconfiguration time-dependent Hartree method used by Vendrell and Meyer [187], and density functional theory [188]–[191].

We will base our calculations on density functional theory with a large basis set as used in the previous section on water whiskers and appropriate gradient-corrected exchange-correlation functionals as implemented in the GAUSSIAN'09 software package [40]. As shown elsewhere [160] a reliable choice for an exchange/correlation potential and basis set for water is B3LYP/6-311++G**.

7.2.1 Protonated Tetramer

The existence of stable water whiskers was also postulated in the 1980's in field ion microscopy [142], [143]. The evidence was as follows: exposing a field emission tip to water vapor with an electric field of the order of volts per angstroms applied and then evaporating the water film on the tip by laser pulses or higher electric field pulses resulted in mass spectra of protonated water clusters $(H_2O)_nH^+$ with up to a dozen water molecules with n=2-4 being most abundant. Field desorption of an adsorbed molecule

occurs when its HOMO is lifted above the Fermi surface of the metal tip resulting in a transfer of an electron to the metal. Thus in the mass spectrometer only positive ions are detected of the form $(H_2O)_nH_3O^+$ which one can view, for n = 3, as either a trimer attached to a hydronium ion or a protonated tetramer. Its lowest energy state in the absence of a field allows for two isomorphic conformations, shown on the left of Figure 7.9. Note that the proton has moved up to the center of the tetramer. As the field is increased up to 0.3 V/Å the straighter geometry remains intact with minor stretching diminishing the angle formed by three consecutive oxygen atoms. It begins to field-dissociate at 0.4 V/Å into a single water molecule and a protonated trimer that moves up the electric field for detection in the mass spectrometer. If the field is cranked up quickly to values between 0.9 and 1.2 V/Å a neutral water dimer is left behind with a protonated dimer moving away. This increase in the field strength must be done quickly enough on the time scale of the protonated trimer moving away from the single molecule. The sequence of disintegration is shown in Figure 7.10 as a function of the number of iterations in the geometry-optimization procedure. It is of note that as the proton moves up the whisker its charge becomes more and more delocalized with additional charge transfer to the closest oxygens. We recall that protonated trimers and tetramers are the most abundant species at fields below 0.5 V/Å in the experimental spectra, see Figure 7.1.

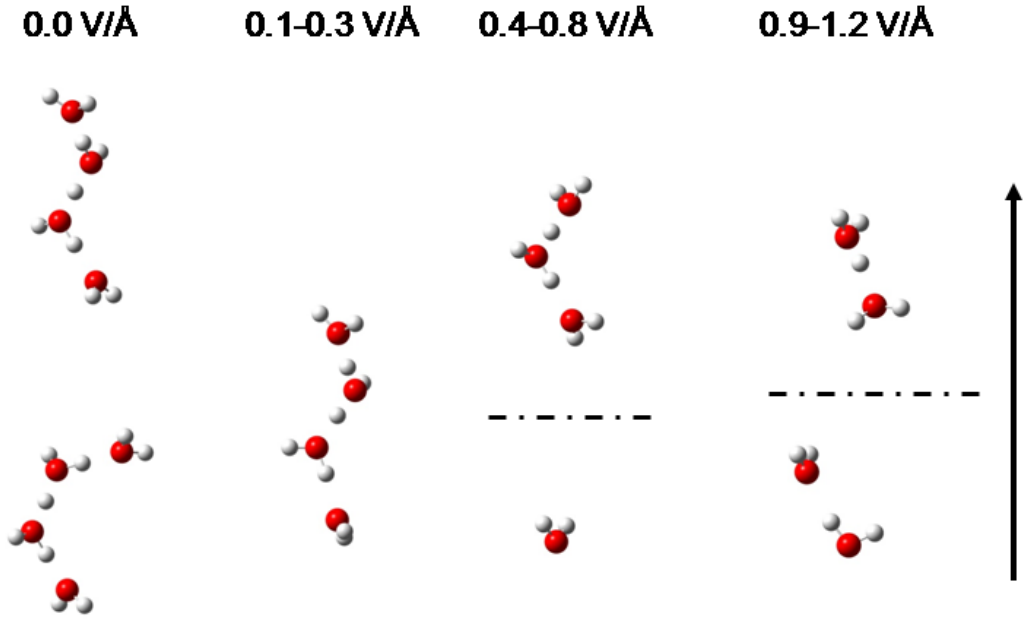

Figure 7.9 Protonated water tetramer in a field [140].

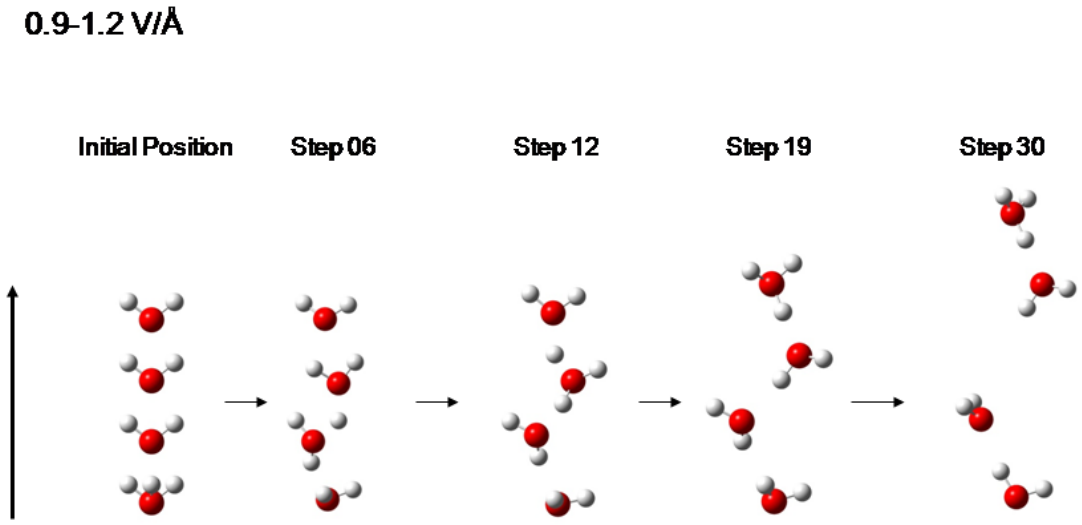

Figure 7.10 Field fragmentation of the protonated tetramer [140].

Our results are summarized in Figure 7.11 for both unprotonated and protonated clusters. There is unfortunately no systematic experimental study of these threshold fields. Rather pulsed field or photodesorption with synchrotron radiation has been used at a fixed field strength. Both methods remove the species from the surface as they are present at the

given field strength. In our comparison we can therefore only say that our results are in general agreement with experiments including the fact that predominantly small protonated clusters are seen. Also of note is the fact that protonated clusters are only stable for fields well below 1 V/Å in total agreement with the experimental findings.

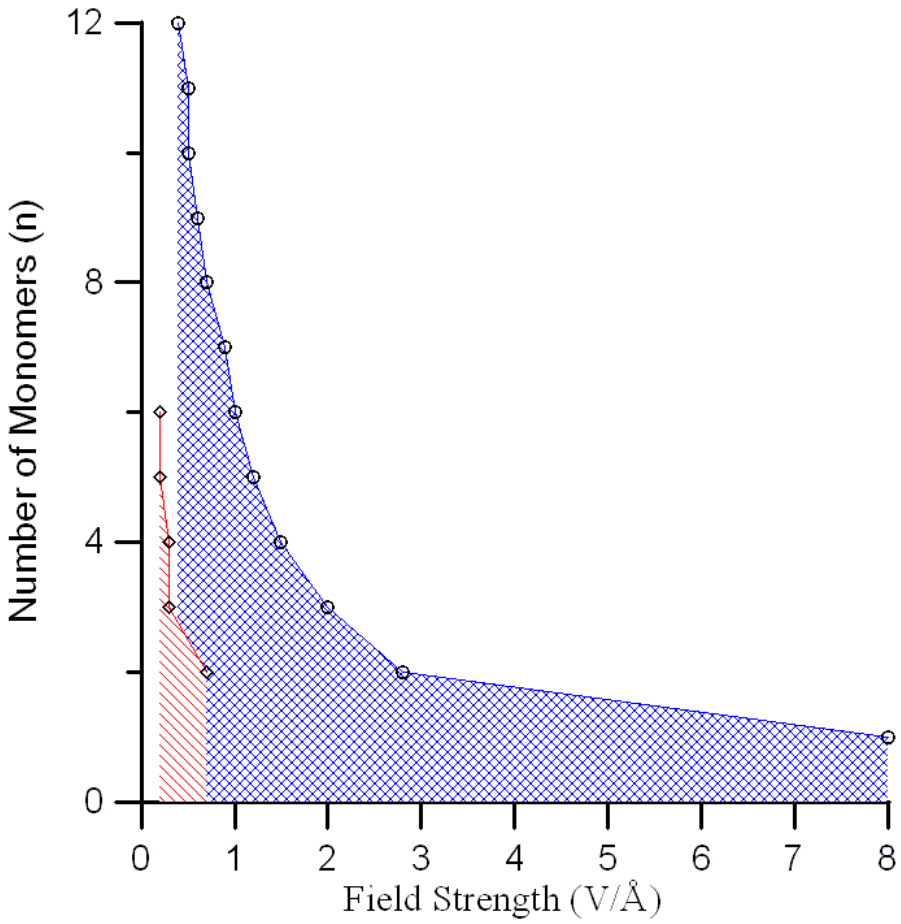

Figure 7.11 Stability diagram for neutral water whiskers (blue cross hatched region under the curve with circles) and protonated whiskers (red hatched region under the curve with diamonds) as a function of field strength with their regions of stability shaded [140].

7.2.2 Charge transfer

In this section we intend to elucidate the process of charge transfer along the proton wire further. We will present results from density functional calculations on the stability of proton wires in weak electrostatic fields of less than 0.1 V/Å as they occur across a cell membrane. To simulate the membrane environment we terminate the water whisker with

NH_3 at one end and with a cation $Zn^{++}(NH_3)_3$ as recently used by Isaev [189], [190]. Employing a procedure developed in section 7.1.1 [140] we will use the interim geometries in the iterations towards the geometry-optimized final result as snapshots to track the motion of one positive charge from the cation cluster up the proton wire to the ammonia group. By following the energy of the intermediate geometries and the position of the center of mass of the charge cloud as a function of the iteration steps we can plot the energy as a function of the center of mass position. This curve of course decreases to lower energies as the energy minimization proceeds but it also has local maxima at certain positions which are interpreted as the barriers that the charge cloud, i.e. the proton, must overcome as it moves up the wire. We take this result as the justification of the classical proton hopping model. We will also show that proton "hopping" is actually the exchange of a proton from one water molecule to the next by moving the electronic charge cloud in the opposite direction. Having the energy barriers we can get the transit times across the "membrane" and estimate the conductivity of the proton wire quantitatively. In addition, our quantum mechanical approach leads to a justification and further elucidation of the Grotthuss mechanism of charge transfer along proton wires [163].

In the absence of a field or a confining membrane channel a water cluster will be compact with the well known coordination of three to four hydrogen bonds. However, putting this cluster into a weak external field will turn it into a quasi-linear water whisker in its converged ground state geometry. The field must be weak enough to ensure stability because for stronger fields the whisker dissociates into smaller clusters. From our study of water whiskers in section 7.1 we know this happens e.g. for a tetramer or an hexamer in a field range of 0.01 to 0.1 V/Å i.e. in the range of typical membrane fields.

7.2.2.1 Terminated Tetramer

As indicated in the beginning of this section we will take $[Zn^{++}(NH_3)_3][H_2O]_4NH_3$ as the prototype of a short proton wire in a membrane although we have also done calculations with more water molecules which however, do not reveal new insights. This aggregate is

not linear but in its lowest energy state is globular. However, if we apply a small field of 0.005 V/Å it will remain straight albeit helical. As the DFT iterations proceed a positive charge will be transferred up to the ammonia group at the other end with the lowest energy state being a linear cluster $[Zn^{+}(NH_3)_3][H_2O]_4[NH_3]^{+}$; this had been the starting configuration in Isaev's work [190]. It should be recognized that a doubly charged ion generates a field $F = 2 \times 14.4/r^2$ [V/Å], i.e. about 1 V/Å at the other end of the complex, compared to which the field applied in the present work is minimal but still strong enough to ensure a linear structure.

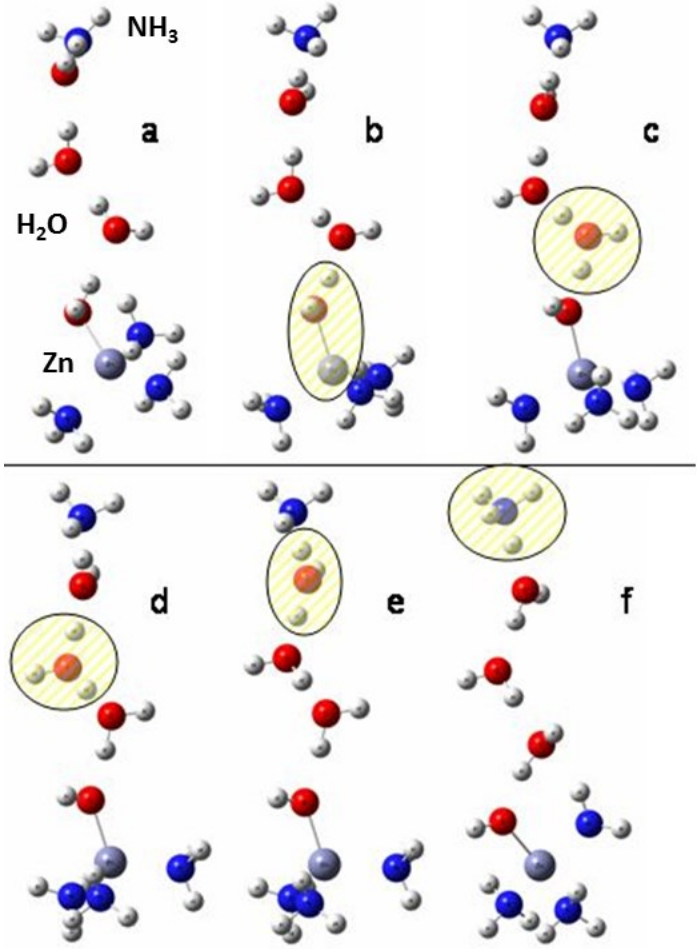

Figure 7.12 Geometric snapshots during the DFT iterations following the motion of the positive charge indicated by the highlighted region up the wire from its original position on the Zn-cluster to its final equilibrium position at the terminal ammonia group. The Zn is grey, N are blue, H are white, and O are red [141].

In Figure 7.12 we show a series of snapshots in the DFT iterative process with the position of the positive charge indicated by the highlighted region. The first image is the initial configuration with the terminal groups and the four water molecules clearly defined and the final image is the lowest energy state in which one of the positive charges has moved up the wire to the ammonia group. This happens as follows: in the second picture a hydrogen has already broken its bond with the lowest oxygen and is halfway in between it and the next oxygen up the wire. It moves closer creating a Zundel cation between the second and third water molecules and, at the same time one of the original hydrogens in the second water molecule detaches and moves up to the third oxygen [192]. This also results in a re-orientation of the second water molecule by an apparent clockwise rotation of about 90°. Note however, that the axis between the oxygen of the third water and one of its hydrogens does not change in its orientation. Thus the rotation of water molecules in the Grotthuss mechanism is not a rigid rotation but is simply the re-distribution of one of the hydrogen bonding orbitals. This process repeats itself one more time until a hydrogen is located close to the upper ammonia.

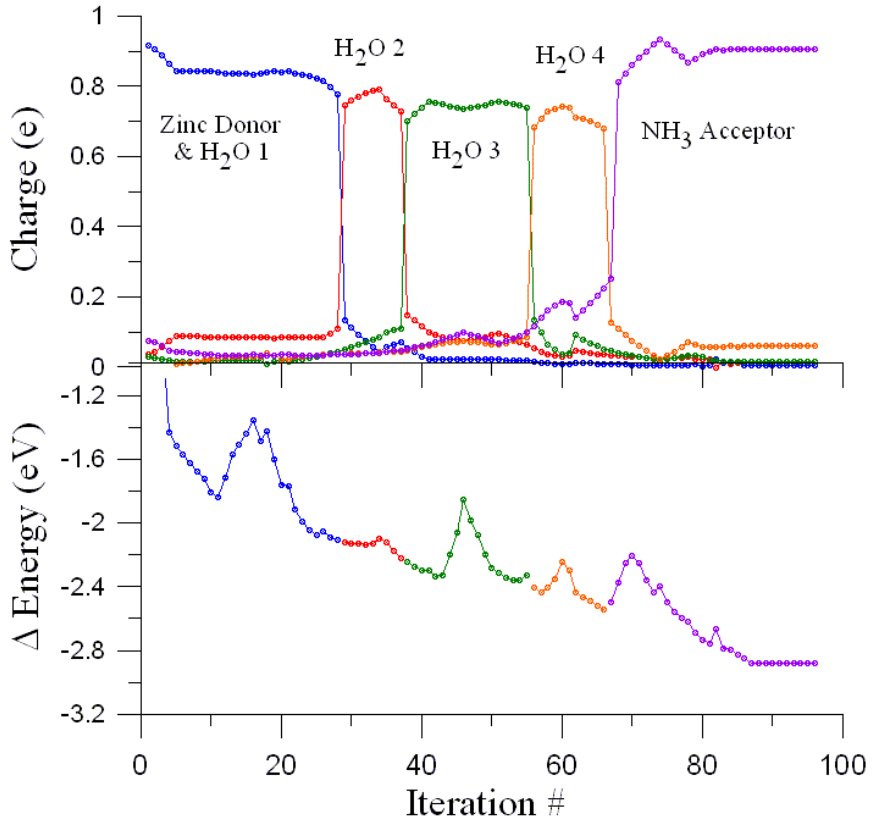

Figure 7.13 The electronic energy and the charges on the various subclusters along the chain as a function of the DFT iterations [141].

So far, we have deliberately talked about hydrogen moving up the wire and not protons because without further information we do not know its charge state or the energetics of the process. The latter is of course available as the total electronic energy of the system in each iteration step. This is plotted in Figure 7.13, lower curve. Overall the energy decreases as the system moves from an initial configuration to its absolute minimum. But, as we were anticipating, local barriers clearly show up which the hydrogen must overcome on its way from one water molecule to its neighbor up the wire. This is the quantum mechanical evidence that proton transfer is an activated process. Moreover, because the individual water molecules temporarily change their orientation we can take this, together with the re-orientation of the water molecules by bond adjustment, as a justification and elucidation of the Grotthuss mechanism of proton transfer in water.

However, at this stage caution is advised because the iterations themselves are purely numerical in nature (similar to the steps in Monte Carlo simulations). We need to extract

additional information. In section 7.1.1 [140] we suggested following a characteristic length scale as a function of the iterations and then eliminating the iteration steps to obtain the energy versus this length scale. For a proton wire this is the electronic charge cloud $\rho(\mathbf{r})$ around the cluster. To get a single coordinate we take the center of this charge cloud in the n^{th} iteration

$$r_{cm}^{(n)} = \int \rho^{(n)}(\mathbf{r})\boldsymbol{r}d^3\boldsymbol{r} \tag{65}$$

A convenient way to evaluate this average efficiently is to use the Mulliken charges $q_i^{(n)}$ on atom *i* in the cluster as this is a standard output of the Gaussian software. We would then get

$$\vec{r}_{cm}^{(n)} = \sum_i \vec{r}_i^{(n)} q_i^{(n)} \tag{66}$$

The diffficulty with implementing such an idea is the fact the local atomic charges within an assembly of atoms such as molecules are NOT quantum mechanical observables, i.e cannot be defined or calculated rigorously. This point is amply demonstrated in the present case by the fact that we cannot assign a proton that is halfway between two oxygen atoms to either one. Having this ambiguity we simply put forward as a criterion that we assign a proton to a given water molecule if it is within half the distance to the next oxygen i.e. a distance of about 1.2 Å. In the upper curve of Figure 7.13 we show the local charges on the Zn-cluster (including the lowest water molecule, the remaining three water molecules and the ammonia group at the other end) as a function of the iterations. Anticipating that one charge remains on the Zn cluster we have only plotted the one charge that is moving up. As the proton moves across the halfway distance between two oxygen atoms the charge drops abruptly on one water molecule and is picked up on the next one up the ladder. Noteworthy is the fact that there is never a charge of 1.0e on one of the subclusters but approximately 0.8e because the other subclusters continue to carry some charge. In other words, the total charge cloud $\rho^{(n)}(\boldsymbol{r})$ is rather diffuse. Yet the picture that a "charge" or proton moves up the wire is quite convincing.

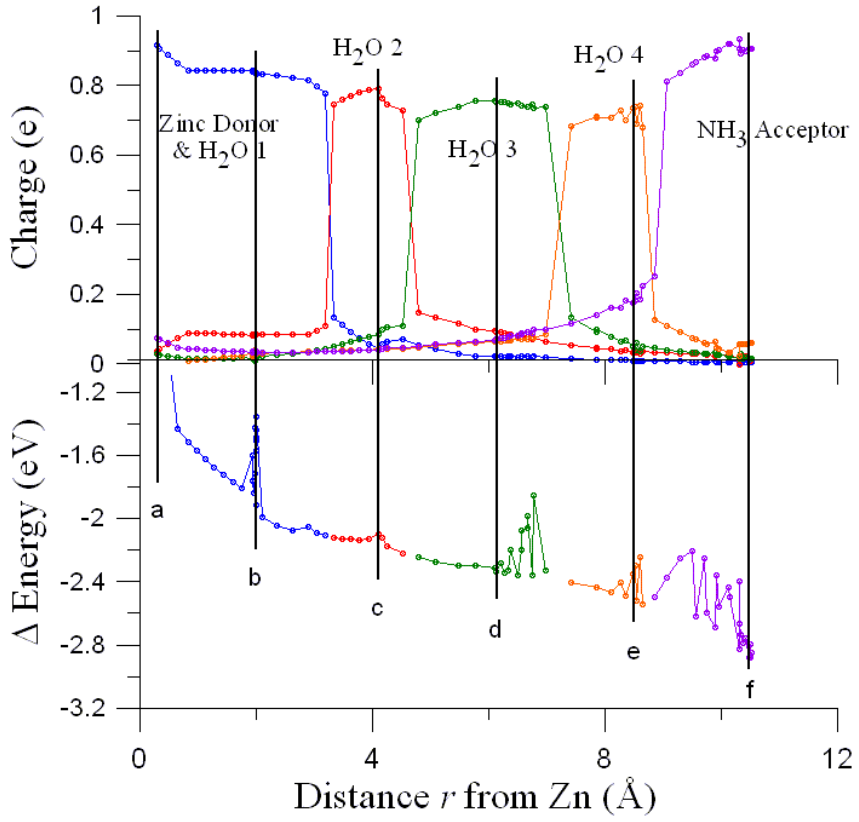

Figure 7.14 The energy and the subcluster charges as a function of the center of charge.The letters a-f refer to the temporary geometries depicted in Figure 7.12 [141].

To get a length scale we pick a number of points in the charge vs. iteration graph, e.g. the local maxima and measure the distance of this maximum from the Zn atom using the geometries shown in Figure 7.12. At this stage we can eliminate the iteration number and plot the energy as a function of the distance the charge cloud has traveled. This gives us the anticipated physical information about the energy landscape seen during charge transfer along the wire. This results in the lower curve in Figure 7.14: as the charge moves up the wire the electronic energy of the whole system is lowered except when the center of charge moves from one water molecule to the next, there is an energy barrier to be overcome. The picture of activated proton hopping is complete.

For clarification: the jaggedness within the activation barriers is a reflection that the hopping proton will make several attempts to get to the next water molecule, i.e. it is a reflection of local fluctuations. This can be taken as evidence of a Bjerrum defect [193] as recently discussed again by Pavlenko [163]. A Bjerrum defect is a crystallographic

defect which is specific to ice. Normally a hydrogen bond has one proton, but a hydrogen bond with two protons (no protons i.e. a hole) is called a Bjerrum D defect (L defect). The strain caused by the defect is resolved when a water molecule pivots about an oxygen atom to produce hydrogen bonds with single protons.

Looking at the geometries along this energy curve we can now identify what causes the barriers. To this end we have plotted in Figure 7.15 five geometries, namely at the beginning, at the height and at the end of the green barrier, and at the beginning and at the height of the orange barrier.

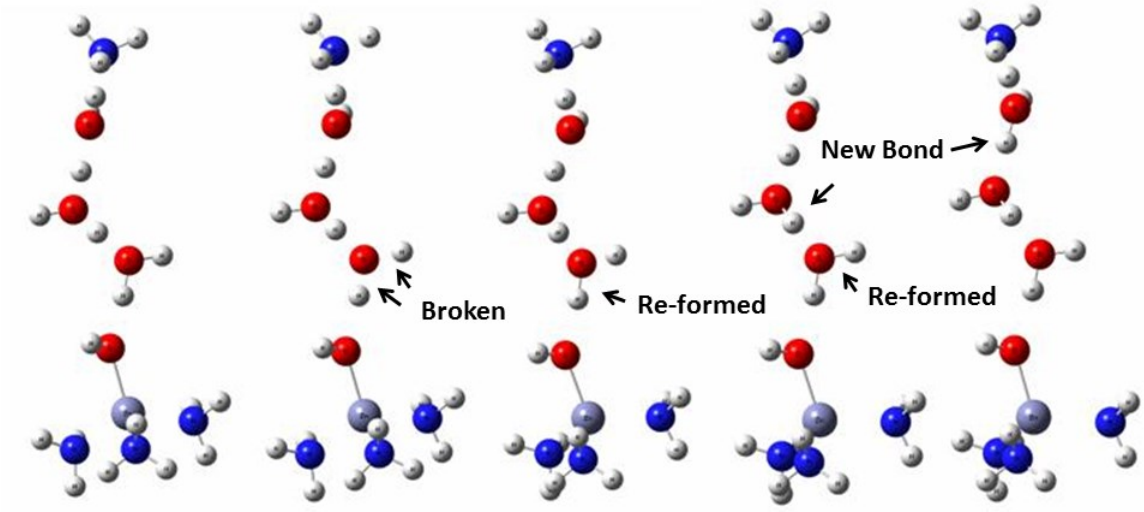

Figure 7.15 Five geometries, namely at the beginning, at the height and at the end of the green barrier, and at the beginning and at the height of the orange barrier in Figure 7.13. Changes in the hydrogen bonding are indicated via arrows and text [141].

At the height of the green barrier the hydrogen bonds to the second oxygen are stretched which costs energy, i.e. results in a barrier for further migration. One of the two bonds is re-formed at the end of the green barrier re-gaining this energy and at the beginning of the orange barrier the second hydrogen bond is re-formed.

7.2.2.2 Protonated Hexamer

A number of papers on the role of proton wires in biology simplify the model to one without terminal donor and acceptor groups [163], [175], [176], [178]–[182], [187]. As such a cluster of water molecules, either protonated or neutral, will assume a globular structure unless a small electric field is added to keep it in a linear configuration. Although we have reported a systematic study of such structures in section 7.1 [140] we want to briefly show some results for a protonated hexamer as it shows some surprising differences to the terminated whiskers (in a field). We follow the procedure used for the latter starting this time from a neutral whisker in a field. Adding a proton we follow the motion of the charge cloud up the wire, see Figure 7.16. The fifth and sixth water molecules remain neutral and thus are not shown.

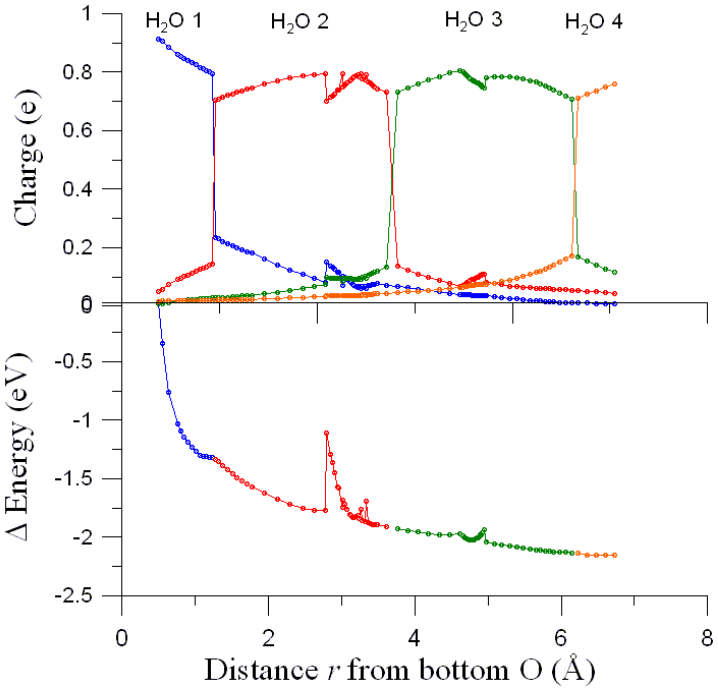

Figure 7.16 The energy and the subcluster charges as a function of the center of charge for a hexamer [141].

The most remarkable feature of this graph is the large reduction in the barriers to 0.001 (0.029), 0.66 (15.19), and 0.09 (1.98) eV (kcal/mol), (apart for the one really high barrier around 3 Å) as compared to the terminated whisker. The main reason for this is the fact that a whisker without heavy donor and acceptor groups at the ends has greater rotational

freedom i.e the two water molecules involved in a particular transfer event can more easily rotate at lower energy cost. This is obvious when one examines a series of snapshots like those in Figure 7.12. The exceptionally high barrier is associated with an attempt by the chain to twist as a whole.

The extra proton moves close to the lowest water molecule forming an H_3O^+ which in turn rotates and loosens its bond to the hydrogen in the direction of the field. This proton in turn moves closer to the next water molecule leaving a "neutral" H_2O behind and forming a new H_3O^+ which again rotates to accommodate the extra charge which is by now located beyond the second water molecule. This process - motion of the extra proton up the wire, rotation of the two closest water molecules and eventual attachment to the new host molecule repeats itself until the proton has reached the fourth water molecule in the chain.

7.3 Conclusions

We are now in a position to answer the five questions raised in the beginning of this chapter:

(1) What are the lower and upper threshold fields for water whiskers of different lengths?

The stability diagram in Figure 7.11 gives the threshold fields for the water whiskers and proton wires as a function of monomer number but one can also look at the stability as a function of the separation distance between the top and bottom oxygens in the whisker. We then see in Figure 7.17 that fitting an exponential to the O-O separation distance vs. electric field strength that one can make an estimate of the stable length of a water whisker given field strength. The maximum estimated length of a water whisker is approximately 33 angstroms. Of course, more calculations should be done to confirm the behavior still holds in this region.

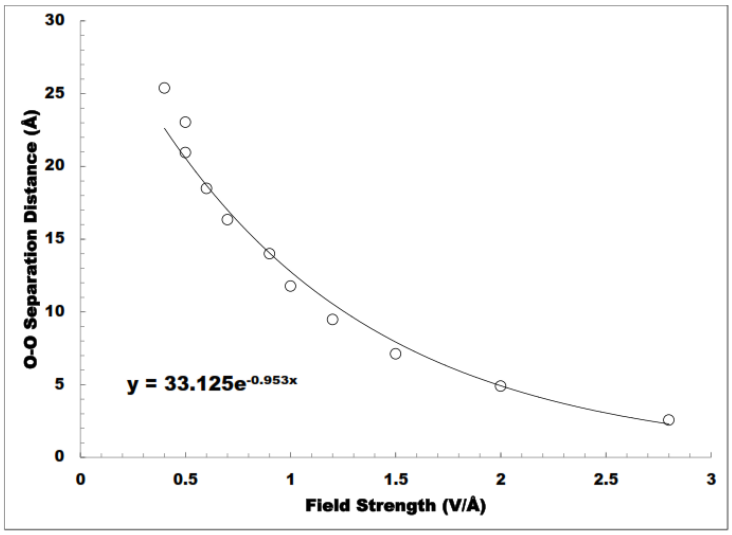

Figure 7.17 The separation distance of the top and bottom oxygens in the water whisker vs. the last field strength at which the whisker is stable. The calculated lengths are indicated by the open circles and the exponential fitting by the solid line with the fitting equation shown in the figure.

(2) How valid is the dipole alignment argument presented above?

In the Anway model it is assumed that the oxygen atoms lie in a straight line with the two hydrogen atoms oriented at some angle to facilitate energy gain through the field but maintain some possibility for hydrogen bonding as well. This picture is acceptable at small fields if it is modified by the fact that a lower energy state can be achieved by a staggered arrangement. Such an arrangement is also not planar but forms a helical conformer much akin to polymers. In this sense one might be tempted to call this field-induced polymerization. In addition, a simple classical dipole model does not allow for the transfer of charge down the field. In other words, a classical model does not allow field-dissociation.

(3) What is the effect of protonation?

Protonation has important consequences in that it destabilizes the whiskers earlier, simply because the additional proton moves up the field leading also to a re-arrangement of the

electrons. The ultimate consequence is that small protonated clusters are much more abundant in the mass spectrometer than larger clusters.

(4) How does the field-aligned whisker re-adjust when it is taken out of the high field region?
In field-induced desorption of water from a field emitter the clusters are protonated. As they move away from the high field region close to the field emitter tip and into regions of low or no field the whisker re-adjusts into a more compact structure with a hydration shell around the ion.

(5) What are the electronic mechanisms such as charge transfer that result in the formation of water whiskers and how does the charge transfer in a proton wire?

We have delineated two effects; (i) polarization and field alignment at small fields, and (ii) charge transfer and re-hybridization due to field modification of the molecular level structure at high fields that ultimately lead to field fragmentation at the point when the HOMO-LUMO gap closes and the whisker becomes conducting and field expulsion from the region of the whisker occurs.

Figure 7.18 shows the HOMO-LUMO gap vs. electric field strength for water whiskers consisting of n monomers (n=2-12). Across all the whiskers we see an initial rise in the H-L gap followed by a monotonic decrease up to the last stable configuration indicated by the last data point above the x-axis. At dissociation the H-L gap is negative indicating closure. There is a sudden change in the H-L gap from 0 to 0.1 V/Å if the structure changes from a globular cluster to a linear whisker. The calculated values of ~7-8 eV at

zero field are close to the experimental values of 6.9, 7.0, 8.7, 8.9, and 9.0 eV [194].

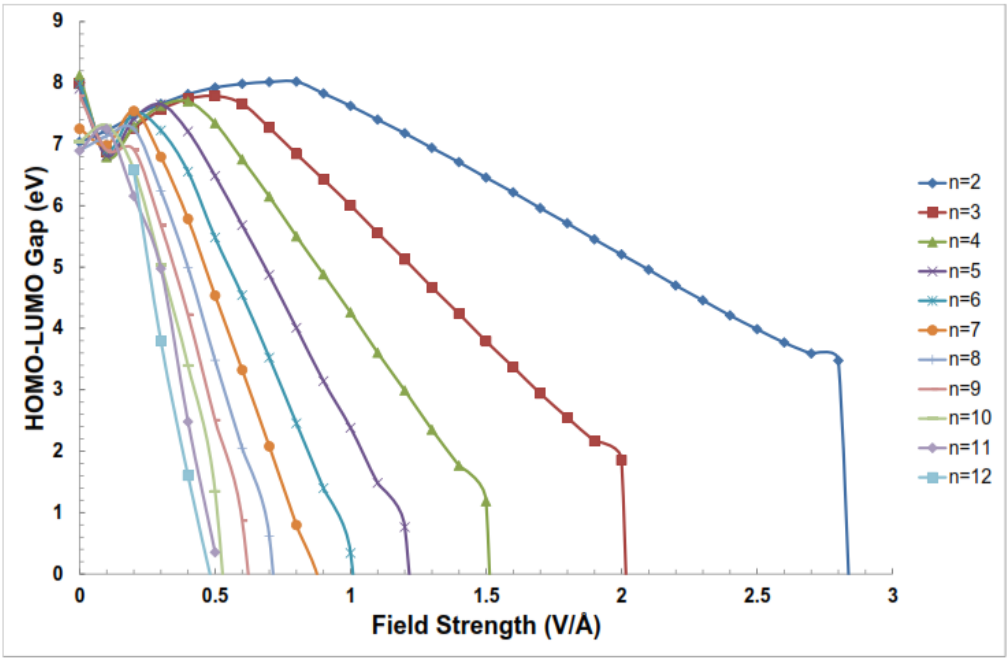

Figure 7.18 The HOMO-LUMO gap vs. electric field strength for water whiskers consisting of *n* water molecules (*n*=2-12).

The addition of a proton to a water whisker creating a proton wire causes the behaviour of the HOMO-LUMO gaps to change as shown in Figure 7.19. Firstly, the wire breaks apart at lower field strengths as discussed earlier in this chapter. Secondly, the H-L gaps do not go to zero upon dissociation, the last data point is when the proton wire dissociates. They do decrease rapidly however. This partial closure could be an artifact from the calculations because once the structure dissociates, there is no final optimized structure and the MOs change with each iteration of the optimization. It is possible that the gaps may close completely given enough iterations of the optimization. Another interesting feature is the higher H-L gap due to the proton and as the number of water molecules increase the gap moves closer to that of a water whisker.

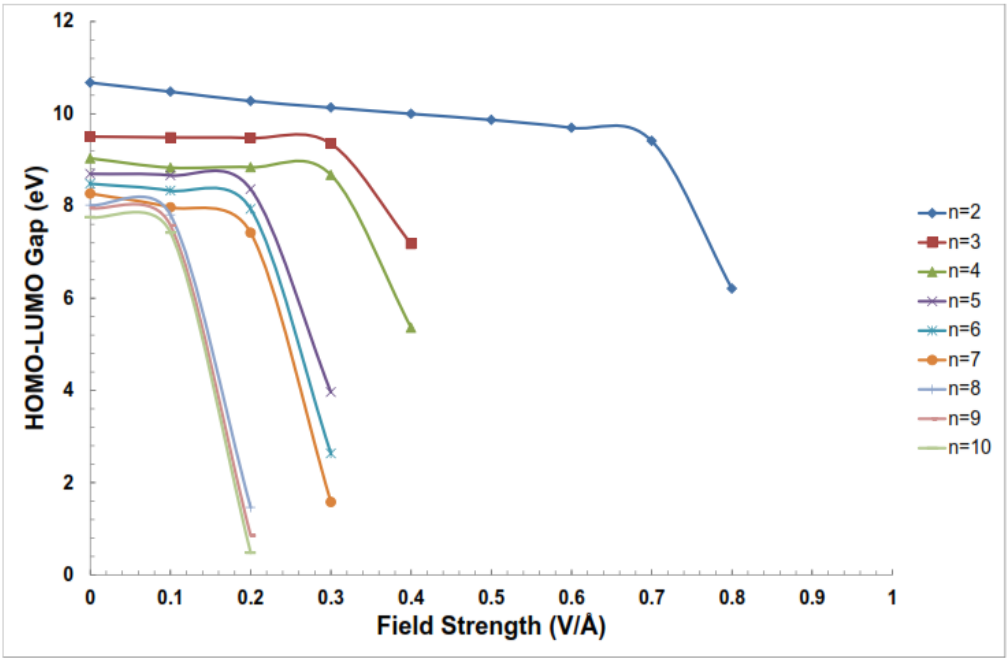

Figure 7.19 The HOMO-LUMO gap vs. electric field strength for proton wires consisting of *n* water molecules (*n*=2-10).

Charge transfer along a proton wire is an atomic exchange mechanism in which a proton moves the short distance of less than the O-O distance leaving behind a quasi-neutral water molecule and forming a temporary diffuse hydronium ion H_3O^+.

What is then the overall picture of charge or proton transfer through a membrane channel? We start from the equilibrium configuration $[Zn^+(NH_3)_3][H_2O]_4[NH_3]^+$. At some point in time a proton or hydronium ion, getting close to the Zn cluster will accept an electron getting neutralized and turning the Zn^+ into Zn^{2+}. If in a time interval before this charge transfer is reversed by another fluctuation, an electron is transferred from a water molecule on the other side of the membrane to the ammonia molecule a charge transfer has occurred across the membrane with the proton now on the other side. This results in the configuration $[Zn^{++}(NH_3)_3][H_2O]_4[NH_3]$ which will trigger the next round of charge transfer.

We stress again that a protonated water whisker without acceptor and donor groups has negligible activation barriers i.e. typically of the order of thermal energy at room temperature. This obviously casts doubt on the validity of classical Ising-type chain models in which one postulates well-defined and permanent minima along the chain for the extra proton which then hops over a barrier in the same way as an adsorbed particle hops from one adsorption site to the next in lattice gas models for surface diffusion. What emerges from our quantum mechanical calculations is a picture in which the transfer of a charge cloud from one water molecule to the next creates a local minimum and a barrier that disappears as soon as the charge has moved on.

Having dynamic information about the proton transfer mechanism we can estimate the transfer time and also the conductance of the proton wire. For the transfer time τ we note that it is limited by the sum of the inverse of the hopping rates over the barriers

$$\tau = \sum r_i^{-1} \tag{67}$$

Because the transfer time is much longer than any thermalization we can write

$$r_i = \frac{k_B T}{h} exp[\frac{-Q_i}{k_B T}] \tag{68}$$

where the barrier heights can be read off from left to right in Figure 7.13 to be 0.45 (10.39), 0.04 (0.89), 0.48 (11.07), 0.22 (5.02), and 0.33 (7.71) eV (kcal/mol) in agreement with the measured values for carbonic anhydrase of 0.043-0.11 eV (1.0-2.5 kcal/mol) for proton transfer and an overall energy barrier of 0.42-0.47 eV (9.8-11.0 kcal/mol) [195]–[197]. Because the transit time from one barrier to the next one a distance of a few angstroms away is less than a picosecond the proton arrives with some kinetic energy that has not been completely thermalized leading to a small reduction in the barrier heights. Taking this into account we get overall transit times of the order of microseconds, and possibly nanoseconds.
For the total current we get

$$I = \frac{e}{\tau} = GV_{\text{mem}} \tag{69}$$

Here V_{mem} is the membrane potential. For the two estimated transit times we get conductances of nS down to pS. We could not find measured values for isolated proton wires but note that for proton channels in Gramicidin A one finds 1.5 nS [198]. One should note that in a Gramicidin A channel the transit time is on the order of nanoseconds in the range of our estimates.

Our final comments concern the relation of this work with previous studies. In his quantum mechanical studies of proton wires Isaev [189], [190], using the same cluster and the same DFT framework apart from a somewhat smaller basis set, rightly observes that without a field an extra proton will settle in the middle of the wire, i.e. at equal distances from the acceptor and donor which are both charged. He examines extensively the variation in hydrogen bond lengths along the cluster which he finds are within a few hundredth of an angstrom. This is also what we find but do not put any emphasis on it as such a small variation is easily within the thermal fluctuations of the hydrogen bond at room temperature. In the classical Ising-type model of proton hopping Pavlenko [163] assumes that the hydrogen has four well-defined adsorption sites between any two oxygens along the chain. Such an assignment assumes that there are energy barriers on either side of these sites. We see some evidence for that, see Figure 7.14.

CHAPTER 8 Conclusions

The questions considered in this thesis revolve around the effects of high electrostatic fields on various materials. Density functional theory is extensively used to calculate *ab initio* the behavior of the materials in the electric field. A water whisker is quite different from a MgO cluster but the fundamental approach to these problems is the same. The starting point is looking at the structure in field-free conditions. Once this is done, an electrostatic field is applied and the changes in the geometry of the material are tracked through the iterations in a geometry optimization. Various quantities such as energy, force, charge, electric field, etc. can be extracted or calculated depending on the question at hand. These are then used to explain experimental observations.

The physical picture begins quite simply with a high electric field applied across a material. As discussed in Chapter 2, the electric field E applied across a material will raise the energy levels of a MO up the field to another MO down the field by a factor of qEd where d is the separation distance between the relevant atoms. This rearrangement of the bonding and antibonding orbitals can cause: (i) the electronic transformation of one material into another such as N_2 into CO as discussed in Chapter 2 on field-induced chemistry, (ii) the formation of new structures which are stable in the field such as the water whiskers discussed in Chapter 7. The electric field will also drive charge down a water whisker turning it into a proton wire. We calculated the stability of protonated water whiskers and found agreement with experimental results that whiskers consisting of 3-4 molecules were abundant at the given field strength. We also confirmed the Grothuss mechanism as a method of charge transfer down a proton wire and calculated the energy barriers.

The changing MO energy levels not only can cause new structures but also aid in their dissociation. As shown in Figures 2.4, 2.5, and 4.15 the tunneling barrier for an electron decreases while the HOMO level is raised relative to the barrier, with an increasing field. Thus, from the perspective of the electron, field ionization, dissociation, and evaporation

are all due to the raising of the electrons energy level while the tunneling barrier is reduced or removed entirely. As seen in Figure 4.15, an electron at the HOMO level, at field strengths close to the evaporation field strength, has few barriers inside the ZnO cluster, in effect acting like a free electron in a conductor. This metallization of the surface is responsible for the effectiveness of laser-assisted APT of semiconductors and insulators.

After looking at 4 different materials in 41 configurations we see that in the majority of cases the HOMO-LUMO gap closes or partially closes upon field evaporation or dissociation of the material indicating field-induced metallization and the effects of raising MO energies.

Other indicators of field-induced metallization as discussed previously are rapid increases in the polarizability and dielectric constant of a material as shown in Figure 8.1 for MgO, ZnO, and Si. They were calculated using the methods of Chapter 4. The experimental values are indicated by the dashed black lines. There is good agreement with experimental values for small fields for several of the systems.

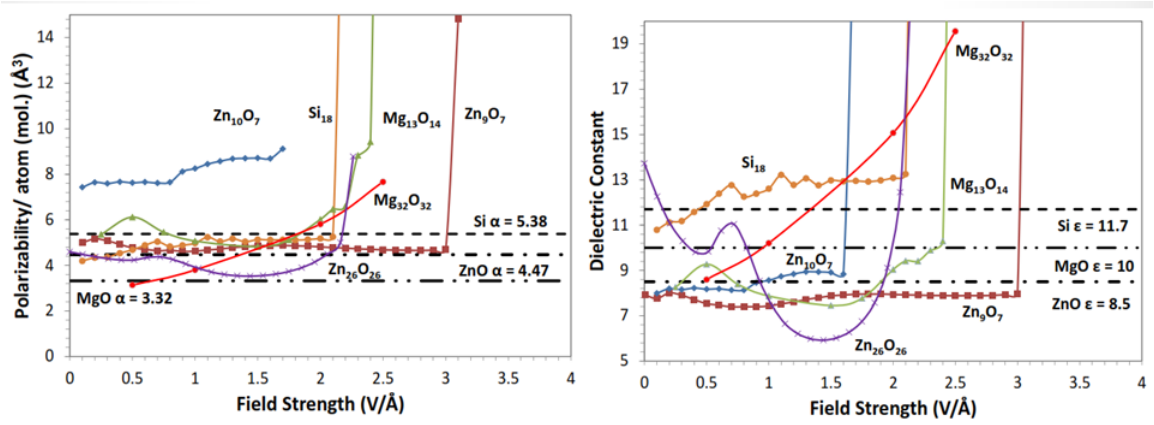

Figure 8.1 The polarizabilty and dielectric constant of MgO, ZnO, and Si clusters as a function of the electric field. Experimental values are indicated by the dashed lines.

Further work that can still be done are:

- Using Time dependent DFT to look at the kinetics and excited states during the evaporation process to calculate the ion yield and compare with experiment.

- The role of spin multiplicity in terms of calculated evaporation products should be investigated further to make sure the various compound ions seen in experiment can be reproduced.
- Calculate the depth of field-induced metallization through the layers of a 6x6x6 cluster; in effect sweeping from the surface to middle of the cluster.
- Given that APT reconstructions are based on the assumption that an ion will follow a field line from the evaporation site to the detector, it would be possible to calculate the degree of lateral motion during the evaporation process and test that assumption to improve reconstructions.
- It would be useful to construct an evaporation atlas so to speak consisting of calculations using multiple levels of theory of the evaporation field strength of each element, that can be shaped into a tip of course. To be consistent in terms of geometry one should probably use a unit cell. This can then be compared with or replace the results from the Image hump model and Kingham curves.
- A cluster model can be used to investigate the underlying physics of APT hybrid systems, for e.g., dielectrics with embedded metallic nanoclusters, or metals with embedded dielectric or oxide clusters by encasing an oxide cluster with two layers of a metal and studying the evaporation process.

BIBLIOGRAPHY

[1] H. J. Kreuzer, “Physics and chemistry in high electric fields,” *Surf. Sci.*, vol. 246, no. 1–3, pp. 336–347, Apr. 1991.

[2] H. J. Kreuzer, “Physics and chemistry in high electric fields,” *Surf. Interface Anal.*, vol. 36, no. 5–6, pp. 372–379, 2004.

[3] H. J. Kreuzer, “Surface Physics and Chemistry in High Electric Fields,” in *Chemistry and Physics of Solid Surfaces VIII*, P. R. Vanselow and D. R. Howe, Eds. Springer Berlin Heidelberg, 1990, pp. 133–158.

[4] Kreuzer H. J., “Chemical Reactions in High Electric Fields,” in *Surface Science of Catalysis*, vol. 482, 0 vols., American Chemical Society, 1992, pp. 268–286.

[5] J. H. Block, “Field Desorption and Photon-Induced Field Desorption,” in *Chemistry and Physics of Solid Surfaces IV*, P. R. Vanselow and P. R. Howe, Eds. Springer Berlin Heidelberg, 1982, pp. 407–434.

[6] D. J. Griffiths, *Introduction to Electrodynamics*, 3 edition. Upper Saddle River, N.J: Addison-Wesley, 1998.

[7] E. W. Müller, J. A. Panitz, and S. B. McLane, “The Atom-Probe Field Ion Microscope,” *Rev. Sci. Instrum.*, vol. 39, no. 1, pp. 83–86, Jan. 1968.

[8] E. W. Müller, “Das Feldionenmikroskop,” *Z. Für Phys.*, vol. 131, no. 1, pp. 136–142, Mar. 1951.

[9] B. Gault, M. P. Moody, J. M. Cairney, and S. P. Ringer, *Atom Probe Microscopy*, vol. 160. New York, NY: Springer New York, 2012.

[10] E. P. Silaeva, M. Karahka, and H. J. Kreuzer, “Atom Probe Tomography and field evaporation of insulators and semiconductors: Theoretical issues,” *Curr. Opin. Solid State Mater. Sci,* vol. 17, 5, October 2013, Pages 211–216.

[11] M. K. Miller, A. Cerezo, M. G. Hetherington, and G. D. W. Smith, *Atom Probe Field Ion Microscopy*. Oxford, England: Oxford Science Publications, 1996.

[12] R. Gomer, “Field Desorption,” *J. Chem. Phys.*, vol. 31, no. 2, pp. 341–345, Aug. 1959.

[13] F. Vurpillot, A. Gaillard, G. Da Costa, and B. Deconihout, “A model to predict image formation in Atom probeTomography,” *Ultramicroscopy*, vol. 132, pp. 152–157, Sep. 2013.

[14] C. Oberdorfer and G. Schmitz, “On the Field Evaporation Behavior of Dielectric Materials in Three-Dimensional Atom Probe: A Numeric Simulation,” *Microsc. Microanal.*, vol. 17, no. 1, pp. 15–25, 2011.

[15] A. L. Pregenzer, K. W. Bieg, R. E. Olson, and J. A. Panitz, “Ion production from LiF-coated field emitter tips,” *J. Appl. Phys.*, vol. 67, no. 12, pp. 7556–7559, Jun. 1990.

[16] D. Larson, R. Alvis, D. Lawrence, T. Prosa, R. Ulfig, D. Reinhard, P. Clifton, S. Gerstl, J. Bunton, D. Lenz, T. Kelly, and K. Stiller, “Analysis of Bulk Dielectrics with Atom Probe Tomography,” *Microsc. Microanal.*, vol. 14, no. Supplement S2, pp. 1254–1255, 2008.

[17] T. T. Tsong, “Field penetration and band bending near semiconductor surfaces in high electric fields,” *Surf. Sci.*, vol. 81, no. 1, pp. 28–42, Feb. 1979.

[18] M. K. Miller and R. G. Forbes, “Field Evaporation and Related Topics,” in *Atom-Probe Tomography*, Springer US, 2014, pp. 111–187.

[19] T. T. Tsong, *Atom-probe field ion microscopy: Field ion emission and surfaces and interfaces at atomic resolution*. Cambridge: Cambridge University Press, 1990.

[20] R. Haydock and D. R. Kingham, “Post-Ionization of Field-Evaporated Ions,” *Phys. Rev. Lett.*, vol. 44, no. 23, pp. 1520–1523, Jun. 1980.

[21] L. C. Wang and H. J. Kreuzer, “Kinetic theory of field evaporation of metals,” *Surf. Sci.*, vol. 237, no. 1–3, pp. 337–346, Nov. 1990.

[22] Y. Suchorski, N. Ernst, W. A. Schmidt, V. K. Medvedev, H. J. Kreuzer, and R. L. C. Wang, “Field desorption and field evaporation of metals: In memoriam Professor J.H. Block,” *Prog. Surf. Sci.*, vol. 53, no. 2–4, pp. 135–153, Oct. 1996.

[23] Tien Tzou Tsong, “On the mechanism of field evaporation,” *Surf. Sci.*, vol. 10, no. 1, pp. 102–117, Apr. 1968.

[24] Kreuzer, Wang, and Lang, “Self-consistent calculation of atomic adsorption on metals in high electric fields,” *Phys. Rev. B Condens. Matter*, vol. 45, no. 20, pp. 12050–12055, May 1992.

[25] N. D. Lang and W. Kohn, “Theory of Metal Surfaces: Charge Density and Surface Energy,” *Phys. Rev. B*, vol. 1, no. 12, pp. 4555–4568, Jun. 1970.

[26] N. D. Lang and A. R. Williams, “Theory of atomic chemisorption on simple metals,” *Phys. Rev. B*, vol. 18, no. 2, pp. 616–636, Jul. 1978.

[27] Y. Suchorski, W. A. Schmidt, J. H. Block, and H. J. Kreuzer, “Comparative studies on field ionization at surface sites of Rh, Ag and Au—differences in local electric field enhancement,” *Vacuum*, vol. 45, no. 2–3, pp. 259–262, Feb. 1994.

[28] Y. Suchorski, W. A. Schmidt, N. Ernst, J. H. Block, and H. J. Kreuzer, “Electrostatic fields above individual atoms,” *Prog. Surf. Sci.*, vol. 48, no. 1–4, pp. 121–134, Jan. 1995.

[29] W. A. Schmidt, Y. Suchorski, J. H. Block, H. J. Kreuzer, and R. L. C. Wang, “Field ion appearance energy spectroscopy of CO+ originated from Rh(111) and Au(111) surface step sites,” *Surf. Sci.*, vol. 326, no. 3, pp. 243–251, Mar. 1995.

[30] H. . Kreuzer, K. Watanabe, and L. . Wang, “Theory of field desorption and field ionization: Thermal field desorption of helium,” *Surf. Sci.*, vol. 232, no. 3, pp. 379–392, Jun. 1990.

[31] B. S. Nickerson, “KINETICS OF FIELD EVAPORATION,” MSc, Dalhousie, Halifax, NS, Canada, 2015.

[32] M. Razavy, *Quantum Theory of Tunneling*. WORLD SCIENTIFIC, 2003.

[33] “Principles of Semiconductor Devices.” [Online]. Available: http://ecee.colorado.edu/~bart/book/home.htm. [Accessed: 06-Aug-2016].

[34] M. Born and R. Oppenheimer, “Zur Quantentheorie der Molekeln,” *Ann. Phys.*, vol. 389, no. 20, pp. 457–484, 1927.

[35] Y. Jean, F. Volatron, and J. K. Burdett, *An introduction to molecular orbitals*. Taylor & Francis US, 1993.

[36] P. Hohenberg and W. Kohn, “Inhomogeneous Electron Gas,” *Phys. Rev.*, vol. 136, no. 3B, pp. B864–B871, Nov. 1964.

[37] W. Kohn and L. J. Sham, “Self-Consistent Equations Including Exchange and Correlation Effects,” *Phys. Rev.*, vol. 140, no. 4A, pp. A1133–A1138, Nov. 1965.

[38] D. M. Ceperley and B. J. Alder, “Ground State of the Electron Gas by a Stochastic Method,” *Phys. Rev. Lett.*, vol. 45, no. 7, pp. 566–569, Aug. 1980.

[39] A. D. Becke, “A new mixing of Hartree–Fock and local density-functional theories,” *J. Chem. Phys.*, vol. 98, no. 2, pp. 1372–1377, Jan. 1993.

[40] M. Frisch, G. Trucks, H. Schlegel, G. Scuseria, M. Robb, J. Cheeseman, G. Scalmani, V. Barone, B. Mennucci, G. Petersson, H. Nakatsuji, M. Caricato, X. Li, H. Hratchian, A. Izmaylov, J. Bloino, G. Zheng, J. Sonnenberg, M. Hada, M. Ehara, K. Toyota, R. Fukuda, J. Hasegawa, M. Ishida, T. Nakajima, Y. Honda, O. Kitao, H. Nakai, T. Vreven, J. Montgomery, J. Peralta, F. Ogliaro, M. Bearpark, J. Heyd, E. Brothers, K. Kudin, V. Staroverov, R. Kobayashi, J. Normand, K. Raghavachari, A. Rendell, J. Burant, S. Iyengar, J. Tomasi, M. Cossi, N. Rega, J. Millam, M. Klene, J. Knox, J. Cross, V. Bakken, C. Adamo, J. Jaramillo, R. Gomperts, R. Stratmann, O. Yazyev, A. Austin, R. Cammi, C. Pomelli, J. Ochterski, R. Martin, K. Morokuma, V. Zakrzewski, G. Voth, P. Salvador, J. Dannenberg, S. Dapprich, A. Daniels, Farkas, J. Foresman, J. Ortiz, J. Cioslowski, and D. Fox, “Gaussian 09, Revision B.01,” *Gaussian 09 Revis. B01 Gaussian Inc Wallingford CT*, 2009.

[41] J. B. Foresman and Ae. Frisch, *Exploring Chemistry With Electronic Structure Methods: A Guide to Using Gaussian*, 2 edition. Pittsburgh, PA: Gaussian, 1996.

[42] H. B. Schlegel, “Optimization of equilibrium geometries and transition structures,” *J. Comput. Chem.*, vol. 3, no. 2, pp. 214–218, Jun. 1982.

[43] B. G. Johnson, P. M. W. Gill, J. A. Pople, and D. J. Fox, “Computing molecular electrostatic potentials with the PRISM algorithm,” *Chem. Phys. Lett.*, vol. 206, no. 1, pp. 239–246, Apr. 1993.

[44] R. S. Mulliken, “Electronic Population Analysis on LCAO–MO Molecular Wave Functions. I,” *J. Chem. Phys.*, vol. 23, no. 10, pp. 1833–1840, Oct. 1955.

[45] M. L. Karahka and H. J. Kreuzer, “New physics and chemistry in high electrostatic fields,” *Surf. Sci.*, vol. 643, pp. 164–171, Jan. 2016.

[46] N. Ernst, W. Drachsel, Y. Li, J. H. Block, and H. J. Kreuzer, “Field Adsorption of Helium on Tungsten,” *Phys. Rev. Lett.*, vol. 57, no. 21, pp. 2686–2689, Nov. 1986.

[47] J. R. Riley, R. A. Bernal, Q. Li, H. D. Espinosa, G. T. Wang, and L. J. Lauhon, “Atom Probe Tomography of a-Axis GaN Nanowires: Analysis of Nonstoichiometric Evaporation Behavior,” *ACS Nano*, vol. 6, no. 5, pp. 3898–3906, May 2012.

[48] A. Devaraj, R. Colby, W. P. Hess, D. E. Perea, and S. Thevuthasan, “Role of Photoexcitation and Field Ionization in the Measurement of Accurate Oxide Stoichiometry by Laser-Assisted Atom Probe Tomography,” *J. Phys. Chem. Lett.*, vol. 4, no. 6, pp. 993–998, Mar. 2013.

[49] K. Stiller, L. Viskari, G. Sundell, F. Liu, M. Thuvander, H.-O. Andrén, D. J. Larson, T. Prosa, and D. Reinhard, “Atom Probe Tomography of Oxide Scales,” *Oxid. Met.*, vol. 79, no. 3–4, pp. 227–238, Apr. 2013.

[50] E. A. Marquis, N. A. Yahya, D. J. Larson, M. K. Miller, and R. I. Todd, “Probing the improbable: imaging C atoms in alumina,” *Mater. Today*, vol. 13, no. 10, pp. 34–36, Oct. 2010.

[51] A. Vella, B. Mazumder, G. D. Costa, and B. Deconihout, “Field evaporation mechanism of bulk oxides under ultra fast laser illumination,” *J. Appl. Phys.*, vol. 110, no. 4, p. 44321, Aug. 2011.

[52] B. Mazumder, A. Vella, B. Deconihout, and T. Al-Kassab, “Evaporation mechanisms of MgO in laser assisted atom probe tomography,” *Ultramicroscopy*, vol. 111, no. 6, pp. 571–575, May 2011.

[53] W. C. Dash and R. Newman, “Intrinsic Optical Absorption in Single-Crystal Germanium and Silicon at 77°K and 300°K” *Phys. Rev.*, vol. 99, no. 4, pp. 1151–1155, Aug. 1955.

[54] E. P. Silaeva, A. Vella, N. Sevelin-Radiguet, G. Martel, B. Deconihout, and T. E. Itina, “Ultrafast laser-triggered field ion emission from semiconductor tips,” *New J. Phys.*, vol. 14, no. 11, p. 113026, 2012.

[55] L. V. Keldysh, “Behavior of Non-metallic Crystals in Strong Electric Fields,” *Sov. J. Exp. Theor. Phys.*, vol. 6, p. 763, 1958.

[56] E. P. Silaeva, N. S. Shcheblanov, T. E. Itina, A. Vella, J. Houard, N. Sévelin-Radiguet, F. Vurpillot, and B. Deconihout, “Numerical study of femtosecond laser-assisted atom probe tomography,” *Appl. Phys. A*, vol. 110, no. 3, pp. 703–707, Sep. 2012.

[57] L. Rigutti, A. Vella, F. Vurpillot, A. Gaillard, N. Sevelin-Radiguet, J. Houard, A. Hideur, G. Martel, G. Jacopin, A. D. Luna Bugallo, and B. Deconihout, “Coupling atom probe tomography and photoluminescence spectroscopy: Exploratory results and perspectives,” *Ultramicroscopy*, vol. 132, pp. 75–80, Sep. 2013.

[58] M. N. Bachhav, R. Danoix, F. Vurpillot, B. Hannoyer, S. B. Ogale, and F. Danoix, “Evidence of lateral heat transfer during laser assisted atom probe tomography

analysis of large band gap materials," *Appl. Phys. Lett.*, vol. 99, no. 8, p. 84101, Aug. 2011.

[59] A. Vella, E. P. Silaeva, J. Houard, T. E. Itina, and B. Deconihout, "Probing the thermal response of a silicon field emitter by ultra-fast Laser Assisted Atom Probe Tomography," *Ann. Phys.*, vol. 525, no. 1–2, pp. L1–L5, Feb. 2013.

[60] Z. W. Gortel and H. J. Kreuzer, "Forward peaking and thermalization in the desorption of helium," *Phys. Rev. B*, vol. 31, no. 6, pp. 3330–3337, Mar. 1985.

[61] V. N. Strekalov, "Photofield migration and desorption of impurity ions," *Tech. Phys.*, vol. 42, no. 12, pp. 1426–1428, Dec. 1997.

[62] H. Tamura, M. Tsukada, K. P. McKenna, A. L. Shluger, T. Ohkubo, and K. Hono, "Laser-assisted field evaporation from insulators triggered by photoinduced hole accumulation," *Phys. Rev. B*, vol. 86, no. 19, p. 195430, Nov. 2012.

[63] H. Sumi, "Theory on laser sputtering by high-density valence-electron excitation of semiconductor surfaces," *Surf. Sci.*, vol. 248, no. 3, pp. 382–410, Jun. 1991.

[64] T. T. Tsong, J. H. Block, M. Nagasaka, and B. Viswanathan, "Photon stimulated field ionization," *J. Chem. Phys.*, vol. 65, no. 6, pp. 2469–2470, Sep. 1976.

[65] B. Mazumder, A. Vella, M. Gilbert, B. Deconihout, and G. Schmitz, "Reneutralization time of surface silicon ions on a field emitter," *New J. Phys.*, vol. 12, no. 11, p. 113029, 2010.

[66] B. Mazumder, A. Vella, F. Vurpillot, G. Martel, and B. Deconihout, "Surface carrier recombination of a silicon tip under high electric field," *Appl. Phys. Lett.*, vol. 97, no. 7, p. 73104, Aug. 2010.

[67] J. Bogdanowicz, M. Gilbert, N. Innocenti, S. Koelling, B. Vanderheyden, and W. Vandervorst, “Light absorption in conical silicon particles,” *Opt. Express*, vol. 21, no. 3, p. 3891, Feb. 2013.

[68] S. Koelling, N. Innocenti, A. Schulze, M. Gilbert, A. K. Kambham, and W. Vandervorst, “In-situ observation of non-hemispherical tip shape formation during laser-assisted atom probe tomography,” *J. Appl. Phys.*, vol. 109, no. 10, p. 104909, May 2011.

[69] J. Houard, A. Vella, F. Vurpillot, and B. Deconihout, “Three-dimensional thermal response of a metal subwavelength tip under femtosecond laser illumination,” *Phys. Rev. B*, vol. 84, no. 3, p. 33405, Jul. 2011.

[70] M. Karahka and H. J. Kreuzer, “Field evaporation of oxides: A theoretical study,” *Ultramicroscopy*, vol. 132, pp. 54–59, Sep. 2013.

[71] M. Kuduz, G. Schmitz, and R. Kirchheim, “Investigation of oxide tunnel barriers by atom probe tomography (TAP),” *Ultramicroscopy*, vol. 101, no. 2–4, pp. 197–205, Nov. 2004.

[72] A. N. Chiaramonti, D. K. Schreiber, W. F. Egelhoff, D. N. Seidman, and A. K. Petford-Long, “Effects of annealing on local composition and electrical transport correlations in MgO-based magnetic tunnel junctions,” *Appl. Phys. Lett.*, vol. 93, no. 10, pp. 103113-103113–3, Sep. 2008.

[73] C. Oberdorfer, P. Stender, C. Reinke, and G. Schmitz, “Laser-Assisted Atom Probe Tomography of Oxide Materials,” *Microsc. Microanal.*, vol. 13, no. 5, pp. 342–346, 2007.

[74] K. E. Yoon, D. N. Seidman, C. Antoine, and P. Bauer, “Atomic-scale chemical analyses of niobium oxide/niobium interfaces via atom-probe tomography,” *Appl. Phys. Lett.*, vol. 93, no. 13, pp. 132502-132502–3, Oct. 2008.

[75] Y. M. Chen, T. Ohkubo, and K. Hono, “Laser assisted field evaporation of oxides in atom probe analysis,” *Ultramicroscopy*, vol. 111, no. 6, pp. 562–566, May 2011.

[76] Y. M. Chen, T. Ohkubo, M. Kodzuka, K. Morita, and K. Hono, “Laser-assisted atom probe analysis of zirconia/spinel nanocomposite ceramics,” *Scr. Mater.*, vol. 61, no. 7, pp. 693–696, Oct. 2009.

[77] D. Larson, “Private communication.” 2012.

[78] M. Tsukada, H. Tamura, K. P. McKenna, A. L. Shluger, Y. M. Chen, T. Ohkubo, and K. Hono, “Mechanism of laser assisted field evaporation from insulating oxides,” *Ultramicroscopy*, vol. 111, no. 6, pp. 567–570, May 2011.

[79] D. Tomanek, H. J. Kreuzer, and J. H. Block, “THEORETICAL APPROACH TO FIELD DESORPTION, TIGHT BINDING CALCULATION OF N_2 ON Fe(111),” *J. Phys. Colloq.*, vol. 47, no. C2, pp. C2-139-C2-144, Mar. 1986.

[80] K. Nath, H. J. Kreuzer, and A. B. Anderson, “Field adsorption of rare gases,” *Surf. Sci.*, vol. 176, no. 1–2, pp. 261–283, Oct. 1986.

[81] K. Huber, *Molecular Spectra and Molecular Structure: IV. Constants of Diatomic Molecules*. Springer Science & Business Media, 2013.

[82] C. W. B. Jr, B. H. L. Iii, and B. Liu, “The dissociation energy of MgO,” *J. Chem. Phys.*, vol. 77, no. 8, pp. 4084–4087, Oct. 1982.

[83] L. R. C. Wang, H. J. Kreuzer, and O. Nishikawa, “Polythiophene in strong electrostatic fields,” *Org. Electron.*, vol. 7, no. 2, pp. 99–106, Apr. 2006.

[84] M. C. C. Wobbe, A. Kerridge, and M. A. Zwijnenburg, “Optical excitation of MgO nanoparticles; a computational perspective,” *Phys. Chem. Chem. Phys.*, vol. 16, no. 40, pp. 22052–22061, Sep. 2014.

[85] M. Karahka and H. J. Kreuzer, “Field evaporation of insulators and semiconductors: Theoretical insights for ZnO,” *Ultramicroscopy*, vol. 159, Part 2, pp. 156–161, Dec. 2015.

[86] Y. Xia, M. Karahka, and H. J. Kreuzer, “Field evaporation of ZnO: A first-principles study,” *J. Appl. Phys.*, vol. 118, no. 2, p. 25901, Jul. 2015.

[87] N. Dawahre, G. Shen, S. Balci, W. Baughman, D. S. Wilbert, N. Harris, L. Butler, R. Martens, S. M. Kim, and P. Kung, “Atom Probe Tomography of Zinc Oxide Nanowires,” *J. Electron. Mater.*, vol. 41, no. 5, pp. 801–808, May 2012.

[88] B. G. Wicke, “Dynamics of the chemiluminescent oxidation of zinc atoms by nitrous oxide,” *J. Chem. Phys.*, vol. 78, no. 10, pp. 6036–6044, May 1983.

[89] M. Dolg, U. Wedig, H. Stoll, and H. Preuss, “Energy-adjusted abinitio pseudopotentials for the first row transition elements,” *J. Chem. Phys.*, vol. 86, no. 2, pp. 866–872, Jan. 1987.

[90] L. Zhang and H. Huang, “Young’s moduli of ZnO nanoplates: Ab initio determinations,” *Appl. Phys. Lett.*, vol. 89, no. 18, p. 183111, Oct. 2006.

[91] L. Zhang and H. Huang, “Structural transformation of ZnO nanostructures,” *Appl. Phys. Lett.*, vol. 90, no. 2, p. 23115, Jan. 2007.

[92] C. Li, W. Guo, Y. Kong, and H. Gao, "First-principles study on ZnO nanoclusters with hexagonal prism structures," *Appl. Phys. Lett.*, vol. 90, no. 22, p. 223102, May 2007.

[93] G. Malloci, L. Chiodo, A. Rubio, and A. Mattoni, "Structural and Optoelectronic Properties of Unsaturated ZnO and ZnS Nanoclusters," *J. Phys. Chem. C*, vol. 116, no. 15, pp. 8741–8746, Apr. 2012.

[94] R. D. Shannon, "Dielectric polarizabilities of ions in oxides and fluorides," *J. Appl. Phys.*, vol. 73, no. 1, pp. 348–366, Jan. 1993.

[95] E. P. Silaeva, L. Arnoldi, M. L. Karahka, B. Deconihout, A. Menand, H. J. Kreuzer, and A. Vella, "Do Dielectric Nanostructures Turn Metallic in High-Electric dc Fields?," *Nano Lett.*, vol. 14, no. 11, pp. 6066–6072, Nov. 2014.

[96] M. Büttiker and R. Landauer, "Traversal Time for Tunneling," *Phys. Rev. Lett.*, vol. 49, no. 23, pp. 1739–1742, Dec. 1982.

[97] N. Nakaoka and K. Watanabe, "*Ab initio* study of field evaporation from single-walled carbon nanotubes," *Phys. Rev. B*, vol. 65, no. 15, p. 155424, Apr. 2002.

[98] L. Mancini, N. Amirifar, D. Shinde, I. Blum, M. Gilbert, A. Vella, F. Vurpillot, W. Lefebvre, R. Lardé, E. Talbot, P. Pareige, X. Portier, A. Ziani, C. Davesnne, C. Durand, J. Eymery, R. Butté, J.-F. Carlin, N. Grandjean, and L. Rigutti, "Composition of Wide Bandgap Semiconductor Materials and Nanostructures Measured by Atom Probe Tomography and Its Dependence on the Surface Electric Field," *J. Phys. Chem. C*, vol. 118, no. 41, pp. 24136–24151, Oct. 2014.

[99] V. o. Turin and A. a. Balandin, "Performance degradation of GaN field-effect transistors due to thermal boundary resistance at GaN substrate interface," *Electron. Lett.*, vol. 40, no. 1, pp. 81–83, Jan. 2004.

[100] R. Banan Sadeghian and M. Saif Islam, "Ultralow-voltage field-ionization discharge on whiskered silicon nanowires for gas-sensing applications," *Nat. Mater.*, vol. 10, no. 2, pp. 135–140, Feb. 2011.

[101] H.-C. Han, C.-W. Chong, S.-B. Wang, D. Heh, C.-A. Tseng, Y.-F. Huang, S. Chattopadhyay, K.-H. Chen, C.-F. Lin, J.-H. Lee, and L.-C. Chen, "High K Nanophase Zinc Oxide on Biomimetic Silicon Nanotip Array as Supercapacitors," *Nano Lett.*, vol. 13, no. 4, pp. 1422–1428, Apr. 2013.

[102] C. Zener, "A Theory of the Electrical Breakdown of Solid Dielectrics," *Proc. R. Soc. Lond. Math. Phys. Eng. Sci.*, vol. 145, no. 855, pp. 523–529, Jul. 1934.

[103] A. Schiffrin, T. Paasch-Colberg, N. Karpowicz, V. Apalkov, D. Gerster, S. Mühlbrandt, M. Korbman, J. Reichert, M. Schultze, S. Holzner, J. V. Barth, R. Kienberger, R. Ernstorfer, V. S. Yakovlev, M. I. Stockman, and F. Krausz, "Optical-field-induced current in dielectrics," *Nature*, vol. 493, no. 7430, pp. 70–74, Jan. 2013.

[104] M. Schultze, E. M. Bothschafter, A. Sommer, S. Holzner, W. Schweinberger, M. Fiess, M. Hofstetter, R. Kienberger, V. Apalkov, V. S. Yakovlev, M. I. Stockman, and F. Krausz, "Controlling dielectrics with the electric field of light," *Nature*, vol. 493, no. 7430, pp. 75–78, Jan. 2013.

[105] L. V. Keldysh, "The effect of a strong electric field on the optical properties of insulating crystals," *Sov Phys JETP*, vol. 7, no. 5, pp. 788–790, 1958.

[106] W. Franz, "Einfluß eines elektrischen Feldes auf eine optische Absorptionskante," *Z. Für Naturforschung A*, vol. 13, no. 6, pp. 484–489, 2014.

[107] M. Durach, A. Rusina, M. F. Kling, and M. I. Stockman, “Metallization of Nanofilms in Strong Adiabatic Electric Fields,” *Phys. Rev. Lett.*, vol. 105, no. 8, p. 86803, Aug. 2010.

[108] V. Apalkov and M. I. Stockman, “Theory of dielectric nanofilms in strong ultrafast optical fields,” *Phys. Rev. B*, vol. 86, no. 16, p. 165118, Oct. 2012.

[109] T. T. Tsong, “Field penetration and band bending for semiconductor of simple geometries in high electric fields,” *Surf. Sci.*, vol. 85, no. 1, pp. 1–18, Jun. 1979.

[110] T. F. Kelly and D. J. Larson, “Atom Probe Tomography 2012,” *Annu. Rev. Mater. Res.*, vol. 42, no. 1, pp. 1–31, 2012.

[111] P. V. Liddicoat, X.-Z. Liao, Y. Zhao, Y. Zhu, M. Y. Murashkin, E. J. Lavernia, R. Z. Valiev, and S. P. Ringer, “Nanostructural hierarchy increases the strength of aluminium alloys,” *Nat. Commun.*, vol. 1, p. 63, Sep. 2010.

[112] K. Biswas, J. He, I. D. Blum, C.-I. Wu, T. P. Hogan, D. N. Seidman, V. P. Dravid, and M. G. Kanatzidis, “High-performance bulk thermoelectrics with all-scale hierarchical architectures,” *Nature*, vol. 489, no. 7416, pp. 414–418, Sep. 2012.

[113] L. M. Gordon and D. Joester, “Nanoscale chemical tomography of buried organic-inorganic interfaces in the chiton tooth,” *Nature*, vol. 469, no. 7329, pp. 194–197, Jan. 2011.

[114] L. Rigutti, I. Blum, D. Shinde, D. Hernández-Maldonado, W. Lefebvre, J. Houard, F. Vurpillot, A. Vella, M. Tchernycheva, C. Durand, J. Eymery, and B. Deconihout, “Correlation of Microphotoluminescence Spectroscopy, Scanning Transmission Electron Microscopy, and Atom Probe Tomography on a Single Nano-object Containing an InGaN/GaN Multiquantum Well System,” *Nano Lett.*, vol. 14, no. 1, pp. 107–114, Jan. 2014.

[115] K. Tedsree, T. Li, S. Jones, C. W. A. Chan, K. M. K. Yu, P. A. J. Bagot, E. A. Marquis, G. D. W. Smith, and S. C. E. Tsang, "Hydrogen production from formic acid decomposition at room temperature using a Ag-Pd core-shell nanocatalyst," *Nat. Nanotechnol.*, vol. 6, no. 5, pp. 302–307, May 2011.

[116] D. R. Sempolinski, W. D. Kingery, and H. L. Tuller, "Electronic Conductivity of Single Crystalline Magnesium Oxide," *J. Am. Ceram. Soc.*, vol. 63, no. 11–12, pp. 669–675, Nov. 1980.

[117] R. Ramírez, R. González, R. Pareja, and Y. Chen, "Semiconducting property of a wide-band-gap oxide crystal: Impact ionization and avalanche breakdown," *Phys. Rev. B*, vol. 55, no. 4, pp. 2413–2416, Jan. 1997.

[118] N. Klein and P. Solomon, "Current runaway in insulators affected by impact ionization and recombination," *J. Appl. Phys.*, vol. 47, no. 10, pp. 4364–4372, Oct. 1976.

[119] H. Kathrein and F. Freund, "Electrical conductivity of magnesium oxide single crystal below 1200 K," *J. Phys. Chem. Solids*, vol. 44, no. 3, pp. 177–186, Jan. 1983.

[120] M. Sterrer, O. Diwald, E. Knözinger, P. V. Sushko, and A. L. Shluger, "Energies and Dynamics of Photoinduced Electron and Hole Processes on MgO Powders," *J. Phys. Chem. B*, vol. 106, no. 48, pp. 12478–12482, Dec. 2002.

[121] B. Gault, F. Vurpillot, A. Vella, M. Gilbert, A. Menand, D. Blavette, and B. Deconihout, "Design of a femtosecond laser assisted tomographic atom probe," *Rev. Sci. Instrum.*, vol. 77, no. 4, p. 43705, Apr. 2006.

[122] Z. W. Gortel, H. J. Kreuzer, P. Piercy, and R. Teshima, “Theory of photodesorption of molecules by resonant laser-molecular vibrational coupling,” *Phys. Rev. B*, vol. 27, no. 8, pp. 5066–5083, Apr. 1983.

[123] K. M. Beck, M. Henyk, C. Wang, P. E. Trevisanutto, P. V. Sushko, W. P. Hess, and A. L. Shluger, “Site-specific laser modification of MgO nanoclusters: Towards atomic-scale surface structuring,” *Phys. Rev. B*, vol. 74, no. 4, p. 45404, Jul. 2006.

[124] G. L. Kellogg, “Temperature dependence of the silicon field evaporation voltage,” *Surf. Sci.*, vol. 124, no. 2, pp. L55–L59, Jan. 1983.

[125] F. Vurpillot, J. Houard, A. Vella, and B. Deconihout, “Thermal response of a field emitter subjected to ultra-fast laser illumination,” *J. Phys. Appl. Phys.*, vol. 42, no. 12, p. 125502, 2009.

[126] D. R. Kingham, “The post-ionization of field evaporated ions: A theoretical explanation of multiple charge states,” *Surf. Sci.*, vol. 116, no. 2, pp. 273–301, Apr. 1982.

[127] W. F. Giauque and R. C. Archibald, “The Entropy of Water from the Third Law of Thermodynamics. The Dissociation Pressure and Calorimetric Heat of the Reaction Mg(OH)2 = MgO + H2O.. The Heat Capacities of Mg(OH)2 and MgO from 20 to 300°K.,” *J. Am. Chem. Soc.*, vol. 59, no. 3, pp. 561–569, Mar. 1937.

[128] E. D. Palik, “Handbook of Optical Constants of Solids vol 1 (New York: Academic),” 1985.

[129] S. Stankic, M. Müller, O. Diwald, M. Sterrer, E. Knözinger, and J. Bernardi, “Size-Dependent Optical Properties of MgO Nanocubes,” *Angew. Chem. Int. Ed.*, vol. 44, no. 31, pp. 4917–4920, Aug. 2005.

[130] R. G. Forbes, “Field evaporation theory: a review of basic ideas,” *Appl. Surf. Sci.*, vol. 87–88, pp. 1–11, Mar. 1995.

[131] A. Vella, B. Deconihout, L. Marrucci, and E. Santamato, “Femtosecond Field Ion Emission by Surface Optical Rectification,” *Phys. Rev. Lett.*, vol. 99, no. 4, p. 46103, Jul. 2007.

[132] M. Karahka, Y. Xia, and H. J. Kreuzer, “The mystery of missing species in atom probe tomography of composite materials,” *Appl. Phys. Lett.*, vol. 107, no. 6, p. 62105, Aug. 2015.

[133] A. Devaraj, R. Colby, F. Vurpillot, and S. Thevuthasan, “Understanding Atom Probe Tomography of Oxide-Supported Metal Nanoparticles by Correlation with Atomic-Resolution Electron Microscopy and Field Evaporation Simulation,” *J. Phys. Chem. Lett.*, vol. 5, no. 8, pp. 1361–1367, Apr. 2014.

[134] A. Devaraj, “Halide ions,” 2015.

[135] F. Hanke and H. J. Kreuzer, “Breaking bonds in the atomic force microscope: Extracting information,” *Biointerphases*, vol. 1, no. 1, pp. 11–17.

[136] L. Rigutti, “APT,” 2015.

[137] H. J. Kreuzer, S. H. Payne, A. Drozdowski, and D. Menzel, “Theory of dissociative and nondissociative adsorption and desorption,” *J. Chem. Phys.*, vol. 110, no. 14, pp. 6982–6999, Apr. 1999.

[138] H. Watanabe, M. Wada, and T. Takahashi, “The Activation Energy for Oxygen Desorption from Zinc Oxide Surfaces,” *Jpn. J. Appl. Phys.*, vol. 4, no. 12, pp. 945–947, Dec. 1965.

[139] J. H. Block, H. J. Kreuzer, and L. C. Wang, “Electrostatic field effects in surface reactivity: Adsorption, dissociation and catalytic reaction of nitric oxide,” *Surf. Sci.*, vol. 246, no. 1, pp. 125–134, Apr. 1991.

[140] M. Karahka and H. J. Kreuzer, “Water whiskers in high electric fields,” *Phys. Chem. Chem. Phys.*, vol. 13, no. 23, pp. 11027–11033, May 2011.

[141] M. L. Karahka and H. J. Kreuzer, “Charge transport along proton wires,” *Biointerphases*, vol. 8, no. 1, p. 13, Jun. 2013.

[142] S. Jaenicke, A. Ciszewski, W. Drachsel, U. Weigmann, T. T. Tsong, J. R. Pitts, J. H. Block, and D. Menzel, “FIELD-ASSISTED PHOTODESORPTION OF IONS FROM METAL AND SEMICONDUCTOR SURFACES,” *J. Phys. Colloq.*, vol. 47, no. C7, pp. C7-343-C7-348, Nov. 1986.

[143] S. Jaenicke, A. Ciszewski, J. DöSselmann, W. Drachsel, J. H. Block, and D. Menzel, “FIELD-INDUCED STRUCTURAL CHANGES IN ADSORBED LAYERS OF POLAR MOLECULES STUDIED BY PHOTON-STIMULATED DESORPTION,” *J. Phys. Colloq.*, vol. 49, no. C6, pp. C6-191-C6-196, Nov. 1988.

[144] J. Dirks, W. Drachsel, and J. H. Block, “PHOTON INDUCED FIELD DESORPTION OF WATER CLUSTERS,” *J. Phys. Colloq.*, vol. 50, no. C8, pp. C8-153-C8-158, Nov. 1989.

[145] J. Dirks, W. Drachsel, and J. H. Block, “The interaction of synchrotron light with water adsorbed on a Ag-field emitter in the presence of a high electric field,” 1992, vol. 10, pp. 231–234.

[146] A. Ciszewski and R. Błaszczyszyn, “Interaction of water with field emitter tips,” *Prog. Surf. Sci.*, vol. 48, no. 1–4, pp. 99–108, Jan. 1995.

[147] H. D. Beckey, “Mass Spectrographic Investigations, Using a Field Emission Ion Source,” *Z. Naturforschung Teil A*, vol. 14, pp. 712–721, 1959.

[148] H. D. Beckey, “Mass Spectrometric Investigation by Means of a Field-Emission Source of Ion-Molecule Reactions and of the Association of Water,” *Z. Naturforschung Teil A*, vol. 15a, p. 822, 1960.

[149] W. A. Schmidt, “Massenspektrometrische Untersuchung der Feldionisation von Wasserdampf an Spitzen aus Wolfram, Platin und Iridium,” *Z. Naturforschung Teil A*, vol. 19, p. 318, Mar. 1964.

[150] T. T. Tsong and Y. Liou, “Cluster-ion formation in pulsed-laser-stimulated field desorption of condensed materials,” *Phys. Rev. B*, vol. 32, no. 7, pp. 4340–4357, Oct. 1985.

[151] A. R. Anway, “Field Ionization of Water,” *J. Chem. Phys.*, vol. 50, no. 5, pp. 2012–2021, Mar. 1969.

[152] Y. C. Choi, C. Pak, and K. S. Kim, “Electric field effects on water clusters (n = 3–5): Systematic ab initio study of structures, energetics, and transition states,” *J. Chem. Phys.*, vol. 124, no. 9, pp. 94308-94308–4, Mar. 2006.

[153] T. James, D. J. Wales, and J. Hernández Rojas, “Energy landscapes for water clusters in a uniform electric field,” *J. Chem. Phys.*, vol. 126, no. 5, pp. 54506-54506–13, Feb. 2007.

[154] D. Rai, A. D. Kulkarni, S. P. Gejji, and R. K. Pathak, “Water clusters (H2O)n, n = 6–8, in external electric fields,” *J. Chem. Phys.*, vol. 128, no. 3, pp. 34310-34310–14, Jan. 2008.

[155] D. L. Cocke, G. Abend, and J. H. Block, “A Mass spectrometric technique for observation of chemical kinetics in physisorbed layers,” *Int. J. Chem. Kinet.*, vol. 9, no. 1, pp. 157–159, 1977.

[156] C. E. Dykstra, “External electric field effects on the water trimer,” *Chem. Phys. Lett.*, vol. 299, no. 2, pp. 132–136, Jan. 1999.

[157] R. L. C. Wang, H. Jürgen Kreuzer, M. Grunze, and A. J. Pertsin, “The effect of electrostatic fields on an oligo(ethylene glycol) molecule: dipole moments, polarizabilities and field dissociation,” *Phys. Chem. Chem. Phys.*, vol. 2, no. 8, pp. 1721–1727, 2000.

[158] A. J. Pertsin, M. Grunze, H. J. Kreuzer, and R. L. C. Wang, “The effect of electrostatic fields on an oligo(ethylene glycol) terminated alkanethiol self-assembled monolayer,” *Phys. Chem. Chem. Phys.*, vol. 2, no. 8, pp. 1729–1733, Jan. 2000.

[159] A. S. Dhoot, J. D. Yuen, M. Heeney, I. McCulloch, D. Moses, and A. J. Heeger, “Beyond the metal-insulator transition in polymer electrolyte gated polymer field-effect transistors,” *Proc. Natl. Acad. Sci.*, vol. 103, no. 32, pp. 11834–11837, Aug. 2006.

[160] R. L. C. Wang, H. J. Kreuzer, and M. Grunze, “The interaction of oligo(ethylene oxide) with water: a quantum mechanical study,” *Phys. Chem. Chem. Phys.*, vol. 2, no. 16, pp. 3613–3622, Jan. 2000.

[161] D. Kang, J. Dai, Y. Hou, and J. Yuan, “Structure and vibrational spectra of small water clusters from first principles simulations,” *J. Chem. Phys.*, vol. 133, no. 1, p. 14302, Jul. 2010.

[162] S. Cukierman, “The transfer of protons in water wires inside proteins,” *Front. Biosci. J. Virtual Libr.*, vol. 8, pp. s1118-1139, Sep. 2003.

[163] N. Pavlenko, “Proton wires in an electric field: the impact of the Grotthuss mechanism on charge translocation,” *J. Phys. Condens. Matter*, vol. 15, no. 2, p. 291, Jan. 2003.

[164] J. F. Nagle and H. J. Morowitz, “Molecular mechanisms for proton transport in membranes,” *Proc. Natl. Acad. Sci.*, vol. 75, no. 1, pp. 298–302, Jan. 1978.

[165] M. Akeson and D. W. Deamer, “Proton conductance by the gramicidin water wire. Model for proton conductance in the F1F0 ATPases?,” *Biophys. J.*, vol. 60, no. 1, pp. 101–109, Jul. 1991.

[166] D. E. Sagnella, K. Laasonen, and M. L. Klein, “Ab initio molecular dynamics study of proton transfer in a polyglycine analog of the ion channel gramicidin A,” *Biophys. J.*, vol. 71, no. 3, pp. 1172–1178, Sep. 1996.

[167] M. Wikström, “Proton translocation by bacteriorhodopsin and heme-copper oxidases,” *Curr. Opin. Struct. Biol.*, vol. 8, no. 4, pp. 480–488, Aug. 1998.

[168] A.-N. Bondar, J. Baudry, S. Suhai, S. Fischer, and J. C. Smith, “Key Role of Active-Site Water Molecules in Bacteriorhodopsin Proton-Transfer Reactions,” *J. Phys. Chem. B*, vol. 112, no. 47, pp. 14729–14741, Nov. 2008.

[169] I. Hofacker and K. Schulten, “Oxygen and proton pathways in cytochrome c oxidase,” *Proteins Struct. Funct. Bioinforma.*, vol. 30, no. 1, pp. 100–107, 1998.

[170] A. Namslauer, H. Lepp, M. Brändén, A. Jasaitis, M. I. Verkhovsky, and P. Brzezinski, “Plasticity of Proton Pathway Structure and Water Coordination in

Cytochrome c Oxidase," *J. Biol. Chem.*, vol. 282, no. 20, pp. 15148–15158, May 2007.

[171] M. A. Kozlova, H. D. Juhnke, D. A. Cherepanov, C. R. D. Lancaster, and A. Y. Mulkidjanian, "Proton transfer in the photosynthetic reaction center of Blastochloris viridis," *FEBS Lett.*, vol. 582, no. 2, pp. 238–242, Jan. 2008.

[172] R. A. W. Frank, C. M. Titman, J. V. Pratap, B. F. Luisi, and R. N. Perham, "A Molecular Switch and Proton Wire Synchronize the Active Sites in Thiamine Enzymes," *Science*, vol. 306, no. 5697, pp. 872–876, Oct. 2004.

[173] K. J. Schweighofer and A. Pohorille, "Computer Simulation of Ion Channel Gating: The M2 Channel of Influenza A Virus in a Lipid Bilayer," *Biophys. J.*, vol. 78, no. 1, pp. 150–163, Jan. 2000.

[174] C. J. T. de Grothuss, "Theory of decomposition of liquids by electrical currents 'Sur la décomposition de l'eau et des corps qu'elle tient en dissolution à l'aide de l'électricité galvanique,'" *Galvanique Ann Chim*, vol. 58, pp. 54–73, 1806.

[175] R. Pomès and B. Roux, "Quantum effects on the structure and energy of a protonated linear chain of hydrogen-bonded water molecules," *Chem. Phys. Lett.*, vol. 234, no. 4–6, pp. 416–424, Mar. 1995.

[176] R. Pomès and B. Roux, "Theoretical Study of H+ Translocation along a Model Proton Wire," *J. Phys. Chem.*, vol. 100, no. 7, pp. 2519–2527, Jan. 1996.

[177] R. Pomès and B. Roux, "Structure and dynamics of a proton wire: a theoretical study of H+ translocation along the single-file water chain in the gramicidin A channel," *Biophys. J.*, vol. 71, no. 1, pp. 19–39, Jul. 1996.

[178] H. S. Mei, M. E. Tuckerman, D. E. Sagnella, and M. L. Klein, "Quantum Nuclear ab Initio Molecular Dynamics Study of Water Wires," *J. Phys. Chem. B*, vol. 102, no. 50, pp. 10446–10458, Dec. 1998.

[179] R. R. Sadeghi and H.-P. Cheng, "The dynamics of proton transfer in a water chain," *J. Chem. Phys.*, vol. 111, no. 5, pp. 2086–2094, Aug. 1999.

[180] K. Drukker, S. W. de Leeuw, and S. Hammes-Schiffer, "Proton transport along water chains in an electric field," *J. Chem. Phys.*, vol. 108, no. 16, pp. 6799–6808, Apr. 1998.

[181] H. Decornez, K. Drukker, and S. Hammes-Schiffer, "Solvation and Hydrogen-Bonding Effects on Proton Wires," *J. Phys. Chem. A*, vol. 103, no. 15, pp. 2891–2898, Apr. 1999.

[182] S. Hammes-Schiffer, "Effects of model protein environments on the dynamics of proton wires," *Isr. J. Chem.*, vol. 39, pp. 397–407, 1999.

[183] M. L. Brewer, U. W. Schmitt, and G. A. Voth, "The Formation and Dynamics of Proton Wires in Channel Environments," *Biophys. J.*, vol. 80, no. 4, pp. 1691–1702, Apr. 2001.

[184] A. V. Nemukhin, B. L. Grigorenko, I. A. Topol, and S. K. Burt, "Quantum Chemical Simulations of the Proton Transfer in Water Wires Attached to Molecular Walls," *J. Phys. Chem. B*, vol. 107, no. 13, pp. 2958–2965, Apr. 2003.

[185] B. L. de Groot and H. Grubmüller, "Water Permeation Across Biological Membranes: Mechanism and Dynamics of Aquaporin-1 and GlpF," *Science*, vol. 294, no. 5550, pp. 2353–2357, Dec. 2001.

[186] S. Braun-Sand, A. Burykin, Z. T. Chu, and A. Warshel, "Realistic Simulations of Proton Transport along the Gramicidin Channel: Demonstrating the Importance of Solvation Effects," *J. Phys. Chem. B*, vol. 109, no. 1, pp. 583–592, Jan. 2005.

[187] O. Vendrell and H.-D. Meyer, "Proton conduction along a chain of water molecules. Development of a linear model and quantum dynamical investigations using the multiconfiguration time-dependent Hartree method," *J. Chem. Phys.*, vol. 122, no. 10, pp. 104505-104505–11, Mar. 2005.

[188] Q. Cui and M. Karplus, "Is a 'Proton Wire' Concerted or Stepwise? A Model Study of Proton Transfer in Carbonic Anhydrase," *J. Phys. Chem. B*, vol. 107, no. 4, pp. 1071–1078, Jan. 2003.

[189] A. Isaev, T. Kar, and S. Scheiner, "Periodicity in proton conduction along a H-bonded chain. Application to biomolecules," *Int. J. Quantum Chem.*, vol. 108, no. 3, pp. 607–616, 2008.

[190] A. N. Isaev, "Quantum-Chemical Calculations of a Long Proton Wire. Application of a Harmonic Model to Analysis of the Structure of an Ionic Defect in a Water Chain with an Excess Proton," *J. Phys. Chem. A*, vol. 114, no. 5, pp. 2201–2212, Feb. 2010.

[191] U. Viswanathan, D. Basak, D. Venkataraman, J. T. Fermann, and S. M. Auerbach, "Modeling Energy Landscapes of Proton Motion in Nonaqueous, Tethered Proton Wires," *J. Phys. Chem. A*, vol. 115, no. 21, pp. 5423–5434, Jun. 2011.

[192] G. Zundel and H. Metzger, "Energiebänder der tunnelnden Überschuß-Protonen in flüssigen Säuren. Eine IR-spektroskopische Untersuchung der Natur der Gruppierungen $H_5O_2^+$," *Z. Für Phys. Chem.*, vol. 58, no. 5_6, pp. 225–245, Apr. 1968.

[193] N. Bjerrum, “Structure and properties of ice,” *Dan. Vidensk Selks Skr*, vol. 27, p. 1, 1951.

[194] C. Fang, W.-F. Li, R. S. Koster, J. Klimeš, A. van Blaaderen, and M. A. van Huis, “The accurate calculation of the band gap of liquid water by means of GW corrections applied to plane-wave density functional theory molecular dynamics simulations,” *Phys. Chem. Chem. Phys.*, vol. 17, no. 1, pp. 365–375, Dec. 2014.

[195] D. N. Silverman, C. Tu, X. Chen, S. M. Tanhauser, A. J. Kresge, and P. J. Laipis, “Rate-equilibria relationships in intramolecular proton transfer in human carbonic anhydrase III,” *Biochemistry (Mosc.)*, vol. 32, no. 40, pp. 10757–10762, Oct. 1993.

[196] X. Ren, C. Tu, P. J. Laipis, and D. N. Silverman, “Proton Transfer by Histidine 67 in Site-Directed Mutants of Human Carbonic Anhydrase III,” *Biochemistry (Mosc.)*, vol. 34, no. 26, pp. 8492–8498, Jul. 1995.

[197] D. N. Silverman, “Marcus rate theory applied to enzymatic proton transfer,” *Biochim. Biophys. Acta BBA - Bioenerg.*, vol. 1458, no. 1, pp. 88–103, May 2000.

[198] S. Cukierman, E. P. Quigley, and D. S. Crumrine, “Proton conduction in gramicidin A and in its dioxolane-linked dimer in different lipid bilayers,” *Biophys. J.*, vol. 73, no. 5, pp. 2489–2502, Nov. 1997.

Appendix A Copyright Permission Letters

This Agreement between Markus L Karahka ("You") and AIP Publishing LLC ("AIP Publishing LLC") consists of your license details and the terms and conditions provided by AIP Publishing LLC and Copyright Clearance Center.

License Number	3878910108601
License date	May 30, 2016
Licensed Content Publisher	AIP Publishing LLC
Licensed Content Publication	Applied Physics Letters
Licensed Content Title	The mystery of missing species in atom probe tomography of composite materials
Licensed Content Author	M. Karahka,Y. Xia,H. J. Kreuzer
Licensed Content Date	Aug 14, 2015
Licensed Content Volume Number	107
Licensed Content Issue Number	6
Type of Use	Thesis/Dissertation
Requestor type	Author (original article)
Format	Print and electronic
Portion	Excerpt (> 800 words)
Will you be translating?	No
Title of your thesis / dissertation	Physics in High Electric Fields
Expected completion date	Sep 2016
Estimated size (number of pages)	180
Requestor Location	Markus L Karahka 79 Bayers Mill Rd. Musquodoboit Harbour, NS B0J 2L0 Canada Attn: Markus L Karahka
Billing Type	Invoice
Billing Address	Markus L Karahka 79 Bayers Mill Rd. Musquodoboit Harbour, NS B0J 2L0

	Canada Attn: Markus L Karahka
Total	0.00 CAD

Terms and Conditions

This Agreement between Markus L Karahka ("You") and AIP Publishing LLC ("AIP Publishing LLC") consists of your license details and the terms and conditions provided by AIP Publishing LLC and Copyright Clearance Center.

License Number	3878901076584
License date	May 30, 2016
Licensed Content Publisher	AIP Publishing LLC
Licensed Content Publication	Journal of Applied Physics
Licensed Content Title	Field evaporation of ZnO: A first-principles study
Licensed Content Author	Yu Xia,Markus Karahka,H. J. Kreuzer
Licensed Content Date	Jul 8, 2015
Licensed Content Volume Number	118
Licensed Content Issue Number	2
Type of Use	Thesis/Dissertation
Requestor type	Author (original article)
Format	Print and electronic
Portion	Excerpt (> 800 words)
Will you be translating?	No
Title of your thesis / dissertation	Physics in High Electric Fields
Expected completion date	Sep 2016
Estimated size (number of pages)	180
Requestor Location	Markus L Karahka 79 Bayers Mill Rd. Musquodoboit Harbour, NS B0J 2L0 Canada Attn: Markus L Karahka
Billing Type	Invoice
Billing Address	Markus L Karahka 79 Bayers Mill Rd. Musquodoboit Harbour, NS B0J 2L0

	Canada Attn: Markus L Karahka
Total	0.00 CAD
Terms and Conditions	

This Agreement between Markus L Karahka ("You") and Elsevier ("Elsevier") consists of your license details and the terms and conditions provided by Elsevier and Copyright Clearance Center.

License Number	3878891374348
License date	May 30, 2016
Licensed Content Publisher	Elsevier
Licensed Content Publication	Ultramicroscopy
Licensed Content Title	Field evaporation of insulators and semiconductors: Theoretical insights for ZnO
Licensed Content Author	Markus Karahka,H.J. Kreuzer
Licensed Content Date	December 2015
Licensed Content Volume Number	159
Licensed Content Issue Number	n/a
Start Page	156
End Page	161
Type of Use	reuse in a thesis/dissertation
Intended publisher of new work	other
Portion	full article
Format	both print and electronic
Are you the author of this Elsevier article?	Yes
Will you be translating?	No
Order reference number	
Title of your thesis/dissertation	Physics in High Electric Fields
Expected completion date	Sep 2016
Estimated size (number of pages)	180

Elsevier VAT number	GB 494 6272 12
Requestor Location	Markus L Karahka 79 Bayers Mill Rd. Musquodoboit Harbour, NS B0J 2L0 Canada

This Agreement between Markus L Karahka ("You") and Elsevier ("Elsevier") consists of your license details and the terms and conditions provided by Elsevier and Copyright Clearance Center.

License Number	3878891469760
License date	May 30, 2016
Licensed Content Publisher	Elsevier
Licensed Content Publication	Current Opinion in Solid State & Materials Science
Licensed Content Title	Atom Probe Tomography and field evaporation of insulators and semiconductors: Theoretical issues
Licensed Content Author	Elena P. Silaeva,Markus Karahka,H.J. Kreuzer
Licensed Content Date	October 2013
Licensed Content Volume Number	17
Licensed Content Issue Number	5
Start Page	211
End Page	216
Type of Use	reuse in a thesis/dissertation
Intended publisher of new work	other
Portion	full article
Format	both print and electronic
Are you the author of this Elsevier article?	Yes
Will you be translating?	No
Order reference number	
Title of your thesis/dissertation	Physics in High Electric Fields
Expected completion date	Sep 2016
Estimated size (number of pages)	180
Elsevier VAT number	GB 494 6272 12

Requestor Location	Markus L Karahka 79 Bayers Mill Rd. Musquodoboit Harbour, NS B0J 2L0 Canada Attn: Markus L Karahka

This Agreement between Markus L Karahka ("You") and Elsevier ("Elsevier") consists of your license details and the terms and conditions provided by Elsevier and Copyright Clearance Center.

License Number	3878891264982
License date	May 30, 2016
Licensed Content Publisher	Elsevier
Licensed Content Publication	Ultramicroscopy
Licensed Content Title	Field evaporation of oxides: A theoretical study
Licensed Content Author	Markus Karahka,H.J. Kreuzer
Licensed Content Date	September 2013
Licensed Content Volume Number	132
Licensed Content Issue Number	n/a
Start Page	54
End Page	59
Type of Use	reuse in a thesis/dissertation
Intended publisher of new work	other
Portion	full article
Format	both print and electronic
Are you the author of this Elsevier article?	Yes
Will you be translating?	No
Order reference number	
Title of your thesis/dissertation	Physics in High Electric Fields
Expected completion date	Sep 2016
Estimated size (number of pages)	180
Elsevier VAT number	GB 494 6272 12
Requestor Location	Markus L Karahka 79 Bayers Mill Rd.

Musquodoboit Harbour, NS B0J 2L0
Canada
Attn: Markus L Karahka

This Agreement between Markus L Karahka ("You") and Elsevier ("Elsevier") consists of your license details and the terms and conditions provided by Elsevier and Copyright Clearance Center.

License Number	3878890400443
License date	May 30, 2016
Licensed Content Publisher	Elsevier
Licensed Content Publication	Surface Science
Licensed Content Title	New physics and chemistry in high electrostatic fields
Licensed Content Author	M.L. Karahka,H.J. Kreuzer
Licensed Content Date	January 2016
Licensed Content Volume Number	643
Licensed Content Issue Number	n/a
Start Page	164
End Page	171
Type of Use	reuse in a thesis/dissertation
Portion	full article
Format	both print and electronic
Are you the author of this Elsevier article?	Yes
Will you be translating?	No
Order reference number	
Title of your thesis/dissertation	Physics in High Electric Fields
Expected completion date	Sep 2016
Estimated size (number of pages)	180
Elsevier VAT number	GB 494 6272 12

Requestor Location

Markus L Karahka
79 Bayers Mill Rd.

Musquodoboit Harbour, NS B0J 2L0
Canada
Attn: Markus L Karahka

Title: Do Dielectric Nanostructures Turn Metallic in High-Electric dc Fields?

Author: E. P. Silaeva, L. Arnoldi, M. L. Karahka, et al

Publication: Nano Letters

Publisher: American Chemical Society

Date: Nov 1, 2014

PERMISSION/LICENSE IS GRANTED FOR YOUR ORDER AT NO CHARGE

This type of permission/license, instead of the standard Terms & Conditions, is sent to you because no fee is being charged for your order. Please note the following:

Permission is granted for your request in both print and electronic formats, and translations.

- If figures and/or tables were requested, they may be adapted or used in part.
- Please print this page for your records and send a copy of it to your publisher/graduate school.
- Appropriate credit for the requested material should be given as follows: "Reprinted (adapted) with permission from (COMPLETE REFERENCE CITATION). Copyright (YEAR) American Chemical Society." Insert appropriate information in place of the capitalized words.
- One-time permission is granted only for the use specified in your request. No additional uses are granted (such as derivative works or other editions). For any other uses, please submit a new request.